Design and Testing of a Bidirectional Smart Charger Prototype

by

Jordan Morris

A thesis

presented to the University of Waterloo

in fulfillment of the

thesis requirement for the degree of

Master of Applied Science

in

Electrical and Computer Engineering

Waterloo, Ontario, Canada, 2015

Author's Declaration

I hereby declare that I am the sole author of this thesis. This is a true copy of the thesis, including any required final revisions, as accepted by my examiners.

I understand that my thesis may be made electronically available to the public.

Abstract

Rising greenhouse gas emissions, increased fuel costs, and recent technological advances are causing a paradigm shift in the auto-industry away from traditional internal combustion engine vehicles to Electric Vehicles (EVs). Although good for the environment, mass deployment of electric and hybrid electric vehicles has the possibility to cause negative effects to the power grid, such as phase imbalances, voltage deviations, and distribution transformer overloading, since some EVs can potentially draw as high as 19.2 kW in a household from a single-phase outlet. However, if charging is properly controlled and coordinated, EVs have the potential to support the power grid, possibly acting as distributed generation or a storage unit.

This thesis aims to address the aforementioned issues by developing a fully-functional "smart" bidirectional EV charger prototype. The term smart refers to the charger's ability to control the charging and discharging of the battery pack based on the preferences of the car owner, the electricity price at the time of use, battery's operational constraints, and the distribution system's requirements at the command of the utility or Local Distribution Company (LDC). Bidirectional refers to power flow, i.e., the charger will employ a design that allows the power to flow from the grid to the battery and vise-versa.

The thesis first reviews existing bidirectional charger topologies and smart grid communication technologies. Then, relevant standards, battery technologies, and controller options are discussed; this finally is followed by the charger design process and simulation results to validate the design. Finally, the smart bidirectional charger prototype is presented and tested, to validate and demonstrate its effectiveness in addressing power grid issues.

Acknowledgements

I owe the completion of this thesis to so many individuals who were able to help me overcome everything from technical obstacles to being there for me when I needed a break. Firstly, I need to thank my supervisors, Mehrdad Kazerani and Claudio Cañizares. Without their help this thesis would never have been possible. They provided inspiration and direction when needed and were able to guide me during times when the road ahead was uncertain.

I owe my family a debt of gratitude for their support through this entire process and for always loving me, even though at times I haven't been the best son or brother, missing important family gatherings to spend time working on this thesis. Alex Green, my roommate, also deserves a mention as someone who was there for me to bounce idea off of while unwinding after a long day.

I owe thanks to my lab mates, Marten Pape and Mauricio Restrepo. It was nice to have Marten in the lab as both a friend a teammate. It relieved a lot of stress to have someone there to discuss potential solutions to problems and also, when a break was in order, someone to talk about nonsense with. Mauricio has been very helpful in the final leg of this project. Having left early to start my employment at Tesla Motors in California, Mauricio, without hesitation, volunteered to do anything I needed while away to complete this thesis. His assistance in this matter was much needed and appreciated.

Finally, to all others in my research group, for creating an inspiring and comforting work place that I looked forward to coming to every day. Thank you.

Dedication

To my family…

Table of Contents

Author's Declaration ii
Abstract iii
Acknowledgements iv
Dedication v
Table of Contents vi
List of Figures x
List of Tables xiii
Acronyms xv
Chapter 1 Introduction 1
1.1 Motivation 1
1.2 Literature Review of Smart EV Chargers 2
1.2.1 Bidirectional EV/PHEV Battery Charger Topologies 3
1.2.2 Smart Grid Communication Technologies 4
1.3 Research Objectives 7
1.4 Thesis Outline 8
Chapter 2 Background Review 10
2.1 Relevant Standards 10

2.1.1 SAE J1772 11
2.1.2 IEEE 1547 12
2.2 Lithium Ion Battery Technology and Charging Controllers 13
2.2.1 Battery Model 13
2.2.2 Constant Current, Constant Voltage Charging 15
2.2.3 Battery Limitations and Degradation 17
2.2.4 Cell Balancing and Battery Management Systems 18
2.3 AC/DC Controllers 18
2.3.1 Control Variables and Operating Modes 19
2.3.2 Stationary Frame PR Controller 20
2.3.3 Synchronous Frame Dq Controller 22
2.4 Summary 25
Chapter 3 Smart Charger Design 26
3.1 Charger Topology and Battery Model 26
3.1.1 Charger Topology 27
3.1.2 Battery Model 28
3.2 Reactive Power Controllers 29
3.2.1 PR Control 29
3.2.2 Dq Control 31
3.2.3 Controller Comparison 34
3.3 Active Power Controllers 35
3.3.1 Constant Power Charging 35
3.4 Optimal Sizing of Components 37
3.4.1 DC/DC Converter Parameters 37
3.4.2 DC Link Ripple 38

3.4.3 Minimum DC Link Voltage 41
3.4.4 DC Link Capacitor Size 42
3.4.5 DC Link Capacitor Current Ripple 44
3.4.6 Final Component Values 45
3.5 Summary 46
Chapter 4 Level 1 Bidirectional Charger Simulation Results 47
4.1 Simulation Setup 47
4.2 Steady-State Response 50
4.3 Step Response 58
4.4 Summary 61
Chapter 5 Smart Charger Prototype Implementation 62
5.1 Prototype Main Components 62
5.1.1 Smart Charger Control Board 63
5.1.2 Smart Grid Communication Controller 64
5.1.3 Battery Pack and BMS 65
5.1.4 Central Control Unit 66
5.2 Experimental Setup 67
5.3 Prototype Response Characteristics 71
5.3.1 Steady-State Response 71
5.3.2 Step Response 76
5.3.3 Efficiency Analysis 77
5.4 Comparison 78
5.5 Prototype Bill of Materials 79
5.6 Summary 80
Chapter 6 Conclusions 82

6.1 Summary 82
6.2 Contributions 83
6.3 Future Work 84
Appendix A Smart Charger Control Board Design 85
A.1 Gate Driver Optical Fiber Transmitter 85
A.2 Optical Fiber Receiver/Gate Driver Module 86
A.3 Voltage/Current Sensors Conditioning Module 87
A.4 Power Supply Module 88
A.5 Smart Charger Printed Circuit Board Layout 89
Appendix B Smart Charger Communication Controller Interface 92
References 96

List of Figures

Figure 2-1. Lithium ion cell electrical model. 14

Figure 2-2 Cell charging curve 15

Figure 2-3. Cell discharging curve 15

Figure 2-4. Charging profile of 40 Ah 32 cell, 105.6 V li-ion battery pack. 16

Figure 2-5. CV, CC charging control block diagram. 17

Figure 2-6. Battery life degradation, 40 Ah pack 100% SOC to 100% DOD. 17

Figure 2-7. Breakdown of VSC current control techniques. 19

Figure 2-8. Charger-grid connection. 19

Figure 2-9. Two-loop UPF controller block diagram. 20

Figure 2-10. PR controller block diagram. 21

Figure 2-11. PLL for dq transform. 24

Figure 2-12. Block diagram dq controller. 25

Figure 3-1. Four quadrants of the P-Q plane. 27

Figure 3-2. Single phase bidirectional battery charger topology. 28

Figure 3-3. Simple lithium-ion battery pack electrical model. 28

Figure 3-4. Block diagram of PR Controller with power factor control. 30

Figure 3-5. AC/DC PR Controller with reactive power support. 31

Figure 3-6. AC/DC DQ Controller with reactive power support. 32

Figure 3-7. First order discrete state space filter. 33
Figure 3-8. Simulation results of first order state space filter in reactive power controller. 34
Figure 3-9. CC-CV charging profile normalized. 36
Figure 3-10. Block diagram for constant power charging algorithm. 36
Figure 3-11. Bidirectional buck-boost DC/DC converter. 37
Figure 3-12. Minimum allowable DC link voltage vs. coupling inductor size. 42
Figure 3-13. DC link capacitor size vs. DC link voltage. 43
Figure 3-14. DC link capacitance vs. DC link capacitor current ripple. 45
Figure 4-1. Smart charger simulation model. 48
Figure 4-2. AC/DC controller. 48
Figure 4-3. DC/DC controller. 49
Figure 4-4. Smart charger simulation modes corresponding to Table 4-2. 50
Figure 4-5. Steady-state response for Simulation 1, $Ps = 1.92$ kW and $Qs = 0$ kVAR. 51
Figure 4-6. Steady-state response for Simulation 2, $Ps = 1.36$ kW and $Qs = 1.36$ kVAR. 52
Figure 4-7. Steady-state response for simulation 3, $Ps = 0$ kW and $Qs = 1.92$ kVAR. 53
Figure 4-8. Steady-state response for Simulation 4, $Ps = -1.36$ kW and $Qs = 1.36$ kVAR. 54
Figure 4-9. Steady-state response for Simulation 5, $Ps = -1.92$ kW and $Qs = 0$ kVAR. 55
Figure 4-10. Steady-state response for Simulation 6,$Ps = -1.36$ kW and $Qs = -1.36$ kVAR. 56
Figure 4-11. Steady-state response for Simulation 7, $Ps = 0$ kW and $Qs = -1.92$ kVAR. 57
Figure 4-12. Steady-state response for Simulation 8, $Ps = 1.36$ kW and $Qs = -1.36$ kVAR. 58
Figure 4-13. Step-response Plot 1. 60
Figure 4-14. Step-response Plot 2. 61
Figure 5-1. Smart charger Control Board. 64
Figure 5-2. Smart Charger communication protocols. 67
Figure 5-3. Smart Charger - battery pack layout 68

Figure 5-4. Smart Charger HV connectors. 69
Figure 5-5. Smart Charger side view. 70
Figure 5-6. Smart Charger top view 71
Figure 5-7. Steady-state response for Experiment 1, $Ps = 1.7$ kW and $Qs = 0$ kVAR. 72
Figure 5-8. Steady-state response for Experiment 2, $Ps = 1.2$ kW and $Qs = 1.2$ kVAR. 73
Figure 5-9. Steady-state response for Experiment 3, $Ps = 0$ kW and $Qs = 1.7$ kVAR. 73
Figure 5-10. Steady-state response for Experiment 4, $Ps = -1.2$ kW and $Qs = 1.2$ kVAR. 74
Figure 5-11. Steady-state response for Experiment 5, $Ps = -1.7$ kW and $Qs = 0$ kVAR. 74
Figure 5-12. Steady-state response for Experiment 6, $Ps = -1.2$ kW and $Qs = -1.2$ kVAR. 75
Figure 5-13. Steady-state response for Experiment 7, $Ps = 0$ kW and $Qs = -1.7$ kVAR. 75
Figure 5-14. Steady-state response for Experiment 8, $Ps = 1.2$ kW and $Qs = -1.2$ kVAR. 76
Figure 5-15. Prototype step response oscilloscope screenshot. 77
Figure A-1. IGBT gate driver optical fiber transmitter. 86
Figure A-2. Optical fiber receiver/gate driver module 87
Figure A-3. Voltage/current sensor conditioning module 88
Figure A-4. Power supply module. 89
Figure A-5. Smart Charger Control Board PCB layout. 90
Figure A-6. Smart Charger Board, populated. 91
Figure B-1. Smart charger broadcast network. 93
Figure B-2. Smart Charger controller, main page, 1. 94
Figure B-3. Smart Charger controller, main page 2. 95

List of Tables

Table 1-1. Smart charger communication technologies. 7

Table 2-1. SAE J1772 charging levels. 11

Table 2-2. Distributed resource interconnection system response to abnormal voltages 12

Table 2-3. Distributed resource interconnection system response to abnormal frequency 12

Table 2-4. Distributed Resource Maximum Current Distortion. 13

Table 2-5. Bidirectional charger control variables and power flow equations. 20

Table 3-1. System Parameters 46

Table 4-1. Simulation ki and kp values 49

Table 4-2. Bidirectional charger simulation parameters summary. 50

Table 4-3. Steady state response base values. 51

Table 4-4. Step-response plot parameter scaling. 59

Table 4-5. Step-response plots P,Q requests vs time. 59

Table 5-1. SN8200 EVK+ WiFi module evaluation kit specifications 65

Table 5-2. Battery Pack Specifications 66

Table 5-3. TMS320F2808 evaluation board product specifications. 66

Table 5-4. Steady-state response experimental results summary. 72

Table 5-5. Prototype step response P-Q request summary. 76

Table 5-6. Efficiency calculations. 78

Table 5-7. Smart Charger bill of materials. 80

Acronyms

2G	Second Generation
3G	Third Generation
4G	Fourth Generation
AC	Alternating Current
C	current required to completely deplete a battery
CC-CV	Constant Current - Constant Voltage
CP	Pilot Circuit
DC	Direct Current
DOD	Depth of Discharge
DR	Distributed Resource
DSL	Digital Subscriber Lines
EV	Electric Vehicle
EVSE	Electric Vehicle Supply Equipment
G2V	Grid-to-Vehicle
GHG	Greenhouse Gas
HAN	Home Area Network
ICE	Internal Combustion Engine
LAN	Local Area Network
LDC	Local Distribution Company
PC	Personal Computer
PCB	Printed Circuit Board
PCC	Point of Common Coupling
PHEV	Plug-in Hybrid Electric Vehicles
PLC	Power Line Communication
PP	Proximity Circuit
P-Q	Active Power - Reactive Power
PWM	Pulse Width Modulation
PWM-CC	PWM-Current Control

SAE	Society of Automotive Engineers
SOC	State of Charge
SOH	State of Health
TDD	Total Demand Distortion
UPF	Unity Power Factor
V2G	Vehicle-to-Grid
VSC	Voltage Source Control
WAN	Wide Area Network

Chapter 1
Introduction

1.1 Motivation

With the increasing public awareness that the transportation sector is one of the largest contributors to Greenhouse Gas (GHG) emissions [1], an increasing number of households are deciding to purchase Electric Vehicles (EV) or Plug-in Hybrid Electric Vehicles (PHEV) as their primary means of transportation. Compared with a traditional Internal Combustion Engine (ICE) vehicle, EVs only contribute to the worlds GHG problem if the electricity used to power the car were created from a non-renewable resource. Over time, as the world moves away from fossil fuels and towards renewable resources such as wind, solar and hydro, EVs will become part of the solution to the GHG problem. Furthermore, government incentives, the realization that petroleum reserve is finite [2] and the ever increasing costs of oil [3], all add to the growing demand of EV/PHEVs. This, EPRI estimates that by 2020, 35% of all vehicles on the road will be EV/PHEVs [4].

Although good for the environment, EVs will significantly affect the power grid. The Tesla Model S requires an 85 kWh battery pack to travel 500 km and takes anywhere from 1 hour to over 24 hours to fully charge, depending on the charge rate [5]. Over time, it can only be assumed that EV manufacturers will be providing consumers with the ability to charge at 20 kW or more from home in

order to compete with ICE vehicles, which take about 1 minute and can provide more than 500 km of range. Currently, EV owners can charge up to 19.2 kW from home with a special installation, which more than doubles the typical Ontario household power draw [6]. EV loads are also quite variable [7], meaning they can draw a lot of power for a short period of time and not always in the same place. Thus, one can imagine a scenario where many EV owners drive into the city for work in the morning, charge all their EVs at the same time, drive home in the evening and do the same thing. In this scenario, the aggregated EV load is shifting from the city to the suburbs, straining both the urban and suburban distribution networks EVs may also disrupt distribution systems by overloading transformers and cable feeders, causing phase imbalances and voltage deviations [8],[9].

If properly controlled and regulated, EVs have the potential to power networks through a concept known as Vehicle to Grid (V2G) [10]. V2G investigations have been conducted, studying its role in future smart grids. The idea is to use the battery as a means of energy storage, charging during low demand times and discharging to the grid when there is a power shortage. This means EVs can be used for peak shaving, deferral of assets, and variability power injection caused by distributed generation resources. However, there are no mass-produced electric vehicles on the market today that carry with them the technology for V2G. The four most prevalent EV/PHEVs on the market today, the Tesla Model S [5], Chevrolet Volt [11], Nissan Leaf [12] and Toyota Prius [13] have only the capacity for Grid to Vehicle (G2V) charging. In order to realize V2G and all the benefits that it carries, a bidirectional charger with proper power electronics, interactive charger control, connection to the grid for communication and smart metering capabilities will be required [14].

1.2 Literature Review of Smart EV Chargers

Over the last decade, the widespread adoption of EVs in the market has motivated much research in the area of bidirectional EV chargers. These are a popular topic of discussion in power system engineering because of the many benefits outlined in the preceding section. Two types of research areas have emerged with respect to bidirectional EV chargers. The first type concerned with power electronics and control, which concentrates on charger topologies and control strategies necessary to achieve V2G and G2V functionality, while reducing harmonics, steady state error, component size and cost. The second is concerned with coordination, communication and control. In this context, parameters such as system stability, peak shaving and coordinated charging of EV fleets are of concern. Very few papers have been written which tie both of these areas together, unless it is a qualitative discussion with no experimental

results. The review discusses the existing research charger topologies and smart grid communication technologies.

1.2.1 Bidirectional EV/PHEV Battery Charger Topologies

Almost all authors who have done research on bidirectional charges unanimously agree that two stage topologies have a significant advantage over single stage topologies. A single stage topology includes only an AC/DC conversion stage, whereas a two-stage includes an AC/DC converter followed by a DC/DC converter (most commonly a buck-boost converter). Two stage topologies are advantageous because they can typically support more than one charging level with improved performance over their single stage counterpart [15]. Papers [16],[17], and [18] all independently come to this same conclusion, using some form of a full-bridge AC/DC converter to charge a DC link capacitor, followed by a DC/DC converter to facilitate controlled battery charging/discharging. The unique aspect of each of these papers is in the AC/DC converter employed to achieve bidirectional functionality. The review that follows focuses on two stage topologies, emphasizing the AC/DC converter topology and control strategy.

In [19], bidirectional battery chargers are investigated, where a three level PWM AC/DC converter based on neutral point clamped control scheme is proposed. An inner loop controller is used to regulate current, while an outer loop voltage controller regulates the DC link voltage. The feasibility of bidirectional operation is demonstrated through experimental results, but only at unity power factor, without reactive power control. In [20] the authors discuss a bidirectional single phase half-bridge rectifier for power quality compensation. The topology employed is a single phase half-bridge rectifier with a clamped capacitor, requiring a flying capacitor and four power switches. The controller is a hysteresis current controller with a DC link voltage regulator to balance the neutral point voltage, and track line current to maintain a constant DC bus voltage. This bidirectional charger improves upon the first one, since it is able to perform shunt active power filter operation and eliminates harmonic currents and compensates the reactive power contributed by the non-linear load. However, similar to the first design, reactive power control is not considered.

In [21], the authors provide simulation and experimental results for a multifunctional bidirectional charger. The topology employed is a split-phase three leg converter with protective earth connected to one of the legs. A new type of controller is employed: the Proportional-Resonant (PR) controller, in which resolves the issue of DC currents being injected into the grid, keeping the output current sinusoidal when operating in V2G mode. This PR controller is able to reduce steady-state error more effectively than the commonly used PI controller. Through simulation, the authors prove the validity

of bidirectional power flow at unity power factor for both charging and discharging, with low harmonics and zero steady state error. However, the experimental implementation is a low power version with noticeable 9^{th} order harmonic in the current waveform; this design does not employ any means of reactive power control either.

In [22], the implications of V2G reactive power operation in terms of component size, voltage and current levels are assessed. In this paper, no controller is offered, but various topologies are evaluated and reactive power operation design equations are presented. It concludes that the dual-buck and half-bridge AC/DC converter requires the most increase in DC link capacitance to make reactive power operation suitable, and therefore a full bride AC/DC converter is shown to be the best choice. This paper is followed up by [23], where experimental results are presented using a PR controller to regulate the utility line current with a full bridge AC/DC converter; results for charging, charging while receiving reactive power and charging while delivering reactive power are demonstrated. These results validated the findings in the earlier paper, and proved that it is possible for the charger to operate in all four quadrants of the P-Q plane; however, discharging operation is not experimentally validated.

1.2.2 Smart Grid Communication Technologies

To the thesis author's knowledge, no one has developed a bidirectional charger capable of third party control through existing smart grid communication technologies. This section will present a general review of such technologies and where they fit into smart bidirectional chargers.

To realize the communication requirements of a smart charger, which will be part of the smart grid, various communication technologies must be reviewed based on reliability, security and cost. A two way integrated communication system is a critical component of a smart charger, since it facilitates wide area sensing, links to the customer, data logging, and safety mechanisms. BC Hydro has already launched a Smart Metering and Infrastructure Program to facilitate smart grid implementation to include, among other things, advanced smart meter applications and a Wide Area Network (WAN) [24], where the WAN aggregates data from various advanced applications such as substations or mobile data as well as Local Area Networks (LANs). These LANs are composed of feeder/transformer meters, smart grid devices and customer meters which aggregate the data from a Home Area Network (HAN), which aggregates the data from Smart Meters, PCs, heavy duty appliances, and smart chargers.

The smart grid can be summarized as a modern electric power grid infrastructure for improved efficiency, reliability and safety, with smooth integration of renewable and alternative energy sources through automated control and modern communication technologies [25]. In countries such as Canada

and the United States, projects are already in place to see the realization of a smart grid [26], which means that the required communication networks are either available or will be very soon. HANs in smart grid applications have data flowing from the sensor or appliance to the smart meter. The data then travels up to the LAN aggregator, and then into the WAN aggregator or utility data center [24]. This line of communication is done with both wired and wireless communications, where typically the HAN communications are wired and the LAN/WAN communications are wireless. Wired communication protocols include Power Line Communications (PLCs) and Digital Subscriber Lines (DSLs), whereas wireless communication protocols include ZigBee, Wireless Mesh and Cellular Networks.

Smart chargers requiring the use of a smart meter have limited use when a smart meter is unavailable. Since the smart charger is mobile, it would be advantageous if it were available anytime it was connected to the grid. Relying on a smart meter means an added level of integration, planning, and coordination at the utility level. In locations where smart meters are not installed or out of commission, smart charging would not be possible. The integration of a smart charger with a smart meter in a HAN is reviewed next.

Power Line Communication (PLC)

PLC is the most dominant communication technology for smart meters, since a direct connection to the meter is already in place, thus capital costs are low [27]. The smart charger could either communicate directly with the utility data center over the power line charging the vehicle, or link to the smart meter in the HAN. The primary appeal of PLC is that the infrastructure is already in place, since any outlet can be considered as a communication port. However, since PLC networks are broadcast in nature, security issues are a concern [28].

Due to the sometimes harsh and noisy environment of the power line, the data transmission rates can be as low as 20 kb/s [26]. However, companies specializing in PLC are developing chips that can support data transmission rates up to 400 Mb/s [28]. Moreover, the number of devices connected to the power line and the length of the data transmission can further affect the signal quality and ultimately the reliability [29]. Based on all these drawbacks, standalone PLC is not well suited for high speed data transmission, and is usually coupled with another communication technology to improve upon its flaws.

Digital Subscriber Lines (DSL)

DSL is a general term encompassing a family of technologies that transmits data over local telephone networks. Since much of the infrastructure is already installed in urban areas, installation costs are low. However, in many rural areas where DSL has not yet reached, installation costs are high or installation is

infeasible [26]. The bit rates can range from 256 kb/s up to 1 Gb/s in some trials [30]. However, during heavy usage periods, the transmission rate can significantly decrease or the transmission can even be interrupted making the system unreliable [31]. An alternative solution includes dedicated lines for smart grid applications, but, this greatly increases the installation costs since dedicated lines will need to be run to each smart meter. Furthermore, when transmitting data over public DSLs, security will be an issue. A dedicated smart charger outlet will be required for the smart charger, since dedicated data lines will need to be added to connect the smart charger to the smart meter.

ZigBee

A mesh network has no centralized controller but rather relies on many low powered devices that can relay information to each other to transmit data over long distances. Zigbee is used here as an illustrative example of mesh networks, since it is the most commercially available mesh network protocol for HANs. ZigBee is a wireless mesh network communication standard most commonly seen in HAN smart grid applications.

ZigBee is a low power, low data solution where data transmission rates only go as high as 250 kb/s and can be transmitted up 50 meters [32]. The nature of the mesh networks makes ZigBee an ideal solutions when there are many ZigBee enabled devices in close proximity that transmit low amounts of data. For example, a study done in [33] demonstrates the potential of a ZigBee communication platform for controlling the charging of PHEVs at a municipal parking deck, and [34] develops a digital test bed using ZigBee, among other communication platforms, to evaluate various charging strategies.

Some drawbacks of Zigbee include low processing capabilities, small memory size, delay and interference requirements [26]. ZigBee also shares the same 2.4 GHz band as IEEE 802.11 which has a WiFi communication line at 2.4 GHz. This raises reliability concerns, especially in HANs where a WiFi router is almost guaranteed [32]. The close proximity nature of ZigBee means a ZigBee enabled smart charger would need to communicate with a ZigBee enabled smart meter to relay the information to the utility data center for analysis and control.

Cellular Networks

“Cellular networks” is a broad inclusive term encompassing, among others standards, 2G, 3G, 4G, WiMAX and LTE. Using cellular networks as the communication medium between a smart charger and utility data center allows taking advantage of the latest updates in security and bandwidth capabilities. The upfront installations costs are extremely low, since the entire network is already in place and maintained by the telecommunication companies. One drawback is that in order to transmit data over long

distances, power requirements exceed that of any of the other technologies reviewed. However, since a smart charger will only operate when connected to the grid, this will not be a concern and will not affect the lifetime of the vehicles battery [35]. Additionally, depending on the network available, data transmission rates can be as high as 2 Mb/s or as low as 14.4 kp/s [26]. With the widespread availability of cellular networks, a smart meter will not be required and the smart charger can communicate directly with the utility data center, making smart charging available anytime the vehicle is plugged in.

A qualitative summary of the communication technologies reviewed is shown in Table 1-1. The colors in the table indicate the positive features of the technology.

Table 1-1. Smart charger communication technologies.

Communication Technology	Reliability	Cost	Security	Bandwidth	Smart Meter Required?
PLC	low	low	low	high	yes
DSL	medium	low	medium	high	yes
ZigBee	medium	medium	medium	low	yes
Cellular Networks	medium	low	high	high	no

1.3 Research Objectives

As discussed in the previous section, the evolution of the bidirectional chargers is beginning to move away from theory and into a reality. The early pioneers of this subject focused their labour towards proving that bidirectional power flow on EV battery chargers was possible, through simulation and simple experimental tests. These prototypes focused on designing chargers capable of bidirectional flow at unity power factor, and cannot be considered “smart”. To these bidirectional chargers, reactive power control was added, allowing the charger to charge or discharge at any power factor. The major emphasis was towards developing design equations and proving the concept through simulation. Experimental prototypes were developed, but not in V2G mode. These prototypes also did not implement communication protocols to allow third party control, focusing mainly on the arrangement of power electronics and the control strategy.

From the above discussion, the next step is to implement a fully functional smart bidirectional charger prototype, which is the main focus of this thesis, and is referred to as Smart Charger for the remainder of this document. The developed Smart Charger prototype will:

- employ a two stage topology, rated at 1.92 kVA, capable of operating in all four quadrants of the P-Q plane;
- be connected to a battery pack and tested in the lab to validate its ability to operate in all four quadrants of the P-Q plane at rated power; and
- contain a wireless network controller to demonstrate how an EV aggregator or LDC would be able to control a fleet of Smart Chargers.

1.4 Thesis Outline

The rest of this thesis is structured as follows:

Chapter 2 focuses on giving the reader the required background information to understand the subsequent chapters, starting with a review of relevant standards (SAE J1772 and IEEE 1547). Market dominant lithium-ion are discussed, including how they are charged, their limitations, cell balancing, and battery management systems; a relevant battery model is also presented. The chapter concludes with a discussion of synchronous and stationary frame AC/DC controllers.

Chapter 3 will focuses on the design process of the Smart Charger. It begins with a chosen topology and battery model to be used in the simulations. Next, reactive power controllers are developed, which are based on the AC/DC controllers discussed in Chapter 2. This is followed with a discussion of active power controllers, and it concludes with a discussion of the optimal sizing of the charger components.

Chapter 4 presents the simulation results of the charger designed in Chapter 3, showing and discussing various results for step and steady-state responses. Chapter 5 presents an implementation of the prototype Smart Charger, which includes the Smart Charger control board, smart grid communication controller, battery pack, and central control unit. The step and steady state response scope shots are presented, concluding with efficiency analysis, a comparison between the simulated and experimental results, and the final bill of materials. Finally, Chapter 6 presents a summary, and contributions, of the thesis, and briefly discusses possible future work.

Chapter 2
Background Review

This chapter will provide the reader with the required background information necessary to understand the subsequent chapters. Relevant standards will be presented which will form the basis of the design requirements and constraints. Next, lithium-ion batteries are reviewed, including the battery model, charging strategies, limitations and cell balancing. Finally, two of the most prevalent non-predictive linear AC/DC controllers are presented.

2.1 Relevant Standards

A bidirectional Smart Charger is capable of bidirectional power flow. SAE J1772, developed by the Society of Automotive Engineers is a standard for electric vehicle charging but considers only unidirectional power flow. When a bidirectional charger is providing power to the grid, it is considered as a distributed energy source and therefore must adhere to IEEE 1547, which establishes the criteria and requirements for interconnection of distributed resources in electric power systems.

2.1.1 SAE J1772

In North America, the Society of Automotive Engineers developed a standard for electrical connectors of Electric Vehicles (EV). This standard, known as SAE J1772, outlines the required EV equipment, Electric Vehicle Supply Equipment (EVSE), connectors, charger ratings and safety. The EVSE serves as the link between the grid and the EV charger, adding an extra level of security and ensuring a signaling protocol between the vehicle and supply equipment. The signaling is done over the Pilot Circuit (CP) and Proximity Circuit (PP) lines. The addition of these two lines means that all J1772 connectors must have five pins: mains 1, mains 2, protective earth, CP and PP [6].

Three charging levels have been defined by SAE and they are summarized in Table 2-1. Level 1 charging has the lowest rating available and can plug into any 120VAC outlet. Due to its low power rating a Level 1 EVSE is typically small and light enough to be stored in the vehicle, so that it may be charged anywhere a 120VAC outlet is available. In Ontario, most residential homes allow no more than 20A to be drawn from any outlet without the circuit breaker tripping, making this an easy solution for charging at home. The primary drawback of this type charging level is long charging times, for example, the 2014 PHEV Chevrolet Volt has a battery capacity of 16 kWh [36], and the control strategy does not allow the SOC of the battery to drop below 20% unless the gas tank is empty; hence to charge this vehicle from 20% to 100% SOC would take over 6.5 hours. This level of charging is not ideal for pure EVs since there is no engine to extend the vehicles range.

Table 2-1. SAE J1772 charging levels.

Charging Level	**Level 1**	**Level 2**	**Level 3**
Type	AC	AC	DC
Phase	Single	Single/Three	N/A
Voltage (V)	120	208-240	480
Peak Current (A)	16	80	120
Peak Power (kW)	1.92	19.2	57.6
Structure	On-board	On-board	Off-board

Level 2 charging is similar to Level 1 but more powerful. Since these chargers can charge up to 19.2kW, the Level 2 EVSE is much larger than the Level 1 EVSE, and often too large to carry in the vehicle. Level 2 EVSEs are most commonly found in public charging stations, although they can also be installed at the owner's home as well, with the help of an electrician. Similar to the Level 1 charger, the Level 2 charger is an on-board charger and today most on-board chargers can operate as either a Level 1 or Level 2, such as the GM Voltec EV Charger [37]. Charging a Chevrolet Volt from 20% to 100% SOC

could be done in just over 30 minutes; however, the charging current is limited by the on board charger of the Volt.

Level 3 chargers are capable of charging at a rate of 57.6 kW and do not require an onboard charger. The AC/DC conversion process is done off-board and DC current is fed directly into the battery. These types of chargers are not available in residential neighborhoods and are only found at special charging stations. Additionally, not all vehicles are designed to work with Level 3 chargers since the fast charging time can potentially damage the battery. Tesla has recently been deploying Supercharging stations across North America, Europe and Asia which have the capability to charge the Tesla Model S at 120kW [38]; these Superchargers cannot be considered Level 3, but use a similar method of converting the power to DC off-board and charging the battery directly. Theoretically, a Volt would charge its battery from 20% to 100% SOC in 20 minutes. These types of chargers are ideal for pure EVs with larger battery packs in place of a range extending engine.

2.1.2 IEEE 1547

IEEE 1547 provides interconnection specifications and requirements for the interconnection of distributed resources with electric power systems at the Point of Common Coupling (PCC). To behave as a distributed energy source, the Smart Charger must follow the requirements set forth in the standard, most notably the response time to abnormal voltages and frequencies and current distortion limits [39]. A summary of these requirements is specified in Table 2-2, Table 2-3 and Table 2-4. The maximum permissible TDD for a Distributed Resource (DR) is 5.0%

Table 2-2. Distributed resource interconnection system response to abnormal voltages [39].

Voltage Range (% of base voltage)	Clearing Time (s)
$V < 50\%$	0.16
$50\% \leq V \leq 88\%$	2.00
$110\% \leq V \leq 120\%$	1.00
$V \geq 120\%$	0.16

Table 2-3. Distributed resource interconnection system response to abnormal frequency [39].

Frequency Range (Hz)	Clearing Time (s)
> 60.5	0.16
< 59.3	0.16

Table 2-4. Distributed Resource Maximum Current Distortion [39].

Harmonic Order	h<11	11≤h<17	17≤h<23	23≤h<35	35≤h
Percent (%)	4.0	2.0	1.5	0.6	0.3

2.2 Lithium Ion Battery Technology and Charging Controllers

Lithium-ion batteries are dominating the EV/PHEV market today. As of June, the year-to-date 2014 top selling EV/PHEVs were the Nissan Leaf, Tesla Model S, and Chevrolet Volt [40], all of which use lithium-ion batteries in their design [12],[41],[36]. Compared with other battery types such a lead-acid or nickel-metal-hydride, they provide the most energy and power output for the least weight [42], making lithium-ion batteries the obvious choice as an energy storage device.

Some notable battery nomenclature includes: State of Charge (SOC), which is the amount of charge remaining in the battery; Depth of Discharge (DOD), which is the amount of charge that has been depleted; cycle life, which is the number of times a battery can go from 100% SOC to 100% DOD to 100% SOC before it is unusable; storage capacity, which is the total energy available when fully charged; State of Health (SOH), which is the total capacity of the battery as a percentage of the original capacity; and charge/discharge rate, which refers to the rate (in amps or watts) at which the battery can be charged or discharged. Battery manufacturers typically discuss the charge/discharge rate in terms of C, where C is the current required to completely deplete a fully-charged battery in 1 hour; for example, in a 40 Ah battery, C = 40 and in a 100 Ah battery, C = 100.

2.2.1 Battery Model

Modelling battery technologies has been an area of much focus in both industry and academia. Many lithium-ion batteries found in smart phones and electric vehicles are based very much on the same technology. For example, the Tesla Model S 85 kWh battery pack contains 18,650 3.3V lithium-ion cells [43]. In fact, much of the literature today focuses on developing an accurate model of one cell, then expanding that model to include the total number of cells in the battery pack [44]. However, these models are difficult to use in simulations because they are either too analytical [45], or highly complex, requiring

excessive computational resources [46]. An electrical circuit model for a single lithium-ion cell has been developed in [47], and a simplified diagram is shown in Figure 2-1.

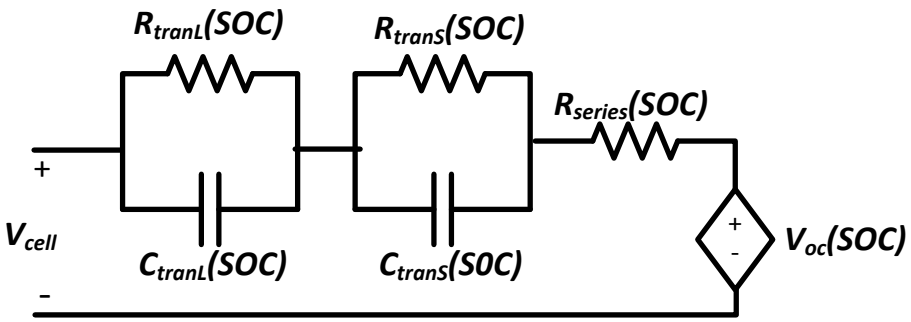

R_{tranL}	long time constant resistive term
C_{tranL}	long time constant capacitive term
R_{transS}	short time constant resistive term
C_{transS}	short time constant capacitive term
R_{series}	battery cell series resistance
V_{oc}	open circuit cell voltage
V_{cell}	cell terminal voltage

Figure 2-1. Lithium ion cell electrical model.

Every parameter in the model is a function of SOC through an exponential relationship where the resistive terms of Figure 2-1 decease as SOC increases, capacitive terms increase with SOC, and the open circuit voltage increases with SOC. Figure 2-2 and Figure 2-3 show the charge and discharge curves of a lithium-ion cell developed by Elite Power Solutions where 1 C = 100 A. These figures allow to determine the model parameters; note that for larger charging C, the cell voltage is greater, and for large discharging C, the cell voltage is lower, and also as the SOC increases, as VOC increases as well.

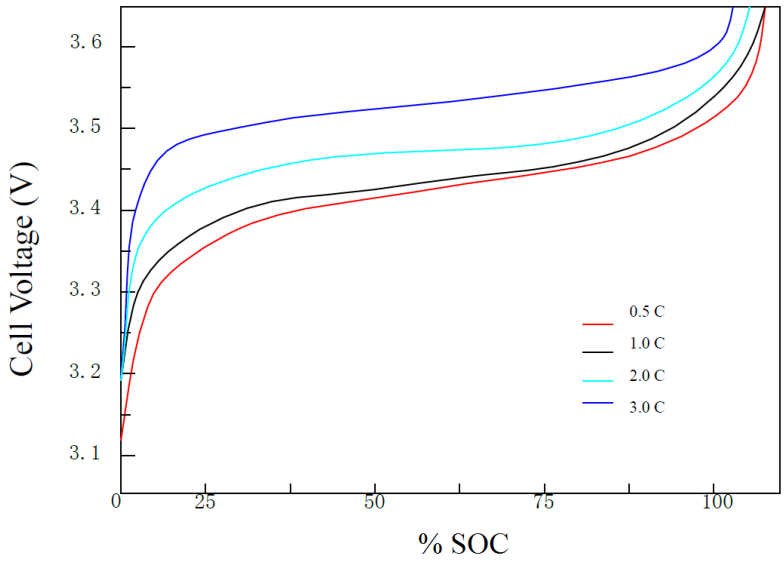

Figure 2-2 Cell charging curve [48].

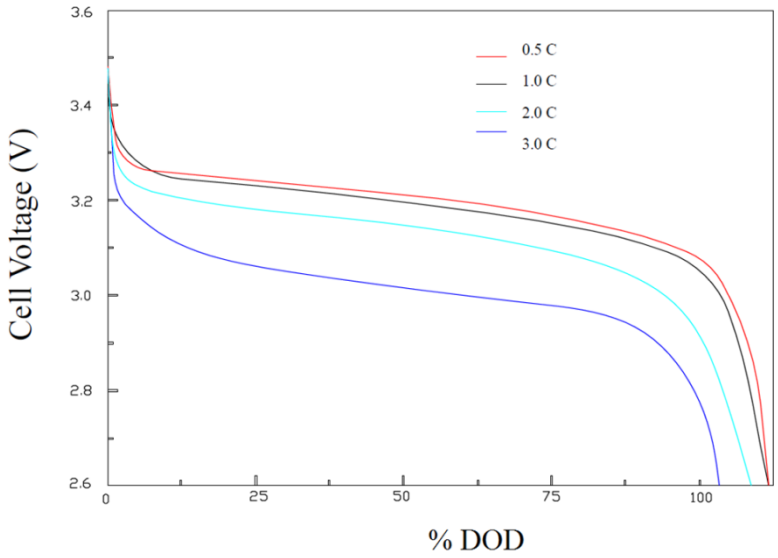

Figure 2-3. Cell discharging curve [48].

2.2.2 Constant Current, Constant Voltage Charging

A common and well known method of charging batteries is through an algorithm known as constant current, constant voltage charging (CC-CV). Various hybrids of this control strategy exist, such as multi-stage constant current charging, pulse current charging, and fuzzy logic control. Depending on the

application, various control strategies can be used to decrease charge time, minimize battery temperature rise, or extend battery life [49]. The profile of a 40 Ah, 105 V li-ion battery pack charging from 5% SOC to 95% SOC is shown in Figure 2-4; During the constant current charging phase the charging current is fixed at 13.5 A. Once the pack voltage reaches 115.2 V, the controller then switches into constant voltage charging, maintaining the pack voltage at 115.2 V; at this point, the charging current begins to drop until the charging current falls below 1 A.

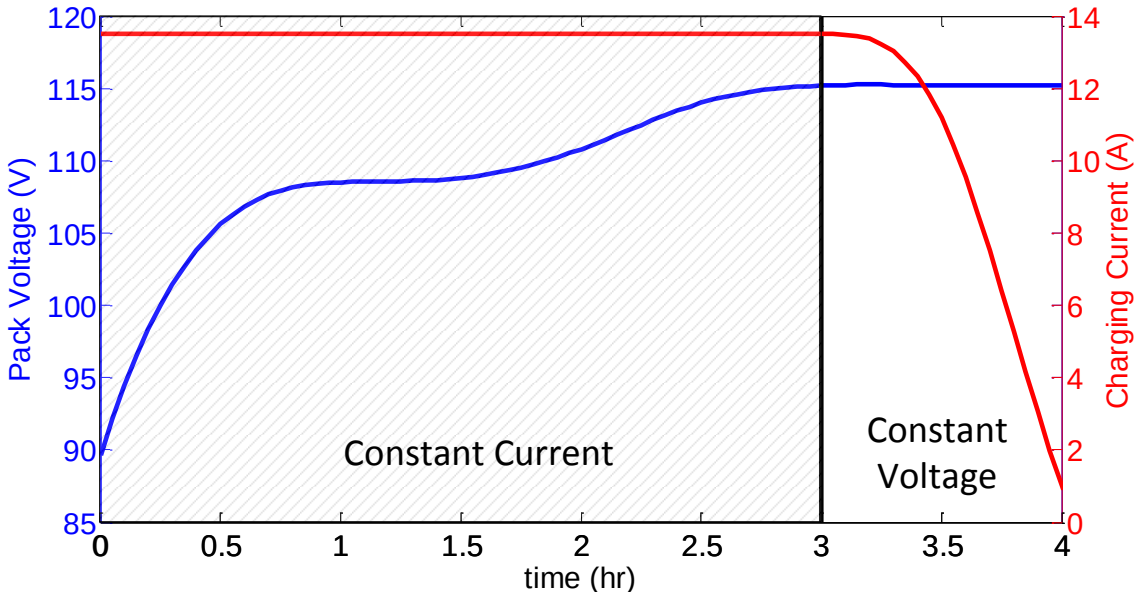

Figure 2-4. Charging profile of 40 Ah 32 cell, 105.6 V li-ion battery pack.

Employing the CC-CV control strategy is very straightforward, and the control block diagram is shown in Figure 2-5. During the CC charging phase, a reference current is chosen (typically C/3 to maintain long battery life) and compared with the measured current; the error is then fed into a PI regulator to produce the modulating voltage for the PWM controller. The terminal voltage of the pack is monitored until the average cell voltage reaches 3.6V, at which point the controller moves into the CV charging phase, using the terminal voltage as the feedback term; the reference voltage is the number of series cells multiplied by 3.6V. The charging current will continue to decrease until it reaches about 0.05C, at which point the charger will stop charging the battery to prevent overcharging and damage to the battery.

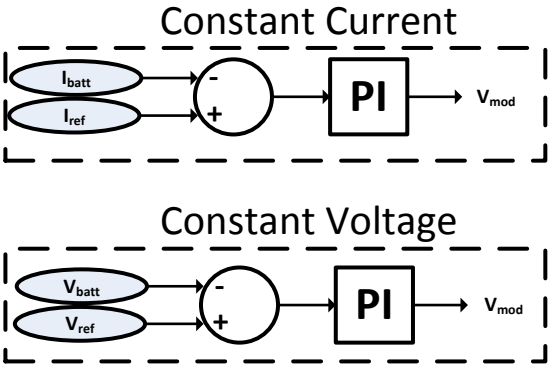

Figure 2-5. CV, CC charging control block diagram.

2.2.3 Battery Limitations and Degradation

Over charging and over discharging can lower the SOH of a battery. Most chargers will purposely charge a battery to 80% SOC and only allow it to be discharged to 20% to maintain a longer useable life. Figure 2-6 shows a battery life test done by Elite Power Solutions where they fully charged and then discharged a 40 Ah battery, measuring its SOH after every charge; after 2000 cycles the SOH drops to 76%.

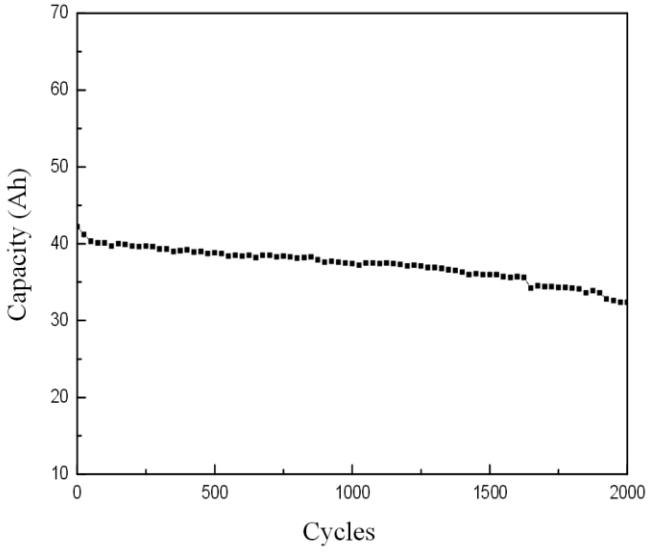

Figure 2-6. Battery life degradation, 40 Ah pack 100% SOC to 100% DOD [48].

2.2.4 Cell Balancing and Battery Management Systems

Today's PHEVs and EVs typically have a battery pack voltage between 250 and 450V, with li-ion batteries, having over 1000 cells in a vehicle's battery pack. Cell balancing is of special concern with li-ion batteries in hybrids, since repetitive charging and discharging from accelerating and regenerative breaking can cause cell imbalances and ultimately decrease the SOH of the battery [50]. For this reason, cell balancing is a very important and integral part of any li-ion battery. This is facilitated by a Battery Management System (BMS) which connects, typically in sequence, to a sensor on each cell which monitors voltage and temperature. Most BMS types will actively balance the cells, while charging and continuously monitoring various battery processes as well, which include: ground fault detection, thermal management, CAN communication, SOC estimation, overvoltage/undervoltage protection, and overcurrent protection [51].

It is important that the battery charger communicates with BMS so that if a fault occurs, charging can stop before the battery is damaged. Additionally, since the BMS estimates the SOC, this parameter can be read by the charger and used in the charging algorithm without the need for the charger to do the calculation.

2.3 AC/DC Controllers

Today, most applications of PWM Voltage Source Converter (PWM-VSC) use a PWM-Current-Control (PWM-CC) technique. PWM CCs available for single phase VSCs can be divided into two groups: linear and non-linear. Since the control system in question can be governed by the superposition principle, linear control is investigated further here: This can be divided into non-predictive and predictive control, as shown in Figure 2-7. Linear PI stationary and synchronous frame controllers are considered here as the primary candidate control strategies, since they are easily simulated and implemented with a digital controller. Some benefits of PWM-CC include: instantaneous control of current, good dynamics, compensation of semiconductor voltage drop, switch dead time, DC-link voltage changes, and AC-side voltage changes. [52]

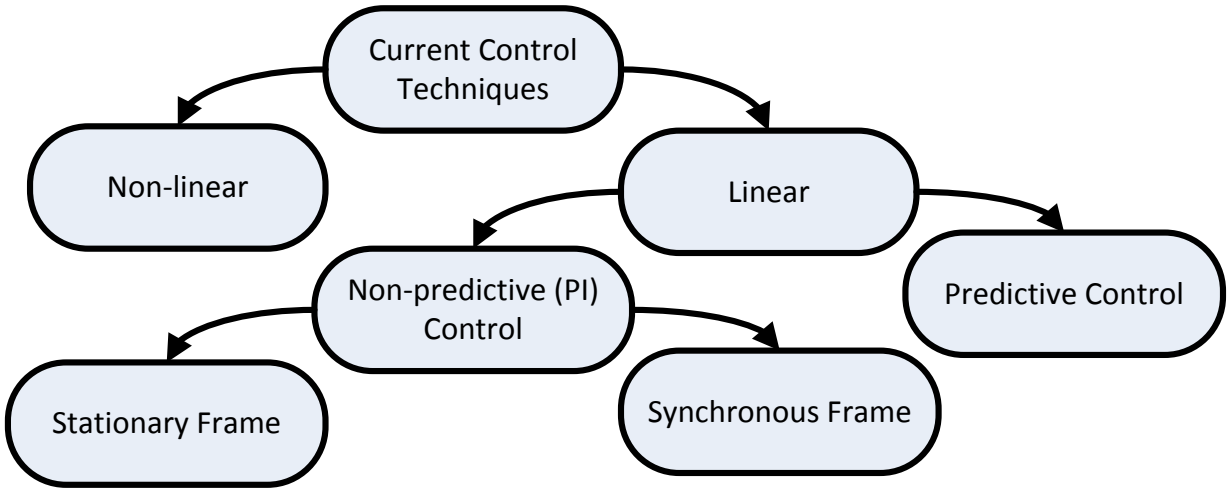

Figure 2-7. Breakdown of VSC current control techniques.

Much of the literature available on this subject agrees that the two top choices for linear non-predictive control are the stationary frame Proportional-Resonant (PR) controller and the synchronous frame Direct-Quadrature (DQ) controller[16],[53],[54]. This section will provide background information on these two controllers, focusing on control at unity power factor, with the analysis and design of reactive power controllers being presented in Chapter 3.

2.3.1 Control Variables and Operating Modes

One common attribute shared among all VSCs is the coupling inductor between the grid and the switches. If one assumes the grid voltage v_s to be a perfect sinusoid and the coupling inductor L_c to have no resistance, then any four quadrant topology can be simplified into the system shown in Figure 2-8, where v_c is the fundamental component of the voltage at the input of the AC/DC converter. As such, if v_c and δ are used as the control variables, where δ is the angle between v_s and v_c, then the power flow equations can be derived as given in Table 2-5.

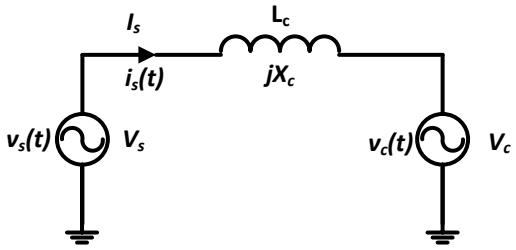

Figure 2-8. Charger-grid connection.

Using v_c and δ as the primary control variables is difficult, since v_c is not easily measured. Additionally, it is important that the charger complies with IEEE 1547, which specifies the maximum current harmonics that may be injected into the grid by a distributed resource. By controlling i_s and θ, where θ is the phase angle of i_s, a hysteresis band current control through PWM can be used to regulate the current waveform [55]. Therefore, controllers using I_s and θ will be investigated and reviewed further here.

Table 2-5. Bidirectional charger control variables and power flow equations.

Control Variable	P	Q
v_c , δ	$\frac{V_s V_c}{X_c} sin\delta$	$\frac{V_s^2}{X_c}\left[1 - \frac{V_c}{V_s} cos\delta\right]$
i_s , θ	$V_s I_s cos\theta$	$V_s I_s sin\theta$

2.3.2 Stationary Frame PR Controller

The PR controller is a hybrid of the stationary frame two-loop Unity Power Factor (UPF) controller shown in Figure 2-9. The two loop controller is the simplest way to control a single phase VSC. A slow outer loop regulates the voltage across the DC link capacitor V_{DC}, and a fast acting inner loop controls the sinusoidal grid current i_s. The error term generated in the V_{dc} control loop is fed to a PI regulator, and then multiplied by the normalized grid voltage, resulting in a reference for the current waveform. An alternative approach found in the literature is to use an angle detector for the grid voltage to generate a waveform in phase with the grid voltage [44], with the error term of the grid current being fed into a PI regulator to generate the modulation voltage. Although easy to implement, the main drawback of this controller is the non-zero steady state error generated on the DC bus and unwanted phase shifts [56].

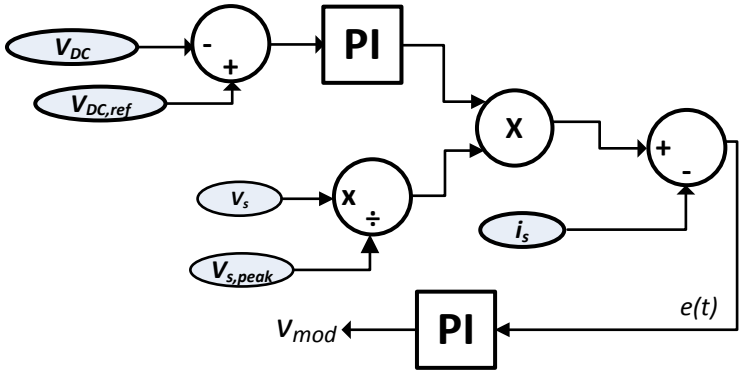

Figure 2-9. Two-loop UPF controller block diagram.

To address the aforementioned issue, a two-loop PR controller has been developed and presented in [57], which is shown in Figure 2-10. For a stationary frame controller, the steady-state error is dependent on the open-loop DC gain, and since this system is dealing with AC quantities, the system is subject to steady-state error. To resolve this issue, the integrator term in the final PI regulator is replaced with a hybrid regulator and the proportional term $I_{s,kp}$ is implemented outside the regulator.

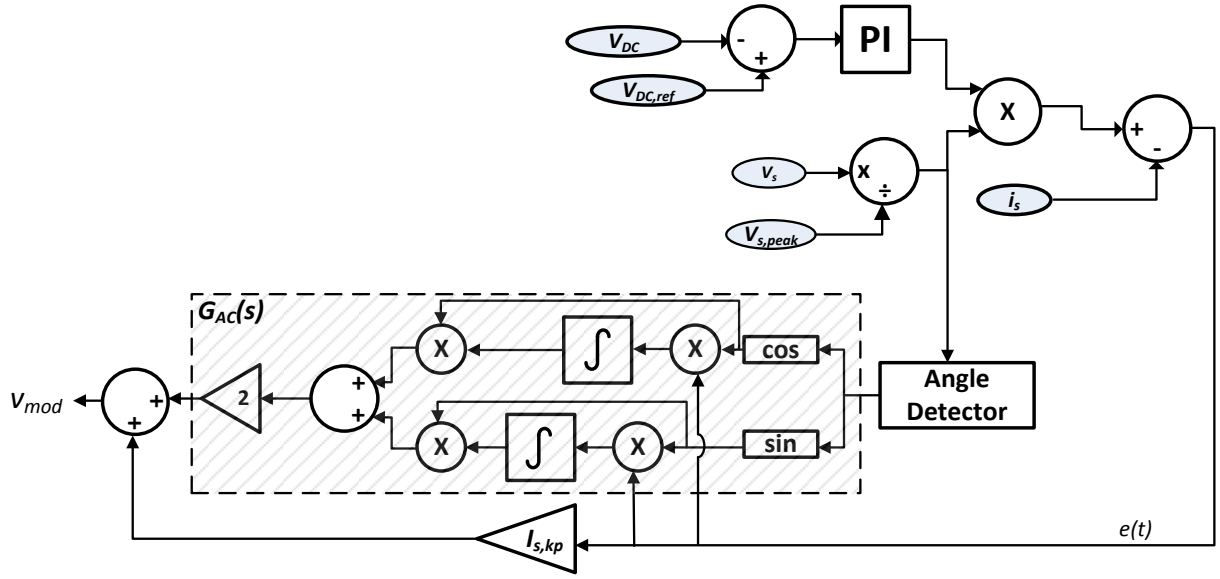

Figure 2-10. PR controller block diagram.

The hybrid regulator G_{AC} in Figure 2-10 multiplies the error term $e(t)$ by sine and cosine functions synchronized with the grid as follows:

$$e_c(t) = e(t) \cdot \cos(\omega_o t) = e(t) \cdot \frac{e^{j\omega_o t} + e^{-j\omega_o t}}{2}$$
$$e_s(t) = e(t) \cdot \sin(\omega_o t) = e(t) \cdot \frac{e^{j\omega_o t} - e^{-j\omega_o t}}{2} \quad (2.1)$$

Taking the Fourier Transform yields the following where it can be seen that for $\omega = \omega_o$, information is present at DC and at double the fundamental frequency:

$$E_c(\omega) = \frac{1}{2}[E(\omega + \omega_o) + E(\omega - \omega_o)]$$
$$E_s(\omega) = \frac{1}{2j}[-E(\omega + \omega_o) + E(\omega - \omega_o)] \tag{2.2}$$

Assuming no phase shift at the fundamental frequency, by low pass filtering (2.2), and then performing the Inverse Fourier Transform, yields:

$$e_{cf}(t) = \frac{1}{2}E_1 \cdot \cos(0) = 0.5E_1$$
$$e_{sf}(t) = \frac{1}{2}E_1 \cdot \sin(0) = 0 \tag{2.3}$$

where E_1 is the amplitude of the fundamental component of the error term. The idea is that the fundamental component now appears as a DC quantity. Hence, by using an integrator in place of a low pass filter, it is possible to drive the fundamental error amplitude to zero, achieving zero steady-state error. Since the integrator is approximating a low pass transfer function, the integrator term is modelled as a non-ideal integrator as follows:

$$\frac{k_i}{s} \rightarrow \frac{k_i\omega_c}{s + \omega_c} \tag{2.4}$$

where the term ω_c represents the controllers cutoff frequency. The signals are then demodulated and added to the proportional term of the control to create v_{mod}. The transfer function for G_{AC} is then [58]:

$$G_{AC}(s) = \frac{2k_i\omega_c s}{s^2 + 2\omega_c s + \omega^2} \tag{2.5}$$

This controller is capable of achieving the same performance as a synchronous controller, i.e., zero steady state error and precise fundamental reference tracking.

2.3.3 Synchronous Frame Dq Controller

Synchronous frame controllers generally dominate current controlled three-phase VSCs, because of their ability to achieve zero steady state error. The idea behind synchronous control is to transform time varying quantities, such as current and voltage, into time-invariant quantities, so that linear control may be performed without introducing steady-state error. In three-phase synchronous machines, the most

common transformation is the abc-dqo transform, which its equivalent in single phase is the following αβ-dq transform, which requires an artificial quantity created in quadrature to the real one:

$$\begin{bmatrix} d \\ q \end{bmatrix} = \begin{bmatrix} cos\theta & sin\theta \\ -sin\theta & cos\theta \end{bmatrix} \begin{bmatrix} \alpha \\ \beta \end{bmatrix} \tag{2.6}$$

If the grid voltage $v_s = v_\alpha$ is the real component, then the fictitious quadrature component v_β is delayed by 90^O with respect to v_α and defined in (2.7).

$$\begin{aligned} v_\alpha = v_s &= \hat{V}_s \cos(\omega t + \sigma) \\ v_\beta &= \hat{v}_s \sin(\omega t + \sigma) \end{aligned} \tag{2.7}$$

If the grid current $i_s = i_\alpha$ is the real component, delayed an angle γ with respect to v_α ; then, the fictitious quadrature component i_β is delayed by 90^O with respect to i_α and defined as follows:

$$\begin{aligned} i_\alpha = i_s &= \hat{I}_s \cos(\omega t + \sigma + \gamma) \\ i_\beta &= \hat{I}_s \sin(\omega t + \sigma + \gamma) \end{aligned} \tag{2.8}$$

If one considers v_α and i_α to be rotating with an angle $\theta = \omega t + \sigma$, then the transformed quantities will be constant DC terms as follows:

$$\begin{bmatrix} V_d \\ V_q \end{bmatrix} = \begin{bmatrix} cos\theta & sin\theta \\ -sin\theta & cos\theta \end{bmatrix} \begin{bmatrix} \hat{V}_s cos\theta \\ \hat{V}_s sin\theta \end{bmatrix} = \begin{bmatrix} \hat{V}_s \\ 0 \end{bmatrix} \tag{2.9}$$

$$\begin{bmatrix} I_d \\ I_q \end{bmatrix} = \begin{bmatrix} cos\theta & sin\theta \\ -sin\theta & cos\theta \end{bmatrix} \begin{bmatrix} \hat{I}_s \cos(\theta + \gamma) \\ \hat{I}_s \sin(\theta + \gamma) \end{bmatrix} = \begin{bmatrix} \hat{I}_s cos\gamma \\ \hat{I}_s sin\gamma \end{bmatrix} \tag{2.10}$$

A Phase Locked Loop (PLL) is required to determine the fundamental frequency, as well as produce a rotating angle θ in phase with the grid voltage. By design, the PLL is part of the dq transform, as shown in Figure 2-11. To keep $V_q = 0$, the phase angle θ must track the reference voltage, therefore producing the desired reference angle.

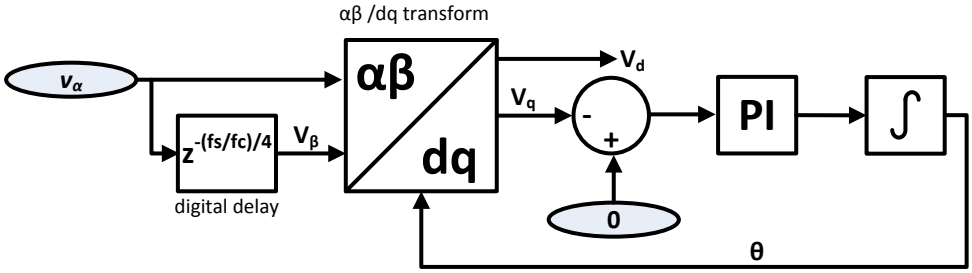

Figure 2-11. PLL for dq transform.

If one considers v_s and i_s to be in the αβ-frame and V_d,V_q,I_d and I_q to be in the dq-frame then the relationship between the variables in the two frames is given by:

$$\begin{aligned} v_s &= V_\alpha + jV_\beta = (V_d + jV_q)e^{j\theta} \\ i_s &= I_\alpha + jI_\beta = (I_d + jI_q)e^{j\theta} \end{aligned} \tag{2.11}$$

where $e^{j\theta}$ represents the rotating nature of the synchronous frame. Referring to Figure 2-8, and assuming L_c to have a small resistance R_c and the full bridge converter to be lossless, the following describes the voltage at the grid interface:

$$v_s - v_c = L_c \frac{di_s}{dt} + R_c i_s \tag{2.12}$$

By substituting (2.11) into (2.12), rearranging to solve for v_c and then separating v_c into its real (V_{c_d}) and imaginary (V_{c_q}) components results in [44]:

$$\begin{aligned} V_{c_d} &= -L_c \frac{dI_d}{dt} + \omega L_c I_q - R_c I_d + V_d \\ V_{c_q} &= -L_c \frac{dI_q}{dt} - \omega L_c I_d - R_c I_q \end{aligned} \tag{2.13}$$

Setting the derivative terms to zero yields the following steady state variables:

$$\begin{aligned} V_{c_d} &= -\omega L_c I_q - R_c I_d + V_d \\ V_{c_q} &= -\omega L_c I_d - R_c I_q \end{aligned} \tag{2.14}$$

The block diagram for a dq-controller operating at unity power factor is given in Figure 2-12. The error term for the DC link voltage V_{dc} is fed through a PI regulator and then used as the reference term for I_D. Meanwhile, to operate at unity power factor $I_Q = 0$ implies that I_s is in phase with V_s, therefore 0 is the reference value for I_Q.

The remaining part of the controller implements (2.14), but must be scaled down by V_{DC} to produce a usable value for v_{mod}. The dq-αβ transform is then performed on these values, v_β is discarded and $v_\alpha = v_{mod}$. Since this controller operates on time-invariant DC quantities, it is able to achieve zero-steady state error, high quality voltage regulation, and is highly resistant to disturbances [44],[59].

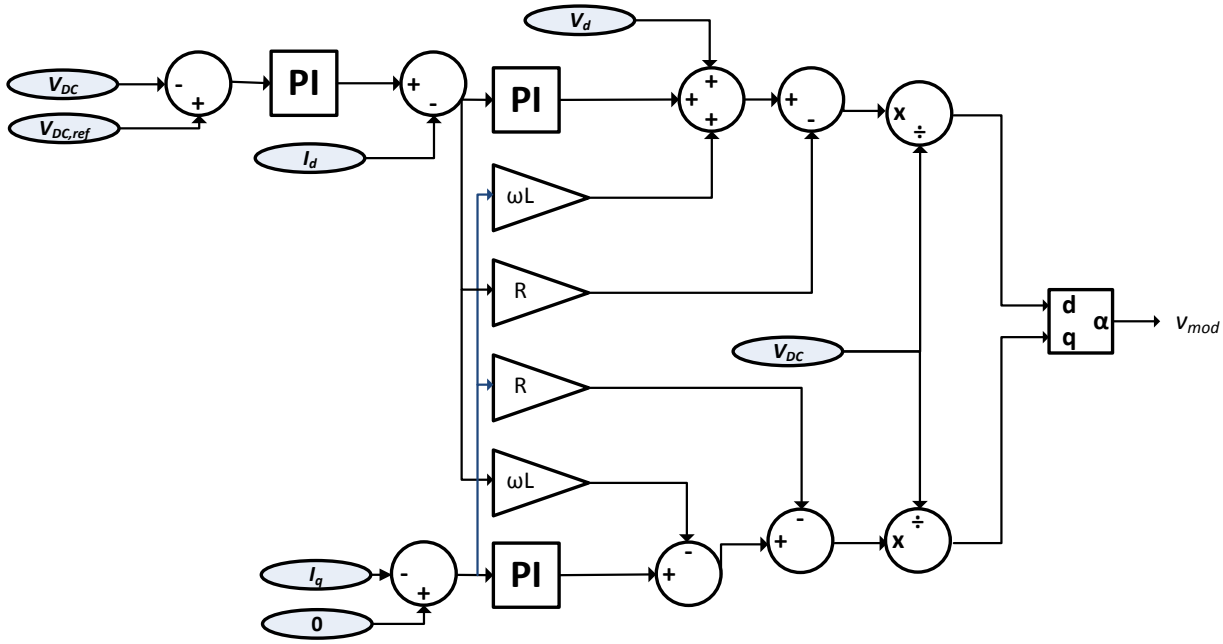

Figure 2-12. Block diagram dq controller.

2.4 Summary

This chapter began with a review of the relevant standards; SAE J1772 for charging operation, and IEEE 1547 for discharging, followed by a review of the battery model, charging algorithm, limitations, and cell balancing techniques of lithium-ion batteries. Finally, a review of existing AC/DC converter controllers was presented, focusing on two well-known control strategies, the single phase dq controller and PR controller.

Chapter 3
Smart Charger Design

This chapter outlines the design process of the Smart Charger. The final topology to be used in the simulations and prototype design is presented. Then, the battery model is added to form a complete model of the bidirectional charger. From there, the PR and dq control strategies are evaluated on the basis of their ability to regulate the DC link voltage and reactive power. A DC/DC controller is developed to control active power flow, and finally, a comprehensive analysis to determine capacitor and inductor sizes concludes the chapter.

3.1 Charger Topology and Battery Model

The P-Q plane discussed in the literature review is shown in Figure 3-1, with four distinct quadrants: charging and inductive; discharging and inductive; discharging and capacitive; and charging and capacitive. To remain consistent throughout the remainder of this thesis, positive P_s will refer to active power flowing into the battery (i.e., charging), and positive Q_s refers to reactive power flowing into the charger (i.e., inductive operation).

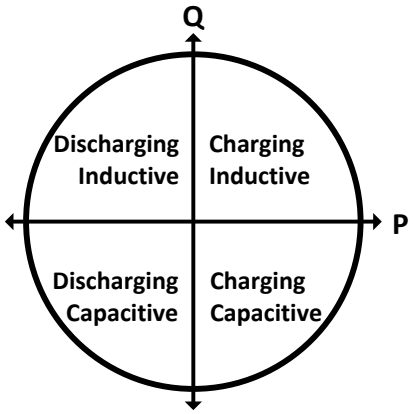

Figure 3-1. Four quadrants of the P-Q plane.

3.1.1 Charger Topology

Based on the results of the literature review and the summary papers [15],[55],[60], and [61] describing bidirectional charger topologies, the chosen topology for the on-board bidirectional charger is a two stage topology. Stage 1 is a full bridge AC/DC converter, and Stage 2 is the half bridge buck boost DC/DC converter shown in Figure 3-2. The role of Stage 1 is to regulate the DC link voltage at any desired power factor, and the role of the Stage 2 is to charge and discharge the battery at any active power level. This leads to a decoupling of the active and reactive power controls, with reactive requests being passed through to the AC/DC controller and active power requests being passed through to the DC/DC controller.

The full bridge AC/DC converter is the ideal choice for a low power on-board charger due to low component stress, high control flexibility, and a high conversion ratio. It also performs well in discharging operation compared with the half-bridge and dual-buck topologies.

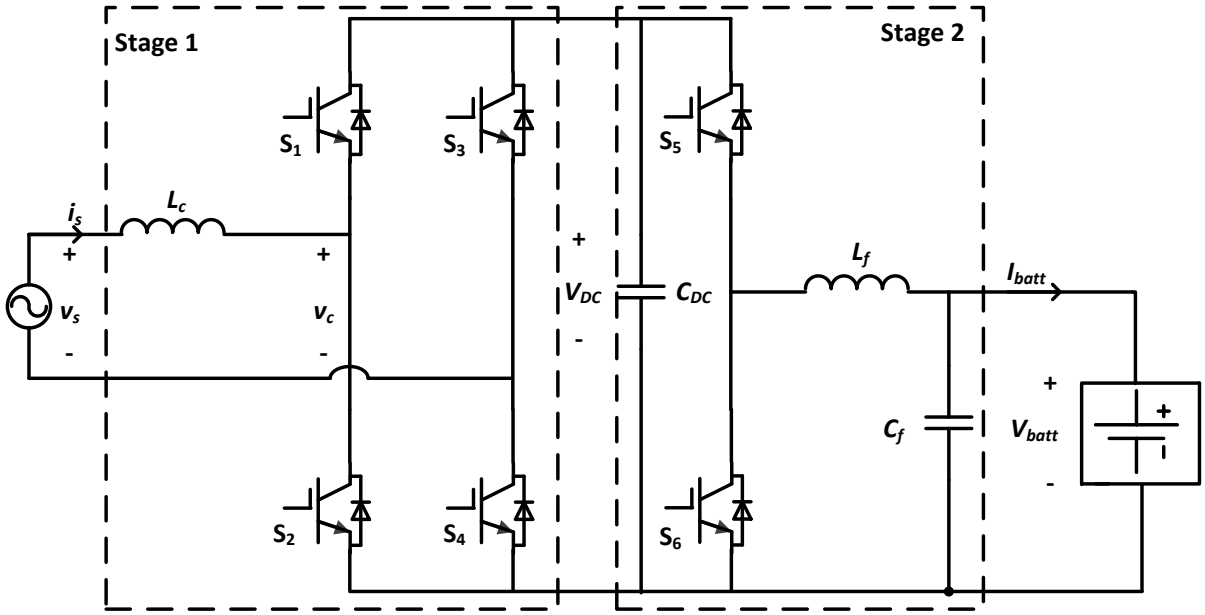

Figure 3-2. Single phase bidirectional battery charger topology.

3.1.2 Battery Model

The battery model presented in section 2.2.1 considers the short and long term transients that coincide with the degradation and SOC level of the battery, but determining these parameters accurately is a difficult task. Since, the controllers discussed in section 2.2.2 do not require V_{oc} as a control parameter, the benefit of using such a complex models is not worth the time investment. Hence, since it is always the case that, when current is flowing into the battery, $V_{batt} > V_{oc}$, and when current is flowing out of the battery, $V_{batt} < V_{oc}$, then the simplified battery model shown in Figure 3-3 is used in the analysis that follows.

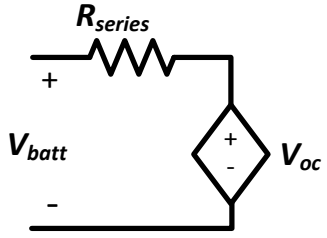

Figure 3-3. Simple lithium-ion battery pack electrical model.

3.2 Reactive Power Controllers

Two solutions for an AC/DC controller with zero steady-state error were presented in section 2.3. Here, these controllers are expanded upon to include reactive power control, and evaluated to determine which solution is best.

3.2.1 PR Control

The PR controller shown in Figure 2-10 synchronizes the current reference term to the grid voltage, so that the converter operates at unity power factor. However, reactive power control can only be achieved if the reference current term is not in phase with voltage. Hence, various control strategies have been presented for reactive power control using the phase angle θ as the feedback term such as the controller presented in Figure 3-4, where the phase angle is measured and compared to a reference angle calculated from the desired power factor and then fed into a PI regulator. The output is subtracted from the AC voltage phase angle to form the phase component of the reference current waveform. However, this controller has poor performance when tracking power factor, and the PI controller must be retuned at every power factor [44]. Furthermore, this solution does not decouple the active and reactive power requests. For example, if $P_{req} = 500$ W and $Q_{req} = 500$ VAR, then $\theta_{ref} = 45^o$; if P_{req} is changed by the utility such that $P_{req} = 1000$ W, then $\theta_{ref} = 63.4^o$. This would require an update to the reference phase angle even though Q_{req} is unchanged.

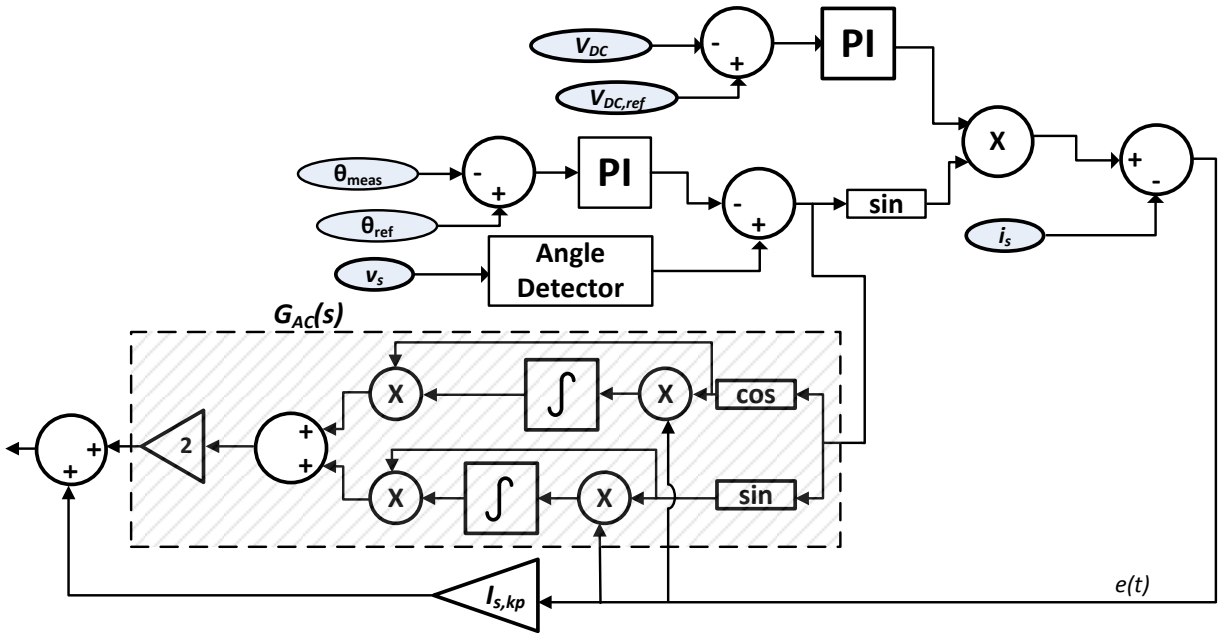

Figure 3-4. Block diagram of PR Controller with power factor control.

Based on the above, any controller using 'desired phase' as the reference term is not adequate. To fix this problem, assume for now that there is a way to accurately measure, Q_s then a devised strategy for decoupled control is presented in Figure 3-5; where Q_{meas} is subtracted from Q_{ref} and fed into a PI regulator to determine a delay factor τ for v_s. The voltage v_s is fed into a variable delay which delays the signal one full cycle plus a delay factor τ, which can be positive or negative depending on whether the power factor is leading or lagging. Since this is a causal system, a full cycle delay must be introduced for the event $\tau < 0$. This produces the phase component for the reference current waveform that is completely decoupled from the active power controller. The primary drawback of this approach is the full cycle phase delay, which will consume a lot of the controllers memory, and have a 16.67 ms delay with respect to deviations in v_s for a 60 Hz system.

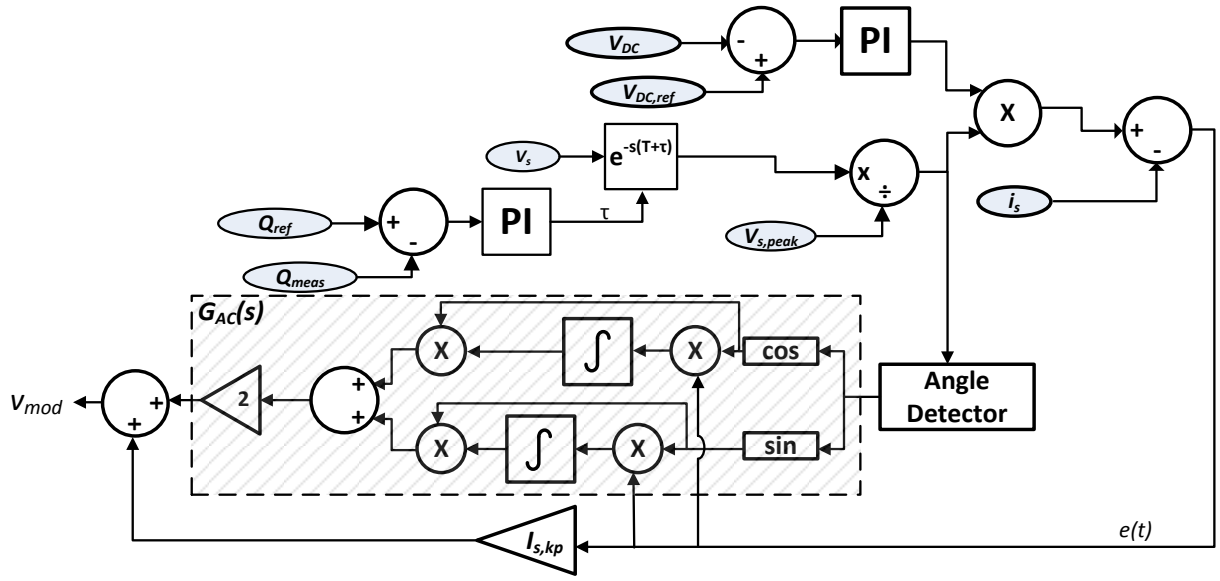

Figure 3-5. AC/DC PR Controller with reactive power support.

3.2.2 Dq Control

The dq controller shown in Figure 2-12 sets the quadrature current I_q reference to zero so that the converter operates at unity power factor, this way non-unity power factor can be achieved. If each vector in the dq frame is considered to have a real and imaginary component, where the d-axis is the real component and the q-axis the imaginary component, then the dq-frame voltage and current can be represented as:

$$\vec{V}_{dq} = V_d + jV_q \tag{3.1}$$

$$\vec{I}_{dq} = I_d + jI_q \tag{3.2}$$

One of the primary advantages of transforming into the dq frame is that active and reactive power can easily be calculated based on the complex power representation. Thus, from (3.1) and (3.2) it follows that:

$$S = \vec{V}_{dq} \cdot \vec{I}^*_{dq} = \frac{1}{2}(V_d + jV_q)(I_d - jI_q) \tag{3.3}$$

Substituting $V_q = 0$ in (3.3) results in a real and imaginary component as follows:

$$S = P_s + jQ_s = \frac{1}{2}V_d I_d - j\frac{1}{2}V_d I_q \tag{3.4}$$

The only controllable variable on the right hand side of the equation is I_q since V_d is determined by v_s and I_d is determined by the battery current and losses in the system. Therefore, by setting $I_{q.ref}$, reactive power can be controlled, decoupled from active power control.

Similar to the solution presented for the PR controller, the dq Q controller is presented in Figure 3-6, where Q_{ref} is subtracted from Q_{meas}, then divided by $-0.5V_d$, and then fed into a PI regulator to produce $I_{q,ref}$. This is an ideal solution since Q_s is easily calculated, and reactive power control is decoupled from active power control.

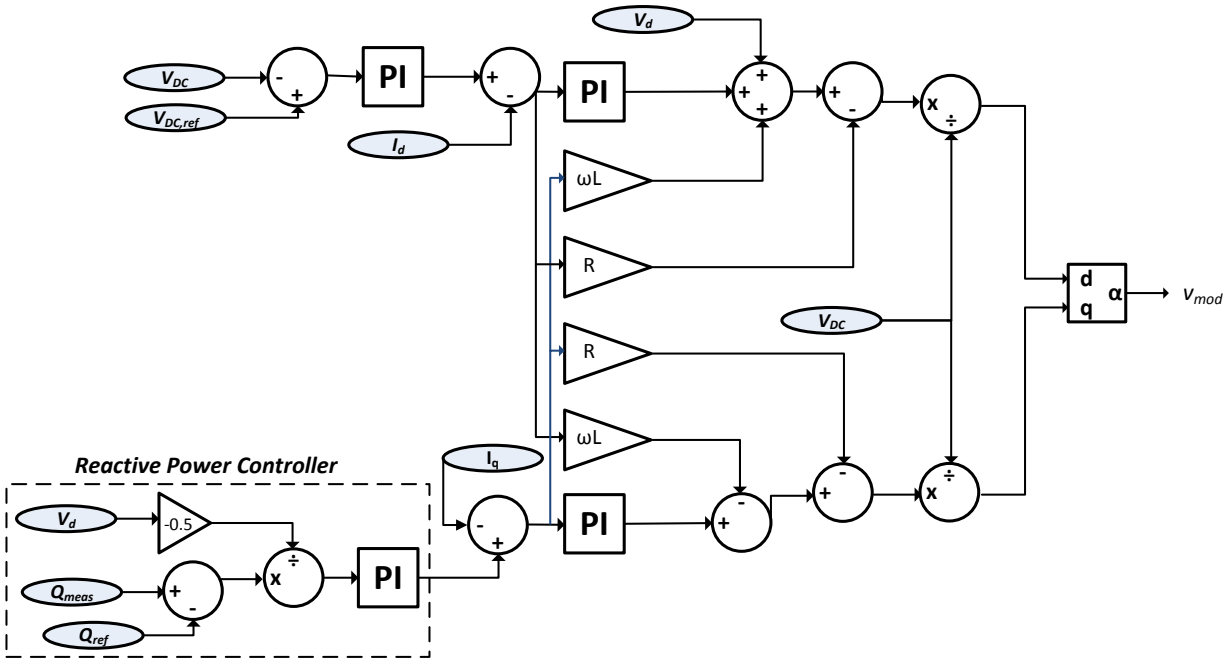

Figure 3-6. AC/DC DQ Controller with reactive power support.

Initially it was observed that the reactive power controller was unable to settle at a steady Q_s value. This in part, is because any ripple in V_d or I_q would carry forward into Q_{meas}, which would carry forward into I_q and then into Q_{meas}, and the cycle would thus continue. An easy solution would be to slow down the response of the PI regulator, but this reduces the speed of response of the controller and increases the chances of steady state error. An ideal solution is then to insert a low pass filter immediately after Q_s is calculated. Since Q_{ref} is not expected to change more than once a minute, a slow response will not hinder the overall performance of the charger; this low pass filter will give similar results to a moving

average filter, but at a lower cost. A discrete first order low pass state space filter was implemented as follows:

$$\begin{bmatrix} x[k+1] \\ y[k] \end{bmatrix} = \begin{bmatrix} A & B \\ C & D \end{bmatrix} \begin{bmatrix} x[k] \\ u[k] \end{bmatrix} \tag{3.5}$$

where A = 0.999 , B = 0.9995 , C = 0.00995 and D = 0.0049975. The filter, shown in Figure 3-7, will filter out the high frequency ripples that are present as a result of $V_d I_q$ before the reactive term Q_{meas} is utilized in the dq controller.

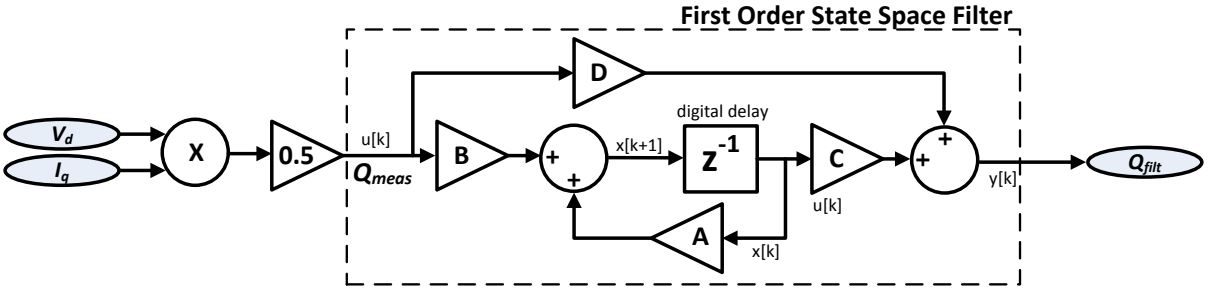

Figure 3-7. First order discrete state space filter.

Simulation results, showing the comparison between Q_{meas} and Q_{filt} are given in Figure 3-8. In this simulation, the reactive power controller was tested with $Q_{ref} = 1.92$ kVAR. One can observe that the measured component has a significant ripple component and with the filter zero steady state error is achieved.

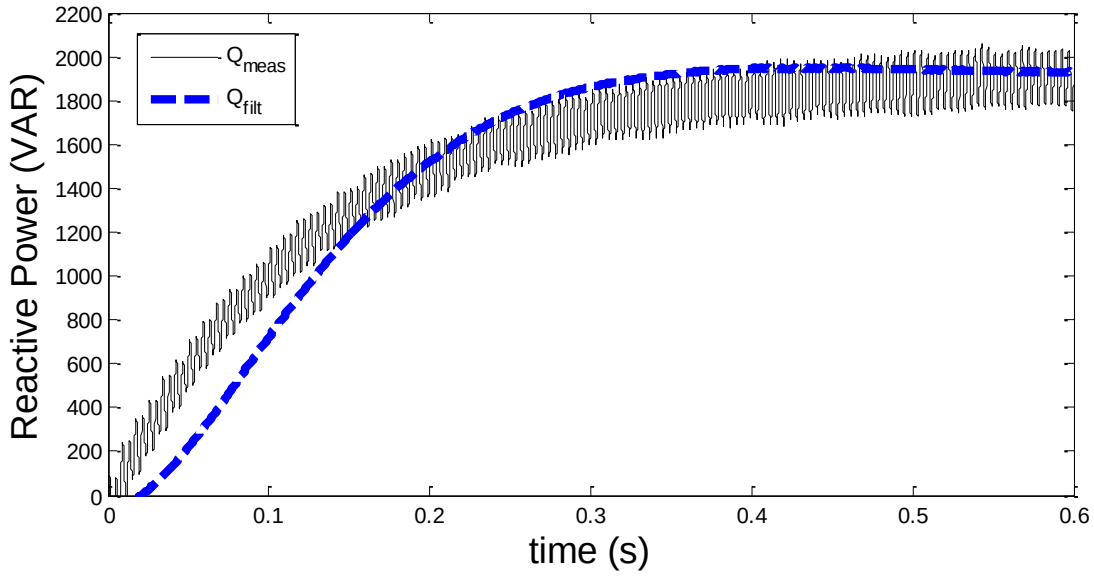

Figure 3-8. Simulation results of first order state space filter in reactive power controller.

3.2.3 Controller Comparison

Based on the analysis of PR and dq controllers for reactive power control, it is apparent that the dq controller is the ideal control strategy. Since, by design, the dq controller requires the computation of current and voltage in the dq reference frame, it inherently makes it easy to calculate reactive power. Furthermore, decoupled P-Q control with the PR controller requires that a full cycle of sample points for v_s be stored in the controller's memory. For example, a controller sampling data every 50 µs (20 kHz) would require 334 data points to store one 60 Hz cycle. If these data points were stored as 64-bit floating point numbers, then it would require 2.672 kB of the controllers RAM. The PR controller does not present a trivial method of calculating reactive power. It could either use the dq transform to determine Q_s as explained in Chapter 2, or it could use v_s, i_s and θ. However, this technique requires RMS computations, which can use a significant amount of the controller's memory. Therefore, based on the significant positive points for using a dq controller and the drawbacks of the PR controller, the dq controller will be used here as the AC/DC reactive power controller.

3.3 Active Power Controllers

3.3.1 Constant Power Charging

The active power flow from the grid is dictated by the battery current, battery voltage, and losses in the charger. As elaborated upon in the previous section, the dq-frame component $I_{d,ref}$ is determined by the output of the PI regulator from the $V_{DC,err}$ term (Figure 3-6). If the DC/DC stage of the converter is drawing current from the DC link capacitor to charge the battery, there will be a decrease in the DC link voltage. This will then be fed back into the dq-controller as a higher $I_{d,ref}$, which will result, initially, in a higher $I_{d,err}$, resulting in more current being pulled from the grid to increase the DC link voltage. If properly tuned, the dq controller will be able to automatically respond to changes in the DC link voltage by either pulling power from the grid if the DC link voltage drops, or pushing power to the grid if the DC link voltage increases. Therefore, it can be concluded that by controlling the charging and discharging of the battery with the DC/DC component of the charger, active power control can be achieved, decoupled from the reactive power controller in the AC/DC component of the charger.

As was shown in Figure 2-5, DC/DC control is very straightforward, thus an error term is generated and fed into a PI regulator and the output is the modulation voltage for the PWM controller. Since this controller is operating on DC quantities, zero steady-state error and fast response can be achieved, even with a simple control method.

It is critical that the Smart Charger be capable of charging/discharging at a constant active power level, so that it may accommodate requests from the utility. There are two significant reasons why the CC-CV charging algorithm will not satisfy this requirement. First, the CC-CV algorithm does not have constant power (see Figure 3-9), since during the CC phase voltage is increasing and during the CV phase current is decreasing. The second reason is that this algorithm is based on measurements taken at the battery terminals and not at the grid interface, thus not accounting for converter losses. For example, if the battery is being charged at 1.5 kW and the converter has 0.2 kW of losses, then the active power seen at the grid interface is 1.7 kW. One solution is to calculate charging power based on battery parameters, then add the estimated losses of the system to determine power at the PCC. This is not a good solution since losses are not consistent at all power levels. A better approach is to calculate power at the grid interface and then use that parameter to dictate the charging current, as shown in Figure 3-10, where P_{meas} is the calculated power from (3.4), which is the active power at the PCC, and P_{ref} is the active power request

sent from the utility; the error is processed by a PI regulator to determine $I_{batt,ref}$. This is a two loop control method where the outer loop has a slower response than the inner loop. Note that this active power controller is decoupled from the reactive power controller, and fully accounts for the losses in the system.

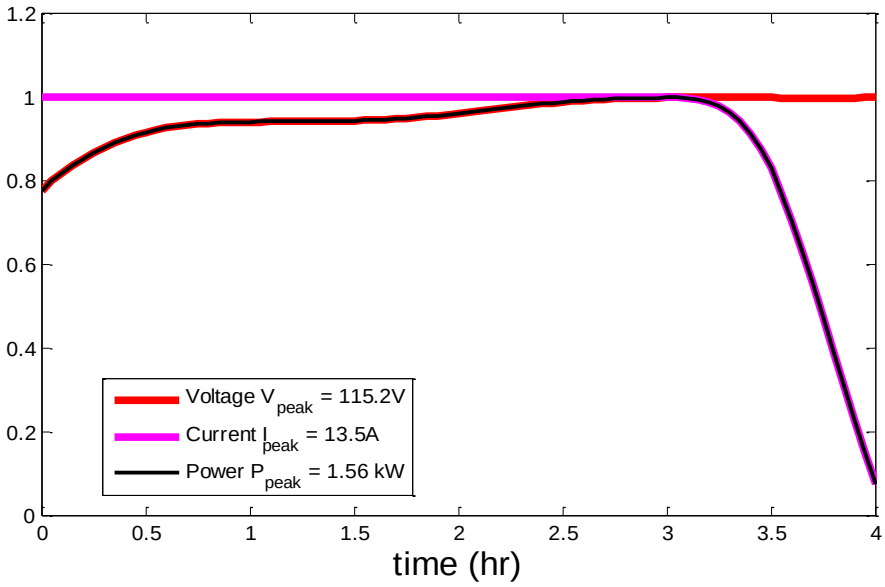

Figure 3-9. CC-CV charging profile normalized.

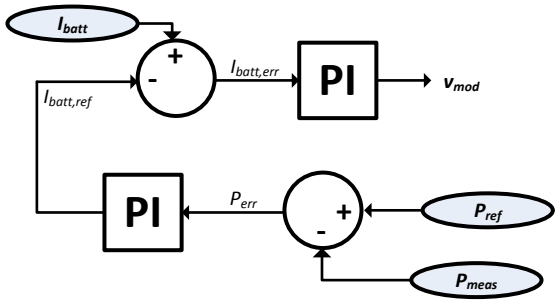

Figure 3-10. Block diagram for constant power charging algorithm.

3.4 Optimal Sizing of Components

The battery charger is composed of two major components, the AC/DC converter and the DC/DC converter. The AC/DC converter requires 4 switches, 1 capacitor and 1 inductor, the DC/DC converter requires 2 switches, 1 capacitor and 1 inductor. In the AC/DC converter, component selection mainly affects the DC link voltage ripple, grid current harmonics, and reactive power limits. In the DC/DC converter, the components are used as an LC filter to reduce the battery current and voltage ripple.

For consistency the analysis that follows will be based on the specifications of the prototype bidirectional charger presented in Chapter 5. The prototype is designed to be a Level 1 charger, capable of charging at rates up to 1.92 kVA (16 A) with a 105 VDC battery pack.

3.4.1 DC/DC Converter Parameters

A bidirectional buck-boost DC/DC converter is shown in Figure 3-11, with the duty cycle by:

$$d = \frac{V_{batt}}{V_{DC}} \tag{3.6}$$

During charging, the battery terminal voltage increases and during discharging the battery terminal voltage decreases due to the series resistance of the battery as explained in section 2.2.1.

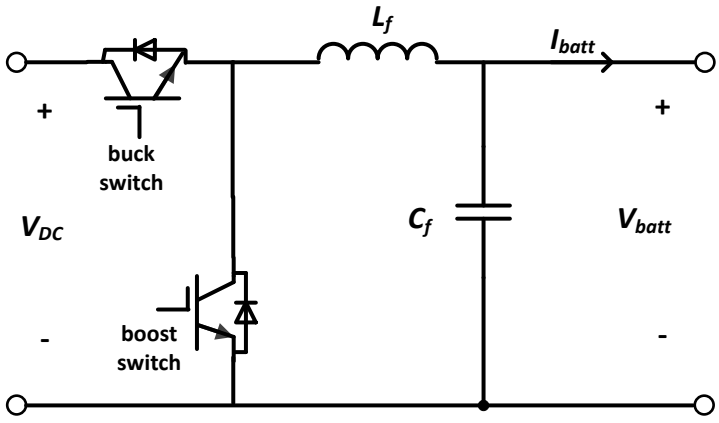

Figure 3-11. Bidirectional buck-boost DC/DC converter.

The open circuit duty cycle d_o is defined as the no-charge, no-discharge duty cycle as follows:

$$d_o \equiv \frac{V_{oc}}{V_{DC}} \tag{3.7}$$

If the DC/DC converter were to operate at $d = d_o$, no current would flow in or out of the battery. If $d < d_o$ then $V_{batt} < V_{oc}$ and the battery is discharging current. If $d > d_o$ then $V_{batt} > V_{oc}$ and the battery is being charged. During continuous operation, the magnitude of the peak-to-peak current ripple is given by:

$$I_{batt,rip} = \frac{dV_{batt}T_s}{L_f} \tag{3.8}$$

Substituting (3.6) into (3.8) and rearranging the equation yields the following relationship between battery current ripple, duty cycle, DC link voltage and inductance:

$$L_f = \frac{d_o^2 V_{DC} T_s}{I_{batt,rip}} = \frac{V_{batt}^2 T_s}{V_{DC} I_{batt,rip}} \tag{3.9}$$

By analyzing this equation it can be seen that for a fixed L_f and V_{batt}, by increasing V_{dc}, $I_{batt,rip}$ decreases. One goal in a DC/DC converter is to make $I_{batt,rip}$ as small as possible, which can be achieved by increasing L_f or V_{dc}. Increasing V_{dc} requires a larger capacitor, and increasing L_f requires a larger inductor. Generally speaking, the inductors add the most weight and cost to the charger, so it is preferable to increase V_{dc} over L_f in order to achieve the desired $I_{batt,rip}$.

For a switching frequency of 20 kHz ($T_s = 50$ µs) and $I_{batt,rip} = 1.5$ A, L_f can be found from (3.9) to be $L_{f,min} = 1.225$ mH.

The focus of this thesis is not on modeling the li-ion batteries, and without a complete model of the battery it is difficult to derive an equation relating the voltage ripple $V_{batt,rip}$ of the battery to the battery pack input capacitor C_f. It is widely known however, that $V_{batt,rip}$ is inversely proportional to C_f. This implies a tradeoff between increasing the weight of the charger and decreasing the voltage ripple. Therefore, based on recommendations from the battery supplier, Elite Power Solutions, it was decided that $C_f = 1.0$ mF.

3.4.2 DC Link Ripple

The values of DC link capacitor C_{DC}, DC link voltage V_{DC}, and coupling inductor L_c are tightly coupled. Changing one of these variables has a ripple effect on the others, so the relationship among all these terms

must first be established. These relationships have been derived in [55] and [16], where they show that the key equation linking these parameters is the energy stored in the ripple of the DC link capacitor.

Referring to Figure 3-2, the instantaneous grid voltage $v_s(t)$, grid current $i_s(t)$, and inductor voltage $v_L(t)$ are:

$$v_s(t) = \sqrt{2}V_s \sin(\omega t) \tag{3.10}$$

$$i_s(t) = \sqrt{2}I_s \sin(\omega t - \theta) \tag{3.11}$$

$$v_L(t) = L_c \frac{di_s(t)}{dt} = \sqrt{2}\omega L_c I_s \cos(\omega t - \theta) \tag{3.12}$$

where θ is the phase angle between $v_s(t)$ and $i_s(t)$. The charger input voltage $v_c(t)$ can then be written as:

$$v_c(t) = v_s(t) - v_L(t) = \sqrt{2}V_s \sin(\omega t) - \sqrt{2}\omega L_c I_s \cos(\omega t - \theta) \tag{3.13}$$

It then follows that the charger input power can be written as:

$$\begin{aligned} p_c(t) &= \tfrac{1}{2} v_c(t) i_s(t) \\ &= \tfrac{1}{2}\{\sqrt{2}V_s \sin(\omega t) - \sqrt{2}\omega L_c I_s \cos(\omega t - \theta)\}\{\sqrt{2}V_s \sin(\omega t - \theta)\} \\ &= V_s I_s cos\theta - V_s I_s \cos(2\omega t - \theta) - \omega L_c I_s^2 \sin(2\omega t - 2\theta) \end{aligned} \tag{3.14}$$

This input power can then be broken into its DC component and ripple components, where the ripple component is oscillating at twice the grid frequency, as follow:

$$p_{ripple}(t) = -V_s I_s \cos(2\omega t - \theta) - \omega L_c I_s^2 \sin(2\omega t - 2\theta) \tag{3.15}$$

This equation can be re-arranged such that the ripple component is composed of two terms, oscillating at the same frequency, 90^{O} apart, much like a phasor, so that it is easy to determine the magnitude and angle; thus:

$$\begin{aligned} p_{ripple}(t) &= -V_s I_s \cos(2\omega t - \theta) - \omega L_c I_s^2 \sin(2\omega t - \theta)\, cos\theta - \omega L_c I_s^2 \cos(2\omega t - \theta)\, sin\theta \\ &= -\cos(2\omega t - \theta)\,(V_s I_s + \omega L_c I_s^2 sin\theta) - \sin(2\omega t - \theta)\,(\omega L_c I_s^2 cos\theta) \end{aligned} \tag{3.16}$$

The magnitude of $p_{ripple}(t)$ is the parameter of interest and is calculated as:

$$\left|p_{ripple}(t)\right| = \sqrt{(V_s I_s + \omega L_c I_s^2 sin\theta)^2 + (\omega L_c I_s^2 cos\theta)^2} \tag{3.17}$$

Substituting $S = V_s I_s$ and $Q_s = V_s I_s sin\theta$ in (3.17), and rearranging yields the magnitude of the power component of the ripple:

$$P_{ripple} = \sqrt{S^2 - 2\omega L_c \frac{S^2}{V_s^2} Q_s + \left(\omega L_c \frac{S^2}{V_s^2}\right)^2} \tag{3.18}$$

The energy of the ripple will be oscillating in and out of the DC link capacitor over the course of one full cycle, so the total energy of the ripple moving in and out of the DC link capacitor will be the integral of $p_{ripple}(t)$ over the half cycle in which $P_{ripple}(t)$ is flowing into the capacitor. From (3.16) it can be seen that the ripple will oscillate at twice the grid frequency, and since half a cycle will measure $\pi/2\omega$, the energy corresponding to the ripple can be calculated as follows:

$$\begin{aligned} E_{ripple} &= \int_{-\frac{\pi}{4\omega}+\gamma}^{\frac{\pi}{4\omega}+\gamma} P_{ripple} \cos(2\omega t - \gamma)\, dt \\ E_{ripple} &= \frac{1}{\omega}\sqrt{S^2 - 2\omega L_c \frac{S^2}{V_s^2} Q_s + \left(\omega L_c \frac{S^2}{V_s^2}\right)^2} \end{aligned} \tag{3.19}$$

where γ is the power ripple phase delay. It is important to reiterate here that $Q_s > 0$ refers to reactive power flow into the battery charger (i.e., inductive operation) and $Q_s < 0$ refers to reactive power support (i.e., capacitive operation). From (3.19), it can be seen that as reactive power support increases, E_{ripple} increases. Since E_{ripple} manifests itself in the DC link voltage ripple and capacitor current ripple, a larger capacitor will be required for reactive power support, than would otherwise be required for a unidirectional charger.

3.4.3 Minimum DC Link Voltage

In order for the converter to operate in the linear modulation range to satisfy the sinusoidal current assumption, the peak voltage on the AC side must be less than the minimum voltage on the DC side. In other words, the following must be satisfied:

$$V_{DC} \geq \sqrt{2}V_c \tag{3.20}$$

where V_c is the rms value of the fundamental component of the voltage on the AC-side of the converter. Rearranging (3.13) so that there are two sinusoidal terms oscillating at the same frequency, 90^{O} apart, yields:

$$v_c(t) = \sqrt{2}(V_s - \omega L_c I_s \sin\theta)\sin(\omega t) - \sqrt{2}(\omega L_c I_s \cos\theta)\cos(\omega t) \tag{3.21}$$

Taking the magnitude of this expression and substituting $S = V_s I_s$ and $Q_s = V_s I_s sin\theta$ results in:

$$|v_c(t)| = V_c = \sqrt{V_s^2 - 2\omega L_c Q_s + \left(\omega L_c \frac{S}{V_s}\right)^2} \tag{3.22}$$

and substituting this into (3.20) yields:

$$V_{DC} \geq \sqrt{2\left(V_s^2 - 2\omega L_c Q_s + \left(\omega L_c \frac{S}{V_s}\right)^2\right)} \tag{3.23}$$

Based on these findings, the effect the coupling inductor size has on the minimum DC link voltage for various levels of Q_s is displayed in Figure 3-12, where $V_s = 120\,\text{V}$ and $S = 1.92\,\text{kVA}$. Observe that the minimum required DC link voltage is greatest when the charger is providing 100% reactive power support to the grid, and that for larger values of L_c, the required minimum DC link voltage increases even further. Based on this a L_c value in the range $1 - 2\,\text{mH}$ is ideal since an inductor of this size is large enough to filter current harmonics and smooth the current waveform, but is not so large that the physical size of the inductor will be too large and heavy for the on-board bidirectional charger.

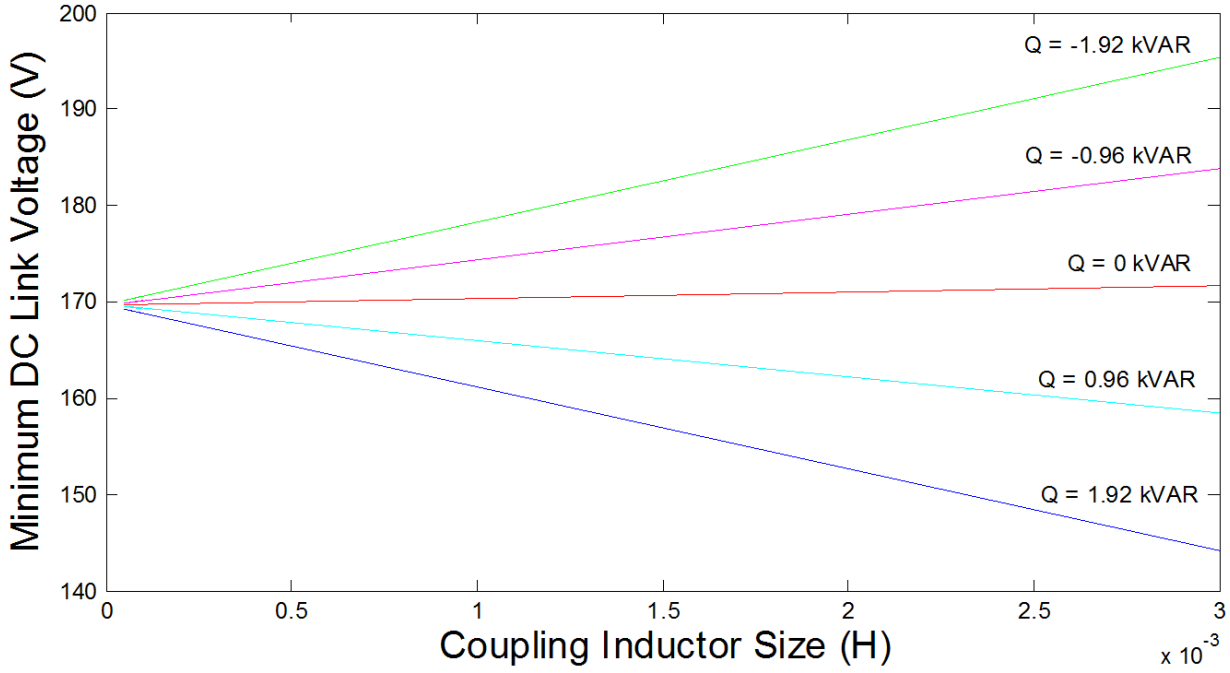

Figure 3-12. Minimum allowable DC link voltage vs. coupling inductor size.

3.4.4 DC Link Capacitor Size

It is assumed that the switches in the converter are lossless; therefore, the ripple energy available at the input of the converter is the same energy available at the DC link capacitor, which manifests itself in the form of DC link voltage ripple. The maximum ripple energy that may be stored in the capacitor is described by:

$$E_{cap,ripple} = \frac{1}{2} C_{DC}\left(V_{DC,peak}^2 - V_{DC,min}^2\right) = C_{DC} V_{DC} V_{DC,rip} \tag{3.24}$$

where $V_{DC,peak} - V_{DC,min} = V_{DC,rip}$ and $V_{DC} = \frac{1}{2}(V_{DC,peak} + V_{DC,min})$. By substituting for $E_{cap,ripple}$ from (3.19) and solving for C_{DC}, the size of the DC link capacitor can be described in terms of V_{DC} and $V_{DC,rip}$, as follows:

$$C_{DC} = \frac{\sqrt{S^2 - 2\omega L_c \frac{S^2}{V_s^2} Q_s + \left(\omega L_c \frac{S^2}{V_s^2}\right)^2}}{\omega V_{DC} V_{DC,rip}} \tag{3.25}$$

From this equation, it can be observed that if Q_s injected to the grid increases, all else remaining equal, C_{DC} will increase as well. The same can also be said for the minimum DC link voltage; if Q_s injected to the grid increases, V_{DC}will increase if all else remains equal. It follows then that, since the aim of this thesis is to develop a fully functional bidirectional charger, capable of providing full reactive power support C_{DC} should be sized for $Q_s = -S$.

Figure 3-13 shows the relationship described in (3.25), where $L_c = 1.5$ mH, $S = 1.92$ kVA, $Q_s = -1.92$ kVAR, $\omega = 120\pi$ and $V_s = 120$ V. It can be observed that as the maximum allowable ripple increases, the size of the DC link capacitor decreases. Furthermore, as the DC link voltage increases, the size of the DC link capacitor decreases as well. A large ripple on the DC bus can cascade into a large current at the terminals of the battery; therefore, careful consideration must be taken when sizing the DC link capacitor. If, for example, it is decided that $V_{DC,rip} < 20V_{pp}$, then the DC link capacitance and DC link voltage must be selected such that the intersection of the two lie above the $V_{DC,rip} = 20$ V curve.

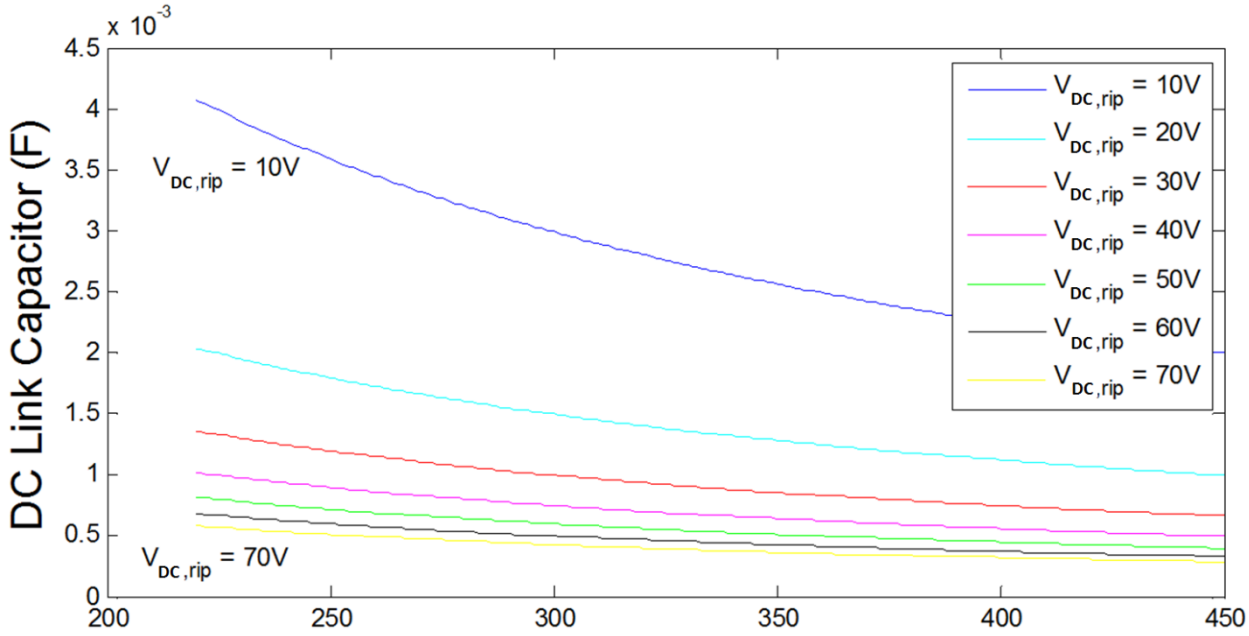

Figure 3-13. DC link capacitor size vs. DC link voltage.

3.4.5 DC Link Capacitor Current Ripple

As established in (3.16), there will be an oscillating power on the DC link capacitor at twice the grid frequency. It then follows that the instantaneous DC link voltage can be expressed as:

$$v_{DC}(t) = V_{DC} + \frac{V_{DC,rip}}{2}\cos(2\omega t - \gamma) \tag{3.26}$$

Only the oscillating current will flow through the capacitor; thus:

$$i_{cap,rip}(t) = C_{DC}\frac{dv_{DC}(t)}{dt} = -\omega C_{DC} V_{DC,rip}\sin(2\omega t - \gamma) \tag{3.27}$$

The RMS value is, therefore:

$$\begin{aligned} I_{cap} &= \frac{1}{\sqrt{2}}\omega C_{DC} V_{DC,rip} \\ I_{cap} &= \frac{\sqrt{S^2 - 2\omega L_c \frac{S^2}{V_s^2} Q_s + \left(\omega L_c \frac{S^2}{V_s^2}\right)^2}}{\sqrt{2} V_{DC}} \end{aligned} \tag{3.28}$$

This relationship is plotted in Figure 3-14, where it can be seen that as capacitance increases, if all else remains equals, capacitor current ripple increases. In contrast to all other parameters, this is the first negative effect observed from increasing the DC link capacitance. However, from (3.28) it can be seen that the capacitor current is inversely proportional to the DC link voltage, suggesting that the capacitor current can be minimized by maximizing DC link voltage, minimizing ripple, and minimizing DC link capacitance.

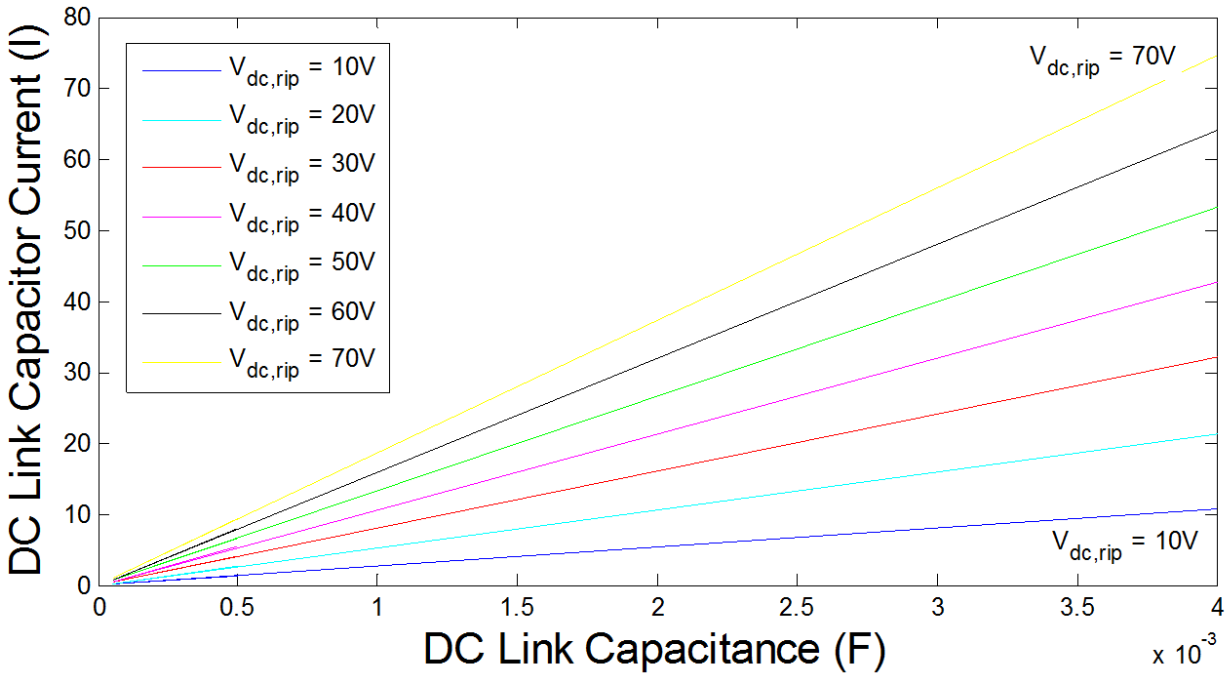

Figure 3-14. DC link capacitance vs. DC link capacitor current ripple.

3.4.6 Final Component Values

The final selection for the system parameters and a summary of the results obtained in this section is given in Table 3-1. The first five parameters are simply the parameters of a Level 1 EV charger. The battery voltage and current are based on the lithium ion battery pack used for the prototype design and will be discussed further in Chapter 5. The values of V_{DC}, L_c, C_{DC}, L_f, and C_f are all coupled and based on the analysis in the preceding sections and chosen to minimize DC link voltage ripple, current ripple, cost, and weight. The new parameter introduced in Table 3-1, switching frequency, is chosen to be 20 kHz. This switching frequency was selected so that it would be out of the audible range for humans, but not so high that it would produce large high frequency voltage and current ripples and high switching losses in the converter.

Table 3-1. System Parameters

Description	System Parameter	Value	Unit
Smart Charger VA Rating	S	1.92	kVA
Absolute Maximum Reactive Power	Q_s	1.92	kVAR
Absolute Maximum Active Power	P_s	1.92	kW
Grid Voltage	V_s	120	VAC
Maximum AC Current	I_s	16	AC
Absolute Maximum Battery Current	I_{batt}	20	AC
Nominal Open Circuit Battery Voltage	V_{oc}	105	VDC
DC Link Voltage	V_{DC}	280	VDC
Coupling Inductor	L_c	1.65	mH
DC Link Capacitor	C_{DC}	2	mF
DC/DC Filter Inductor	L_f	1.5	mH
DC/DC Filter Capacitor	C_f	1.0	mF
Switching Frequency	f_s	20	kHz

3.5 Summary

Based on the analysis done in Chapter 2 and the review in Chapter 1, the Smart Charger topology and battery model were finalized. A constant active power controller, and two candidate reactive power controllers based on the PR and dq controllers shown in Chapter 2 were presented; ultimately settling on a hybridization of the dq controller over the PR controller. The chapter concluded by determining the optimal size of the high voltage components, DC link voltage, and battery voltage. The design work done in this chapter laid the foundation for the simulations and experimental implementation in subsequent chapters.

Chapter 4
Level 1 Bidirectional Charger Simulation Results

In this chapter a simulation model developed in Simulink for the purpose of validating the control strategy, steady state response and step response of the Smart Charger is presented. The simulation uses the system parameters summarized in Table 3-1, the dq controller as outlined in section 3.2.2, the active power controller as outlined in section 3.3.1, and the battery model shown in section 3.1.2.

4.1 Simulation Setup

In an attempt to account for as many of the non-idealities of the components as possible, all capacitors include an Equivalent Series Resistance (ESR) and Equivalent Series Inductance (ESL), and all inductors include an ESR. The bidirectional charger is simulated with a 1 μs discrete time step, fifty times shorter than the PWM switching period. The simulation model shown in Figure 4-1 shows the non-ideal components, and depicts the reference directions of P_s, Q_s, i_s and I_{batt}.

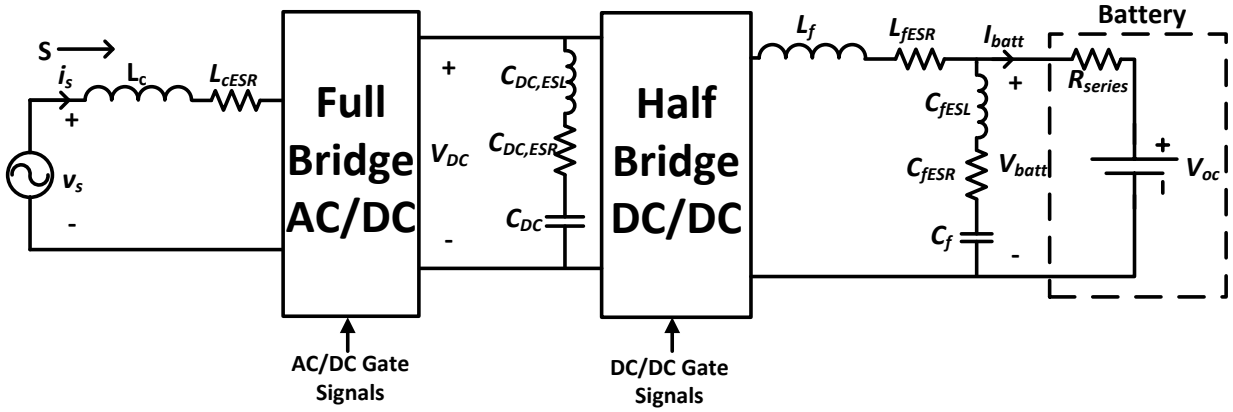

Figure 4-1. Smart charger simulation model.

The control strategy to calculate the AC/DC converter gate control signals is shown in Figure 4-2. The grid voltage v_s is first used to determine the phase angle θ with the PLL (see Figure 2-11) which outputs V_d and θ. The latter is then used to calculate the dq components of I_s through the αβ-dq transform, based on equation (2.6). The variables $V_d, I_d, I_q, \theta, V_{DC}$, and Q_s are then fed into the dq controller (see Figure 3-6) to create a modulating signal which is then passed into a unipolar PWM controller that creates four independent gate signals for the full bridge AC/DC converter.

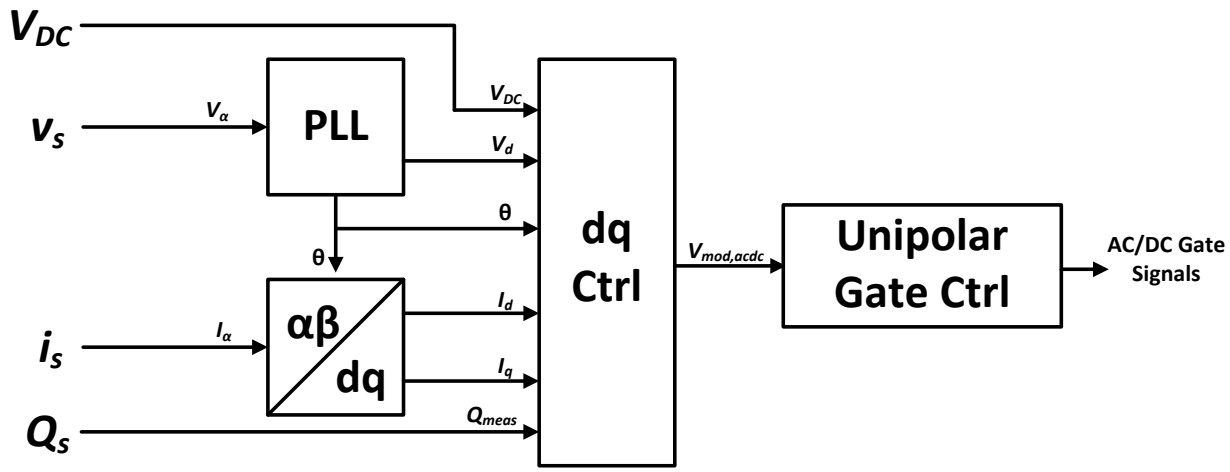

Figure 4-2. AC/DC controller.

V_{batt}, I_{batt}, and P_s are the inputs of the DC/DC Controller as well as a mode select to specify whether the controller be operated as a standard unidirectional, unity power factor charger or a smart bidirectional charger. If the charger is to be controlled like a standard charger with the constant current

constant voltage charging algorithm, then the strategy follows that of Figure 2-5. If the smart charging mode is to be used, then the strategy follows that of Figure 3-10, which provides a constant power charging strategy. The modulating signal is then fed into a PWM gate controller, which creates two control signals for the half bridge DC/DC converter. The final integral k_i and proportional k_p gains for the PI regulators found in Figure 3-6 and Figure 3-10 are listed in Table 4-1

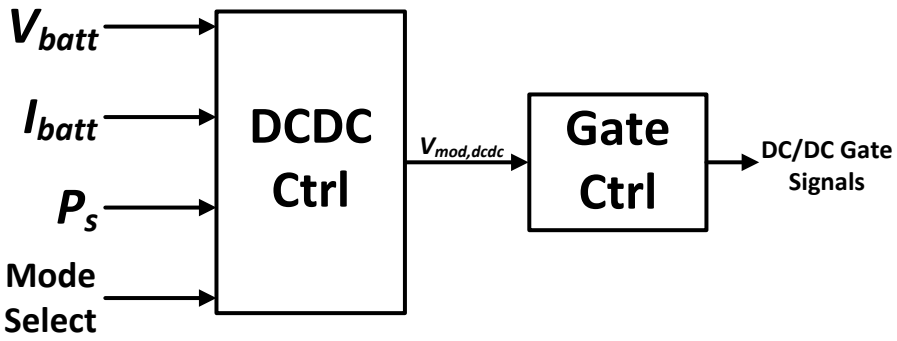

Figure 4-3. DC/DC controller.

Table 4-1. Simulation k_i and k_p values.

PI Regulator	k_i	k_p
$V_{DC,dq}$	3.7	0.37
$I_{d,dq}$	200	50
$I_{q,dq}$	80	40
$I_{batt,dcdc}$	1	0.001
$V_{batt,dcdc}$	1	0.001
Q_{dq}	15	0.07
P_{dcdc}	0.08	0.001

Sections 4.2 and 4.3 show the steady-state and step responses of the bidirectional Smart Charger operating in each of the four quadrants of the P-Q plane as well as on the borders between the neighboring quadrants. Therefore, eight simulations will be required where P_s and Q_s vary but S will remain constant at 1.92 kVAR. A summary of the P_s and Q_s values for each simulation is given in Table 4-2, and shown visually in Figure 4-4.

Table 4-2. Bidirectional charger simulation parameters summary.

Simulation	P_s (kW)	Q_s (kVAR)	Steady-State Response Figure
1	1.92	0	Figure 4-5
2	1.36	1.36	Figure 4-6
3	0	1.92	Figure 4-7
4	-1.36	1.36	Figure 4-8
5	-1.92	0	Figure 4-9
6	-1.36	-1.36	Figure 4-10
7	0	-1.92	Figure 4-11
8	1.36	-1.36	Figure 4-12

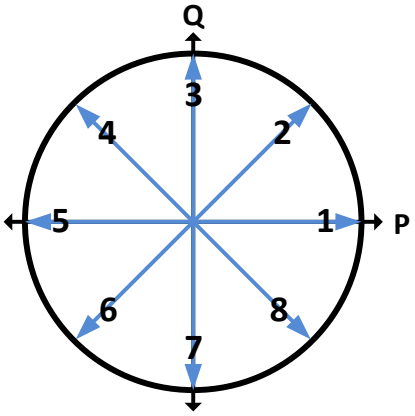

Figure 4-4. Smart charger simulation modes corresponding to Table 4-2.

4.2 Steady-State Response

The steady-state response of the bidirectional charger investigates three parameters, i.e., V_s, I_s and V_{DC}. For the simulations, it is assumed that the utility voltage v_s is constant in magnitude and operating at 60 Hz with no harmonics, since the power transactions of a single Smart Charger with the utility is not enough to cause a change in the grid voltage. The steady-state response is displayed over a 50 ms steady-state window. The parameters are displayed in per unit (pu) with the base values for each parameter being listed in Table 4-3.

Table 4-3. Steady state response base values.

Parameter	1 pu
v_s	175 V
i_s	30 A
V_{dc}	280 V

In Simulation 1 the charger operates at unity power factor delivering full rated power to the battery charger. This is only possible when the battery SOC is low enough to support full rated charging. Here, the DC link, 120 Hz voltage peak-to-peak ripple is $V_{DC,rip} = 9.124\,V$, and the total harmonic distortion of the ac-side current is $THD = 4.2\%$.

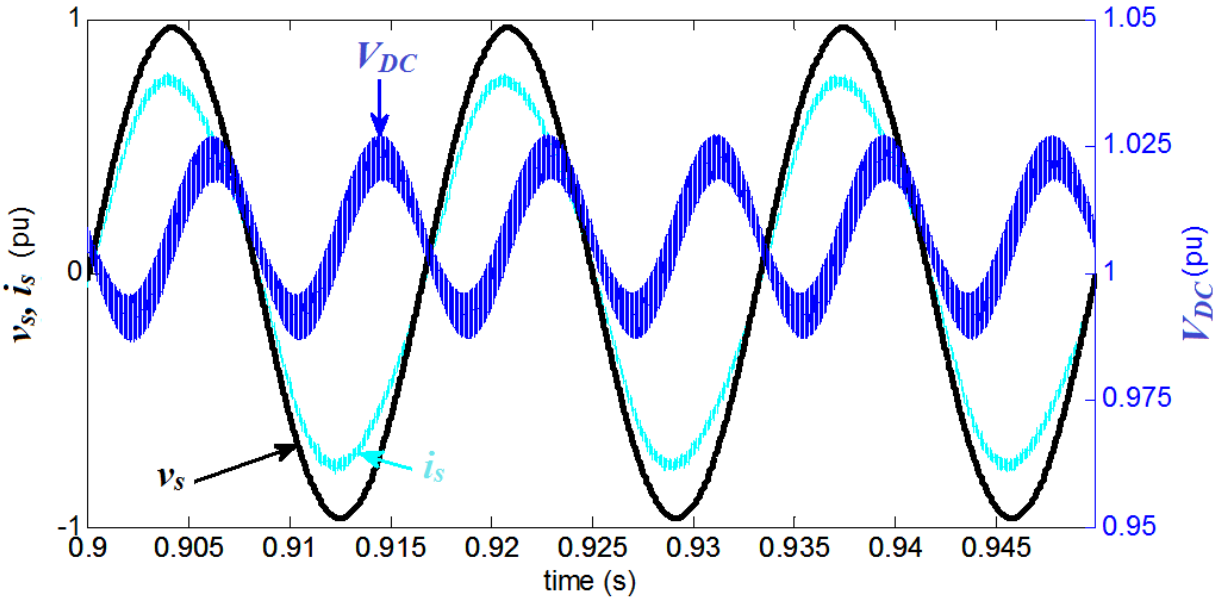

Figure 4-5. Steady-state response for Simulation 1, $P_s = 1.92$ kW and $Q_s = 0$ kVAR

In Simulation 2, the Smart Charger charges the vehicle battery at 1.36 kW and absorbs 1.36 kVAR from the grid, behaving as an R-L load with a 0.7083 lagging power factor. In this case, $V_{DC,rip} = 8.62$ V and ac-side current $THD = 4.2\%$. Since the charger is now absorbing reactive power, the voltage ripple decreases slightly as shown in (3.25) and the THD remains unchanged.

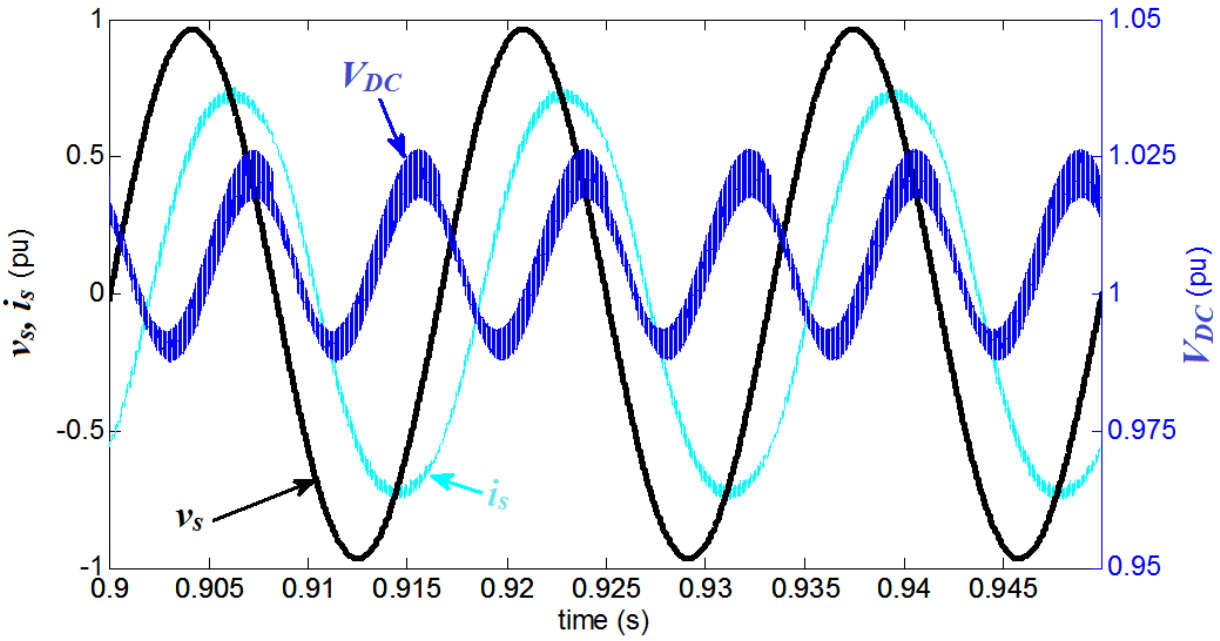

Figure 4-6. Steady-state response for Simulation 2, $P_s = 1.36$ kW and $Q_s = 1.36$ kVAR.

In Simulation 3, the smart charger is behaves as a purely inductive load absorbing 1.92 kVAR from the grid. The DC link voltage ripple decreases further to 8.414 V, and the THD drops to 4%.

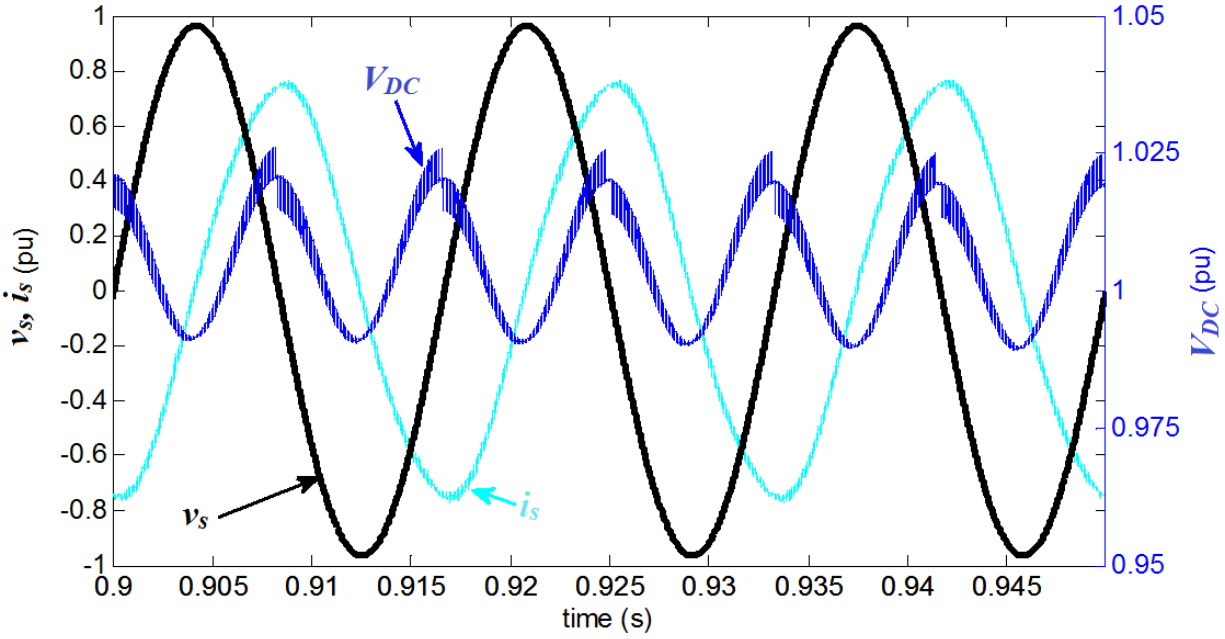

Figure 4-7. Steady-state response for simulation 3, $P_s = 0$ kW and $Q_s = 1.92$ kVAR.

In Simulation 4, the battery is now discharged to support the grid, supplying 1.36 kW while absorbing 1.36 kVAR. As expected, $V_{DC,rip}$ increases to 8.62 V, while the THD remains relatively unchanged at 4.1%.

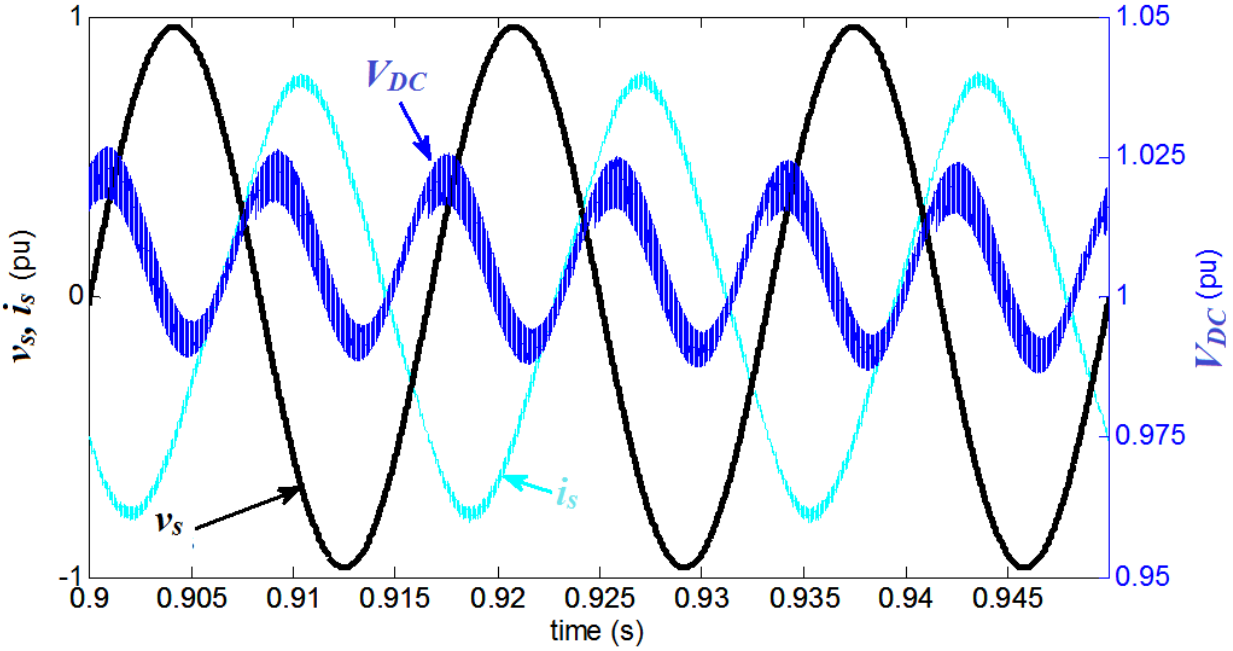

Figure 4-8. Steady-state response for Simulation 4, $P_s = -1.36$ kW and $Q_s = 1.36$ kVAR.

Simulation 5 presents a likely scenario wherein the smart charger provides purely full rated active power to the grid. Since the charger no longer absorbs reactive power, $V_{DC,rip}$ increases to 9.124 V and the THD increases as well to 4.3%. Since P_s and Q_s are measured at the grid interface, the battery will be responsible to account for the losses of the converter, so that $P_s = -1.92$ kW at the PCC. These losses are difficult to accurately measure in simulations, but must be a consideration when selecting battery pack for prototype implementation.

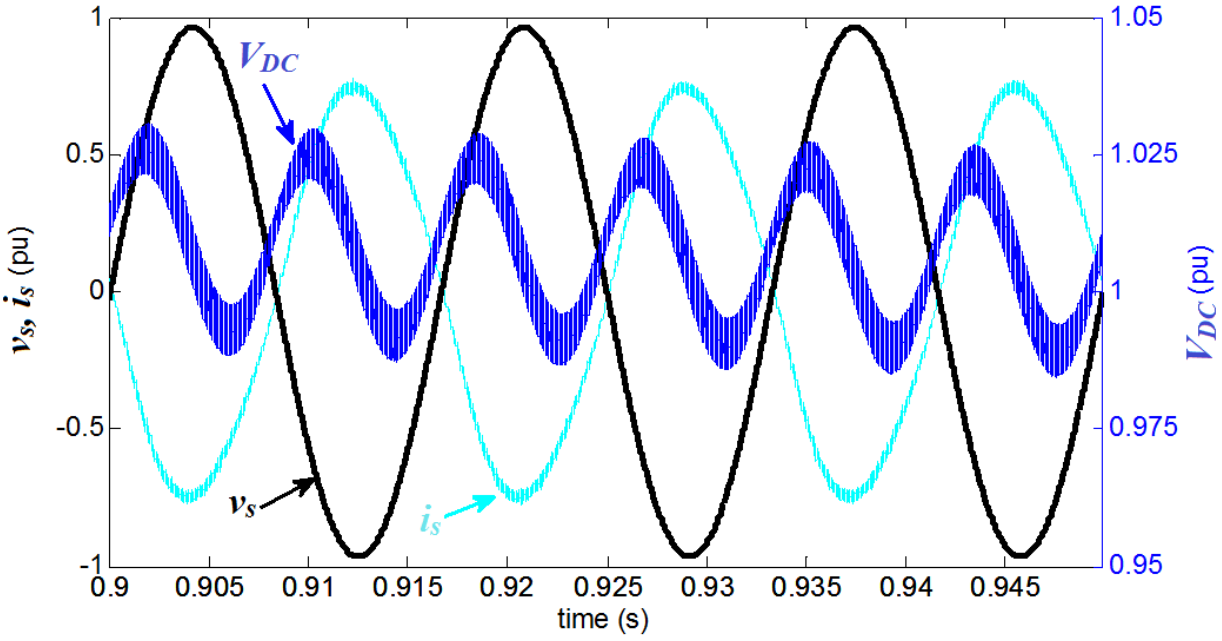

Figure 4-9. Steady-state response for Simulation 5, $P_s = -1.92$ kW and $Q_s = 0$ kVAR.

Simulation 6 has the Smart Charger providing 1.36 kW of active power and 1.36 kVAR of reactive power to the grid. Since the charger provides reactive power to the grid, $V_{DC,rip}$ increases to 9.60 V, and the THD increases a little further to 4.5%.

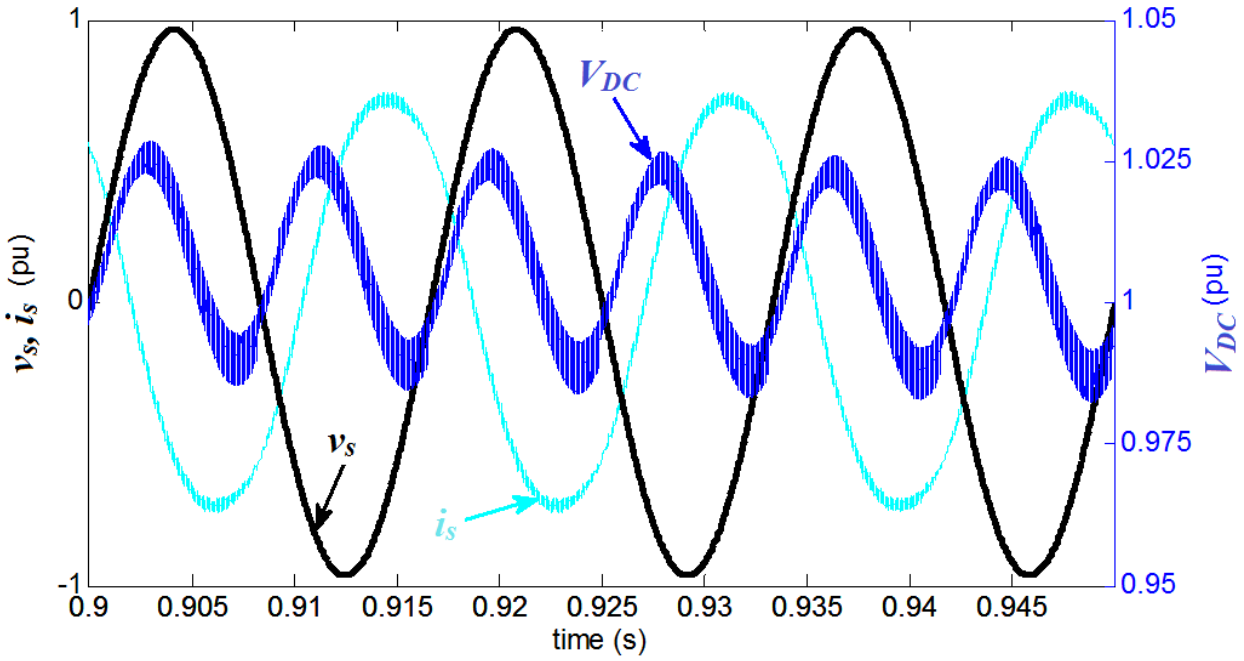

Figure 4-10. Steady-state response for Simulation 6,$P_s = -1.36$ kW and $Q_s = -1.36$ kVAR.

In Simulation 7, the Smart Charger provides 1.92 kVAR of pure reactive power to the grid, behaving as a purely capacitive load. The voltage lags the current by 90^{O}, $V_{DC,rip}$ is at its maximum value of 9.78 V, and $THD = 4.6\%$.

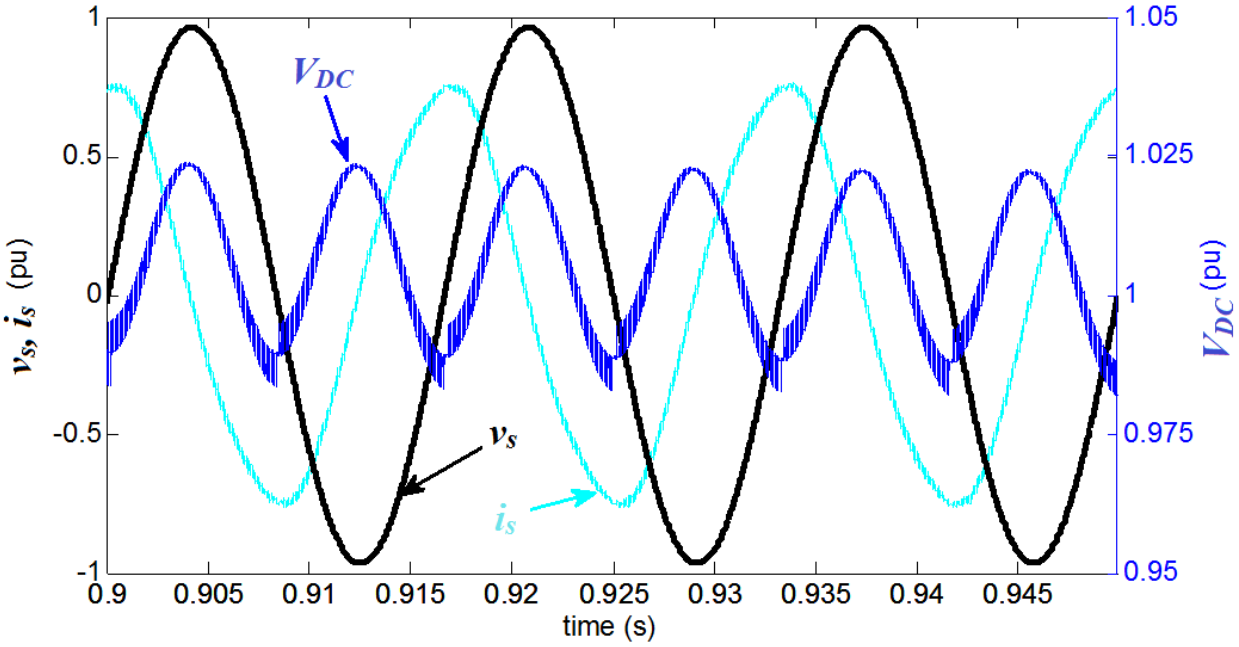

Figure 4-11. Steady-state response for Simulation 7, $P_s = 0$ kW and $Q_s = -1.92$ kVAR.

Simulation 8 has the Smart Charger charging the battery at 1.36 kW, providing 1.36 kVAR to the grid. In this case, $V_{DC,rip}$ decreases slightly to 9.60 V and THD drops to 4.5%.

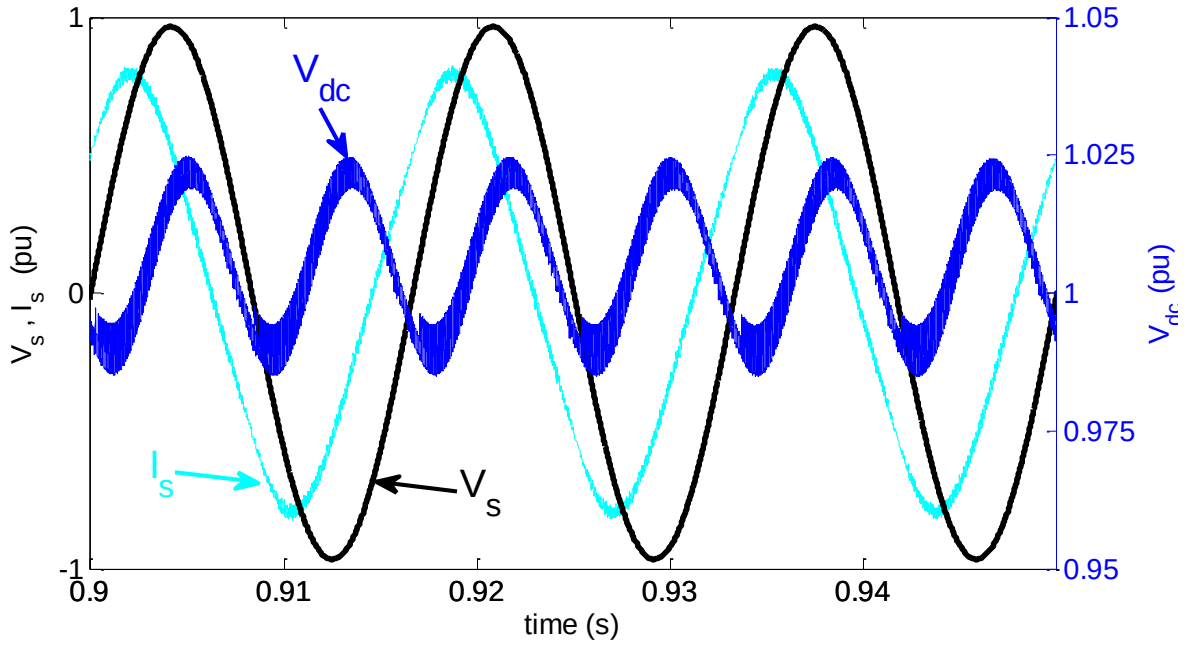

Figure 4-12. Steady-state response for Simulation 8, $P_s = 1.36$ kW and $Q_s = -1.36$ kVAR.

4.3 Step Response

The step-response plots demonstrate the controller's ability to effectively respond to P-Q requests with minimal overshoot or variance in the DC bus voltage. Active power, reactive power, battery voltage, battery current, and DC link voltage are shown on the same plot for two different control profiles. The normalized values of these parameters are given in Table 4-4, and a summary of the P-Q requests is given in Table 4-5, charging at 0.25, 0.75, and 1.5 seconds.

Table 4-4. Step-response plot parameter scaling.

Parameter	**1 pu**
P_s	2.2 kW
Q_s	2.2 kVAR
V_{batt}	105 V
I_{batt}	24 A
V_{dc}	350 V

Table 4-5. Step-response plots P,Q requests vs time.

	Step-response Plot 1		**Step-response Plot 2**	
Time (s)	P_s	Q_s	P_s	Q_s
0.25	1920	0	0	1920
0.75	-1920	0	0	-1920
1.5	1360	-1360	-1360	1360

Step-response plot 1 is shown in Figure 4-13. The instant the DC link capacitor is fully charged, the maximum P_s request is issued to the controller to start charging the battery. Battery voltage and current increase, causing a temporary decrease in the DC link voltage. Once the DC bus stabilizes a maximum P_s request to discharge the battery is issued. The sudden increase in current on the DC bus causes the voltage temporarily increase until the dq controller feeds that excess current back into the grid. At 1.5 seconds, a maximum power request with a 0.707 lagging power factor is issued. From the plot, it can be seen that the controller is able to respond to an array of P-Q requests, and can quickly switch between rated charging to rated discharging. The active and reactive power requests can also be issued simultaneously without causing transients in the system.

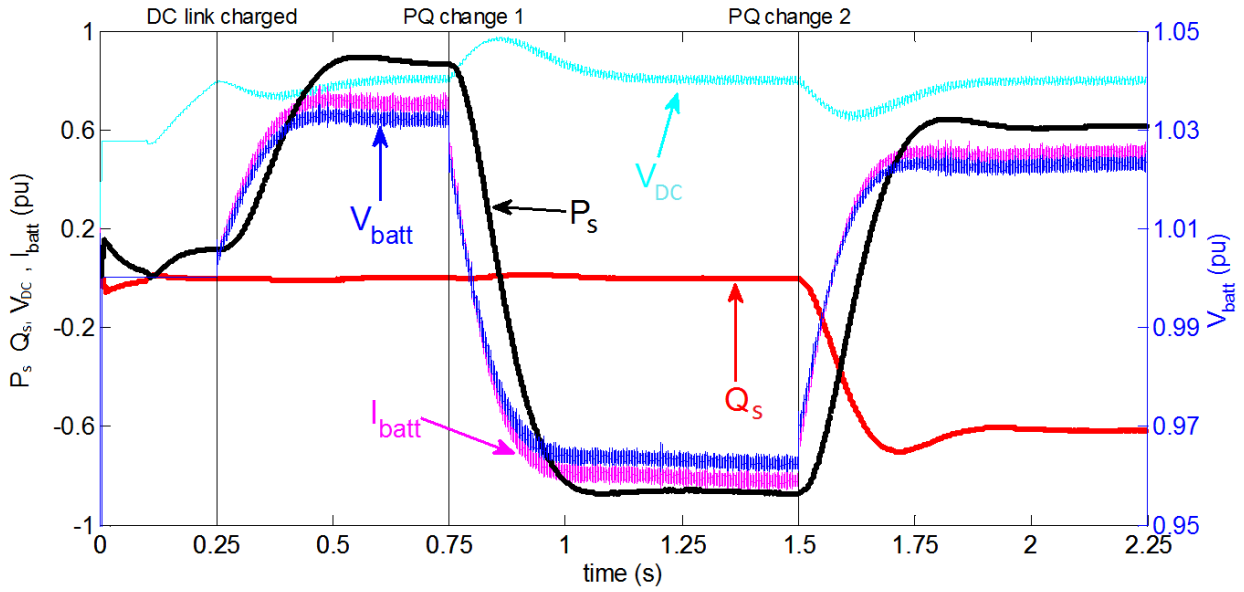

Figure 4-13. Step-response Plot 1.

Step-response plot 2 is shown in Figure 4-14. At 0.25 seconds a maximum reactive power request is issued, resulting in an active DC link voltage ripple increase, but there is no change in the DC link voltage. The active power remains unchanged showing decoupled control between active and reactive power requests. At 0.75 seconds a maximum negative reactive power request is issued; the DC link voltage ripple increases, as expected, and a slight overshoot occurs. At 1.5 seconds a change in the P-Q request is issued, showing again that various P-Q requests can be issued at the same time without causing any transients or strange behaviours in the system.

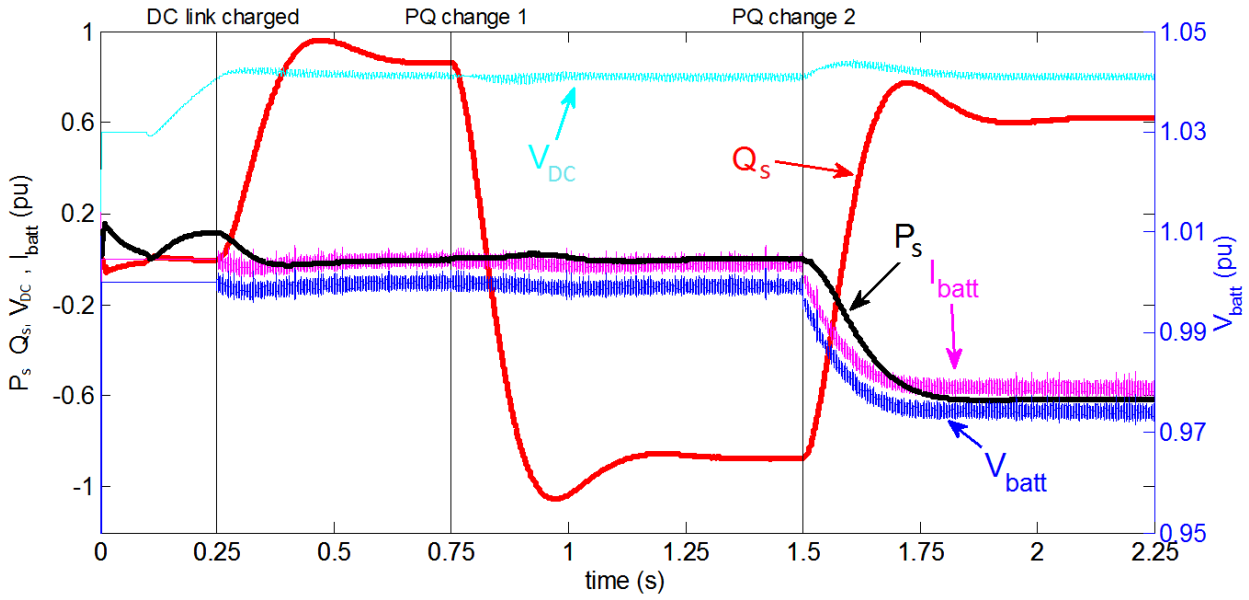

Figure 4-14. Step-response Plot 2.

4.4 Summary

The steady state response simulations validate three critical requirements of the Smart Charger. First, it shows that THD < 5% is possible for operation in all four quadrants of the P-Q plane, satisfying IEEE-1547. Next, it validates design equation (3.25) which states that as Q_s decreases, $V_{DC,rip}$ increases. Finally, it validates the bidirectional chargers ability to operate in all four quadrants of the P-Q plane. The step response demonstrates two important points. It shows that the active and reactive power requests are completely decoupled, and that the control is able to respond to sudden changes in P-Q requests without losing stability.

Chapter 5
Smart Charger Prototype Implementation

In this chapter the prototype Smart Charger is presented. First, the major components of the charger are shown, along with their specifications and justification for using each component in the overall setup. Next, the in-lab setup is presented, showing the major component interconnections. This is followed up with the steady-state and step response results of the Smart Charger, as presented for the simulations. A cost analysis is presented, and the chapter concludes with a general discussion, comparing the experimental and simulation results.

5.1 Prototype Main Components

The practical design of the Smart Charger can be divided into the design of four critical components, each of which is necessary for the charger to be smart and bidirectional. The first component is the Smart Charger Control Board, which contains all the low voltage components, voltage sensors, current transducers, low voltage power supply, and gate drive circuitry. The second component is the Smart Grid Interface Module, which makes the charger "smart" and facilitates the communication between the

charger and the utility. Next, the battery pack and BMS must be carefully chosen since interfacing with the control board is necessary for handling the power requirements. Finally, the central control unit connects the low voltage and controls the high voltage components.

5.1.1 Smart Charger Control Board

The Smart Charger Control Board is the primary Printed Circuit Board (PCB) that connects the low voltage power supplies, current transducers, voltage sensors, gate drive modules and central control unit. The PCB was designed with Altium Designer, and an overview of the design process is given in Appendix A.

The final board, populated with components, is shown in Figure 5-1. The top-left corner of the board contains six IGBT gate drivers, where a digital low (0V) or digital high (3.3V) PWM signal from the central control unit is converter to an isolated -8.2V or 15V signal, respectively. The low power DC power supplies convert 120VAC to -15V, 5V and 15V on GROUND1, which is the common ground for the voltage and currents sensors, BMS, Central Control Unit, and Smart Grid Communication Controller. A second DC power supply converts 120VAC to 5V, and 15V on GROUND2, which is the common ground for the IGBT gate drive components.

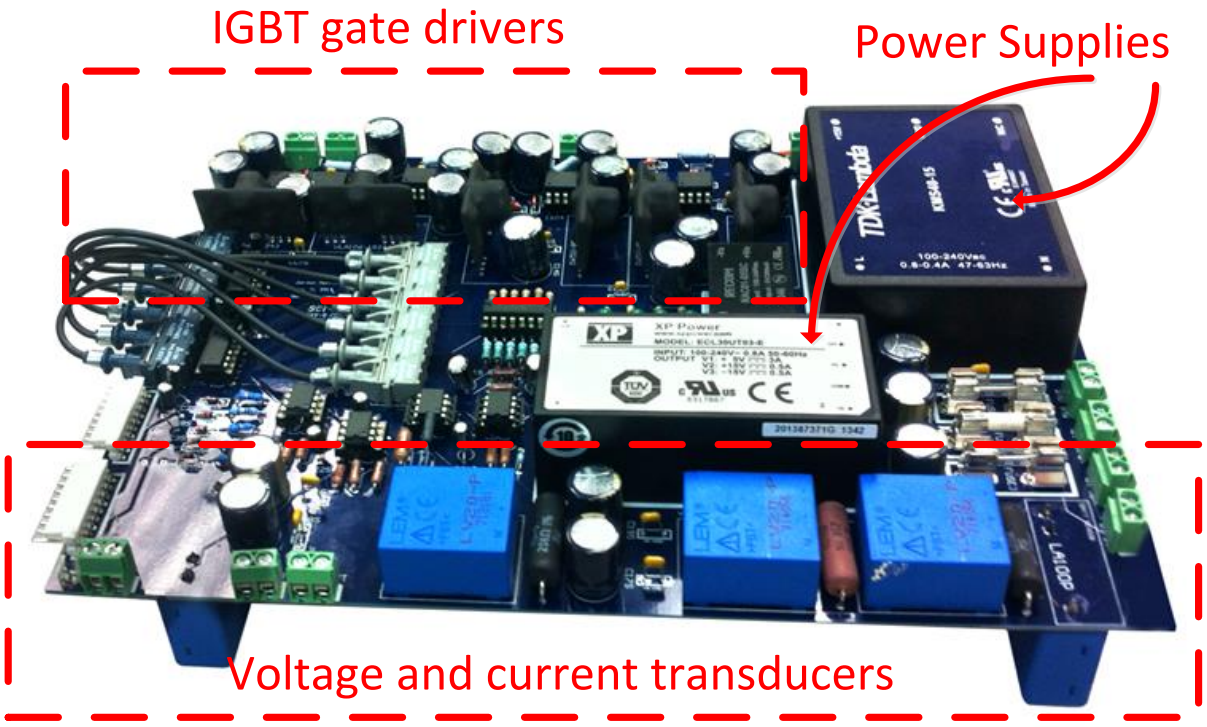

Figure 5-1. Smart charger Control Board.

5.1.2 Smart Grid Communication Controller

The Smart Charger must be able to interface with the Smart Grid, establishing a two way communication with the utility. As discussed in 1.2.2, cellular networks provide the highest reliability and flexibility at the lowest cost. As a proof of concept, a network controller capable of broadcasting a web page, that can receive user inputs wirelessly, is required. This controller must also be able to transmit these commands to the Smart Charger Central Control Unit for processing; therefore it needs a serial communication interface such as I2C, SPI, CAN or LIN. Based on these requirements, the SN8200 EVK from Muratta was chosen as the Smart Grid Communication Controller, with the product specifications given in Table 5-1.

Table 5-1. SN8200 EVK+ WiFi module evaluation kit specifications [62].

Technology	2.4 GHz IEEE 802.11b/g/n
Antenna technology	On-board
Transmit power	+18 dBm @b mode/11Mpbs
Max receive sensitivity	-96 dbm
Host Interface	UART, SPI
Sensor applications support	GPIO, I2C, ADC, DAC
Operating Temperature	-30^{O}C to $+85^{O}$C
Code Support	JS/HTML

The SN8200 EVK can be configured to act as wireless access point, capable of transmitting web pages, which HTTP clients, such as computers with WiFi adapters, can connect to. Since the controller is broadcasting its own network, domain names are not an issue. For more information regarding the connection process and how to communicate with the Smart Charger, see Appendix B.

5.1.3 Battery Pack and BMS

A Level 1 charger is capable of charging at rates up to 1.92 kW; therefore, it is required that the battery pack chosen for the experimental design be capable of handling this power requirement when the pack SOC is less than 80%. As explained in section 2.2, when the pack begins to approach 100% SOC, the charging current must decrease so that the battery is not damaged. Based on this, as long as the battery pack can charge at a minimum of 1.92 kW until 80% SOC, it will meet the compatibility requirements of the Smart Charger. Similarly, since the objective of this thesis is to design a smart bidirectional charger, the pack must be capable of discharging at a rate greater than 1.92 kW to meet the 1.92 kW demand at the grid interface and to cover the losses in the system. This of course is only a requirement when the pack SOC is above 20%, since high power discharge at low SOC damages the battery.

The pack voltage, capacity, and cost must also be factored into the decision. Practical limitations of the DC/DC converter make it advantageous to choose a pack with a higher nominal voltage, but this adds cost. The pack must have sufficient storage capabilities, but again this adds cost. Hence, based on all these considerations, a lithium-ion battery pack was purchased from Elite Power Solutions with the specifications given in Table 5-2.

Table 5-2. Battery Pack Specifications [63].

Battery Model	GBS-LFMP40AH
Cell Capacity (Ah)	40
Cell Count	32
Total Capacity (kWh)	4.1
Max Voltage (V)	115.8
Nominal Voltage (V)	102.4
Minimum Voltage (V)	89.6
Battery Weight (lbs)	118
Max Charging Current (A)	42
Serial Ports	CAN

5.1.4 Central Control Unit

The Central Control Unit (CCU) of the Smart Charger links the network controller, BMS, and Smart Charger Board together. The CCU must have an ADC module to read in the sensor data, must have a PWM module to control the IGBTs; CAN to communicate with the BMS; I2C to communicate with the SN8200 EVK; and sufficient FLASH and RAM to store and execute the firmware. The TMS320F2808 Digital Signal Processor (DSP) was chosen as the CCU, with product specifications given in Table 5-3.

Table 5-3. TMS320F2808 evaluation board product specifications [64].

Microcontroller	C2000
CPU	TMS320C28x
Code Support	C/C++
Memory	64K x 16 Flash, 18K x 16 SARAM
Boot ROM	4K X 16
Cycle Time	100 MHz (10 ns)
Peripherals	ePWM (6 channels)
	ADC (12 bit, 16 channels)
Serial Ports	CAN, I2C, SPI, UART, SCI

The central control unit is the interface that connects the four major components of the Smart Charger. The interaction of the major components, as well as the type of data transmitted between them is shown in Figure 5-2. The Smart Charger Control Board measures $v_s, i_s, V_{DC}, V_{batt}$, and I_{batt}, isolates the measurements and feeds the signals in the ADC of the CCU. Based on the these measurements, along with P-Q requests transmitted over I2C from the Smart Grid Communication Controller, IGBT control

signals are generated and passed back to the Smart Charger Control Board, which switches the IGBTs on and off. The BMS communicates with the CCU over CAN to broadcast battery pack SOC, over current protection, over voltage protection, and pack temperature.

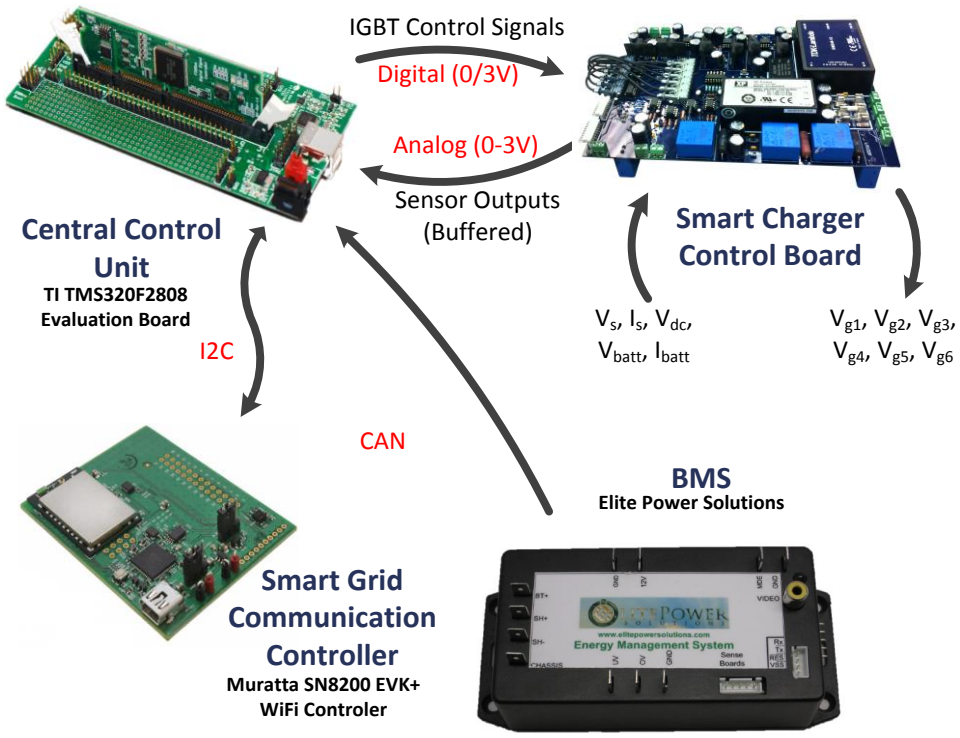

Figure 5-2. Smart Charger communication protocols.

5.2 Experimental Setup

The final prototype Smart Charger and battery pack for the experimental tests are shown in Figure 5-3. The Smart Charger itself is built from the ground up in three sections. The first and bottom section houses all the HV components. These components, especially the inductors, can generator a lot heat; therefore it is important that they are mounted on a heat sink. Also, to facilitate further cooling, fans are placed alongside the Smart Charger (not shown). Since the IGBTs are buried under copper bus bars, capacitors and the Smart Charger Control Board, it is difficult to show them in a clear picture as part of the final board design. Three IGBT legs are required, two for the AC/DC converter and one for the DC/DC converter. The legs are placed side by side and connected with copper bus bars. Each IGBT has a varistor

across its collector-emitter terminals to limit transients, and a snubber capacitor is placed across each leg to limit voltage spikes caused when the IGBT is turned on or off.

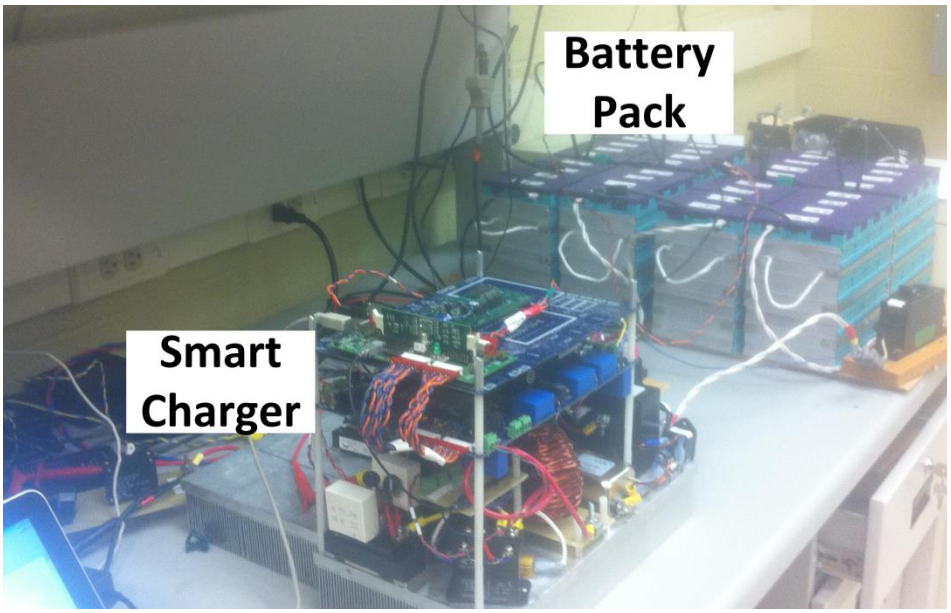

Figure 5-3. Smart Charger - battery pack layout.

Two HV connectors connect the Smart Charger to the grid and battery pack as shown in Figure 5-4. These connectors, along with one low voltage connector which connects the BMS to the Smart Charger, are all the connectors that are required. The AC voltage connector powers all the DC power supplies on the Smart Charger Control Board, which power the CCU.

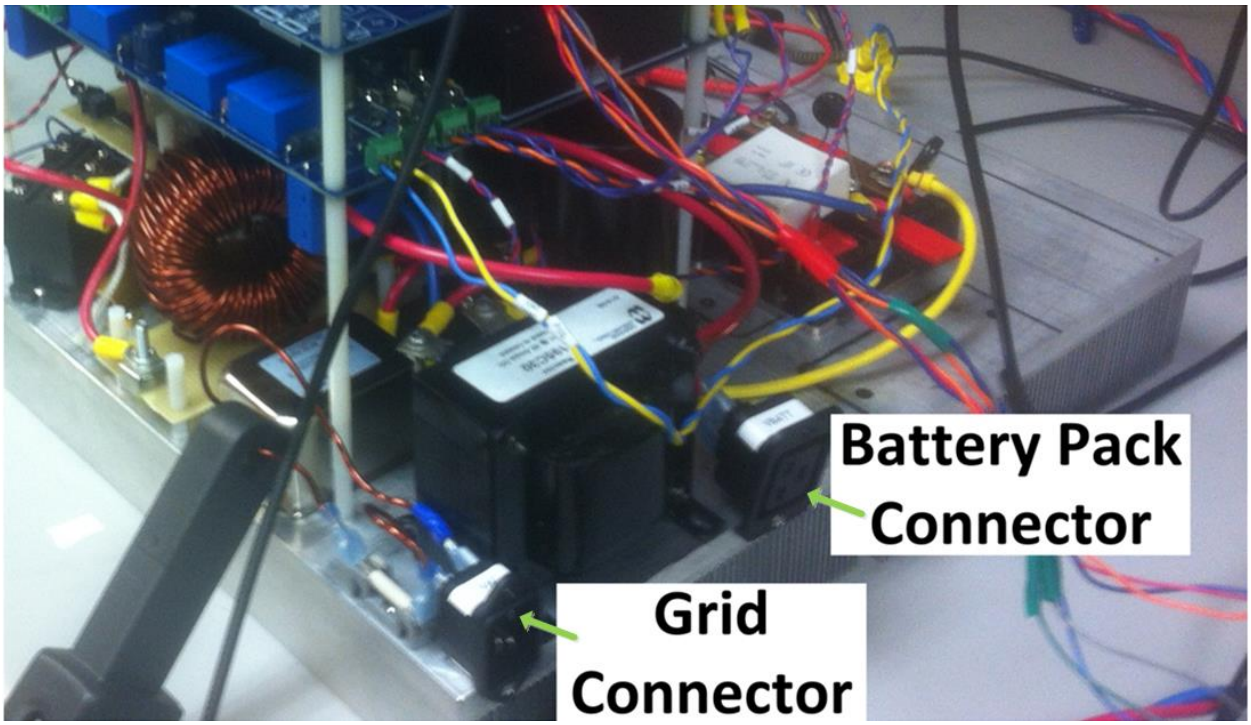

Figure 5-4. Smart Charger HV connectors.

Figure 5-5 shows the side view of the Smart Charger and Figure 5-6 shows the Smart Charger's top view. From the side view, the layers of the Smart Charger become apparent; however, it may still not be obvious how everything is interconnected. The top view of the Smart Charger displays how all the components connect to the CCU. The BMS has a low voltage connector, the WiFi controller connectors over I2C and also receives its power from the CCU. The CCU has two ribbon connectors that attach to the Smart Charger Control Board, one to receive the data from the voltage and current transducers, and another to send the PWM gate drive signals to the IGBTs.

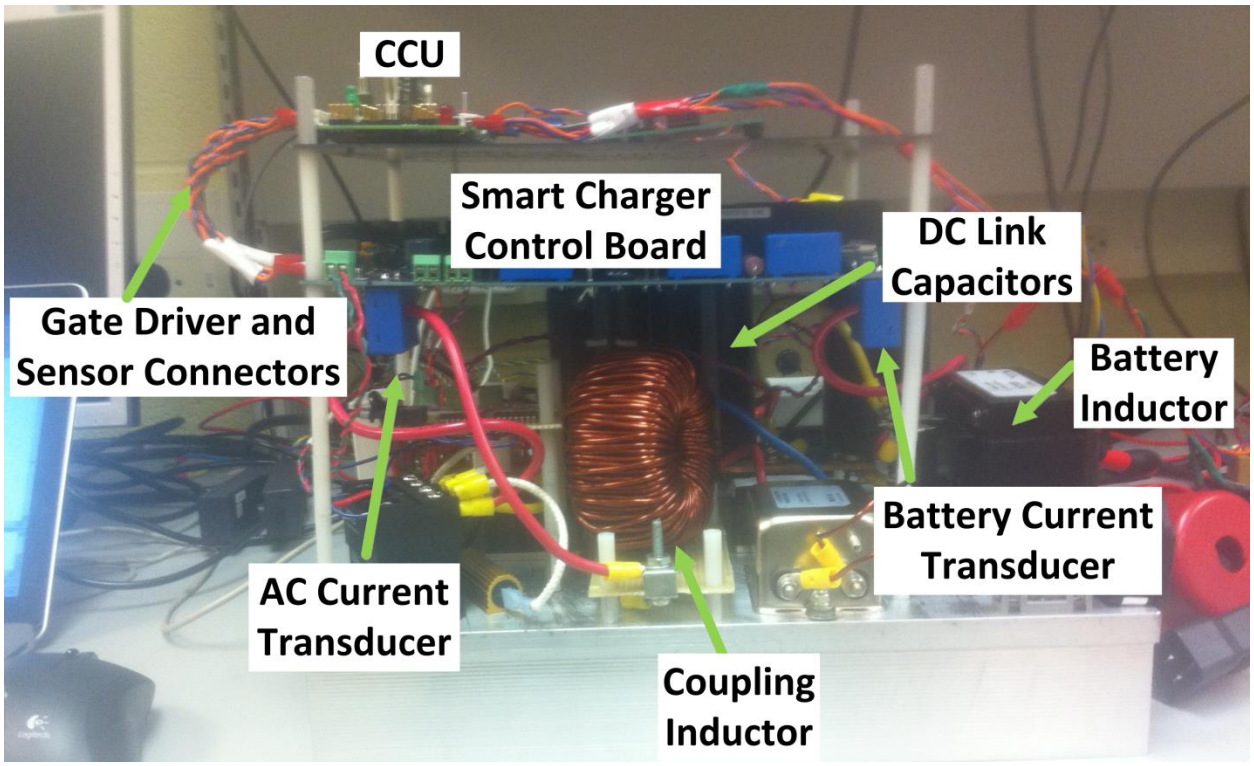

Figure 5-5. Smart Charger side view.

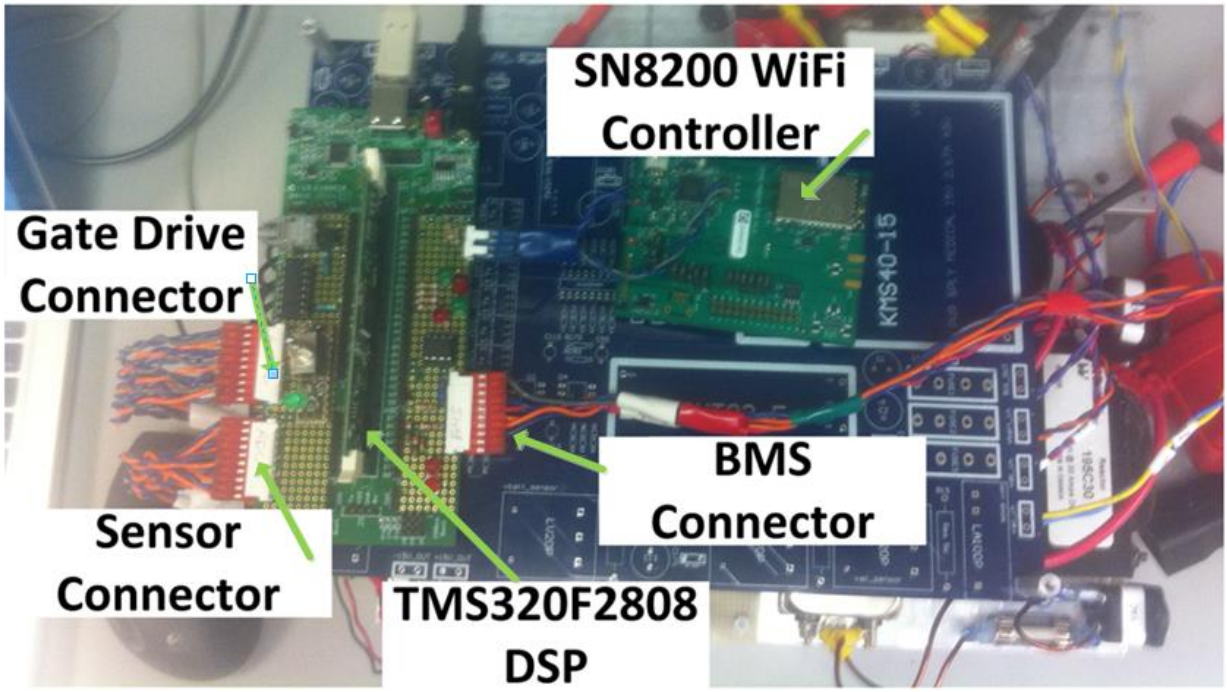

Figure 5-6. Smart Charger top view.

5.3 Prototype Response Characteristics

This section will present oscilloscope screen shots taken during operation of the prototype Smart Charger. Much like what was presented in Chapter 4, steady-state plots are shown to validate the ability of the prototype to operate in all four quadrants of the P-Q plane, and step-response plots show how the Smart Charger responds to changes in P-Q requests.

5.3.1 Steady-State Response

It is critical to validate the steady state response of the prototype Smart Charger operating in the four quadrants of P-Q, plane as well as on the boundaries between the quadrants. A summary of the P-Q requests issued to the prototype Smart Charger, as well as the corresponding figures is given in Table 5-4.

Table 5-4. Steady-state response experimental results summary.

Experiment	P_s (kW)	Q_s (kVAR)	Figure
1	1.7	0	Figure 5-7
2	1.2	1.2	Figure 5-8
3	0	1.7	Figure 5-9
4	-1.2	1.2	Figure 5-10
5	-1.7	0	Figure 5-11
6	-1.2	-1.2	Figure 5-12
7	0	-1.7	Figure 5-13
8	1.2	-1.2	Figure 5-14

The eight plots depicted here show the steady state response of v_s (green), i_s (blue), V_{DC} (red), and V_{batt} (orange). These plots demonstrate that the charger is capable of bidirectional power flow. Purely reactive requests are also demonstrated in Figure 5-9 and Figure 5-13, where the current lags and leads the voltage by 90^O, respectively. The DC link voltage ripple remains low during all modes of operation, never exceeding 10 V_{pp}, and the battery voltage ripple is also small.

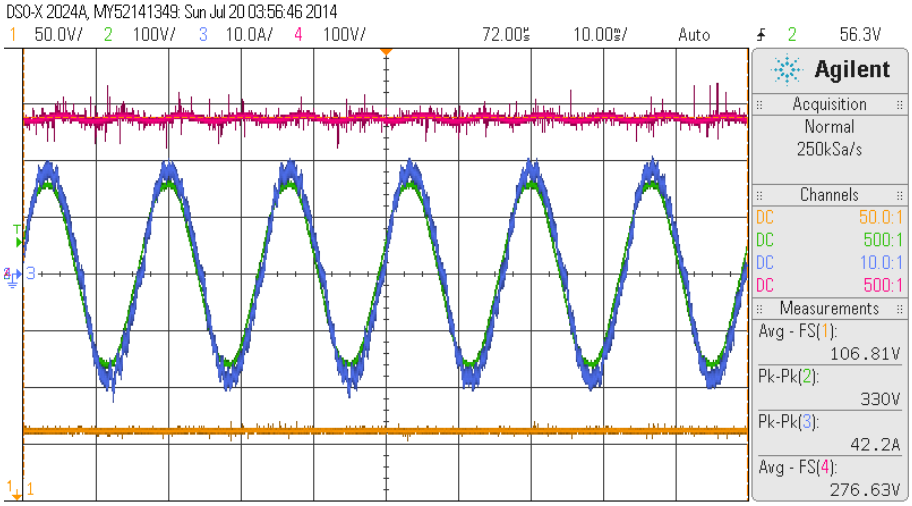

Figure 5-7. Steady-state response for Experiment 1, $P_s = 1.7$ kW and $Q_s = 0$ kVAR.

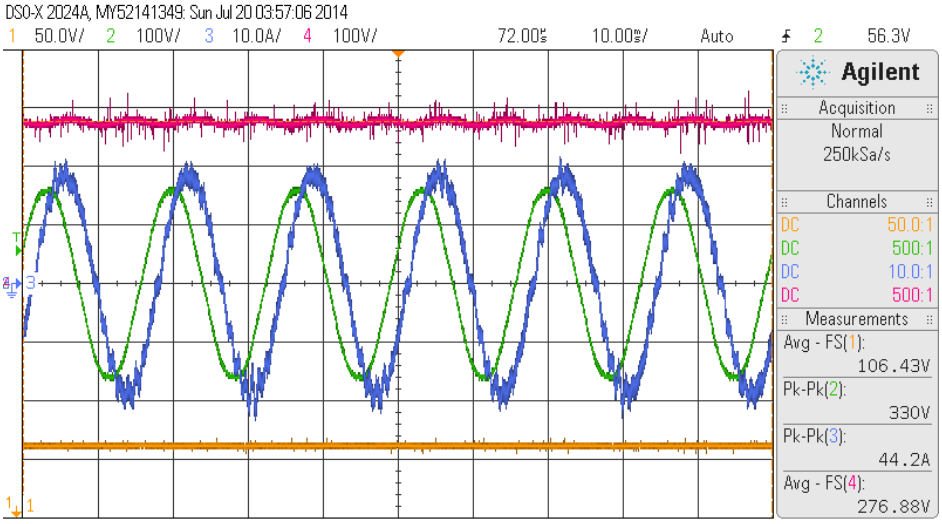

Figure 5-8. Steady-state response for Experiment 2, $P_s = 1.2$ kW and $Q_s = 1.2$ kVAR.

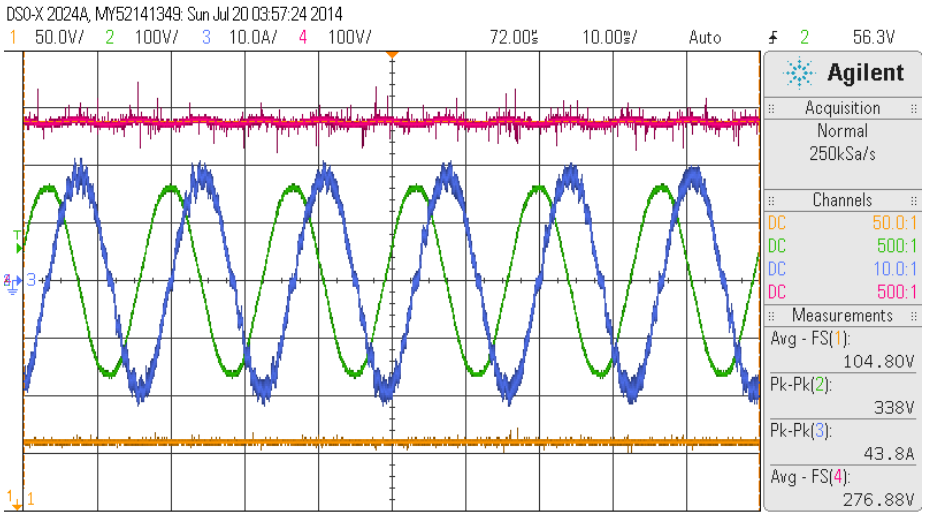

Figure 5-9. Steady-state response for Experiment 3, $P_s = 0$ kW and $Q_s = 1.7$ kVAR.

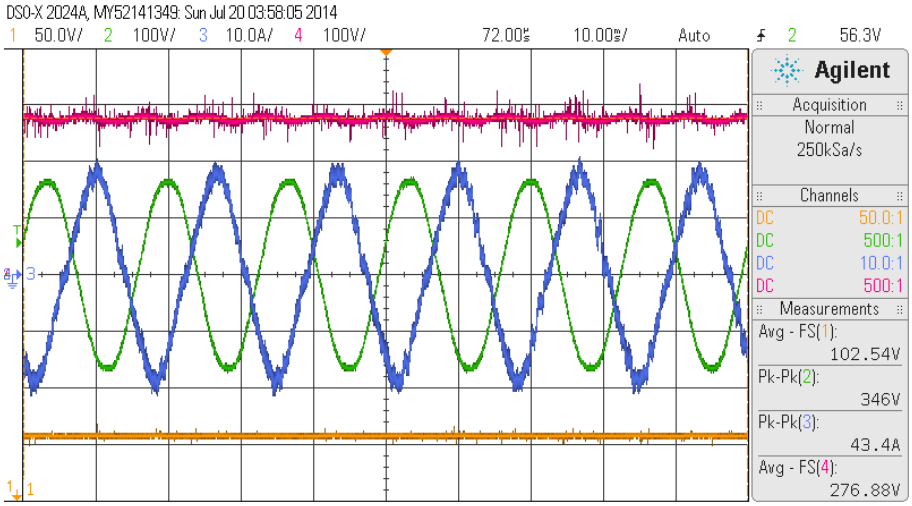

Figure 5-10. Steady-state response for Experiment 4, $P_s = -1.2$ kW and $Q_s = 1.2$ kVAR.

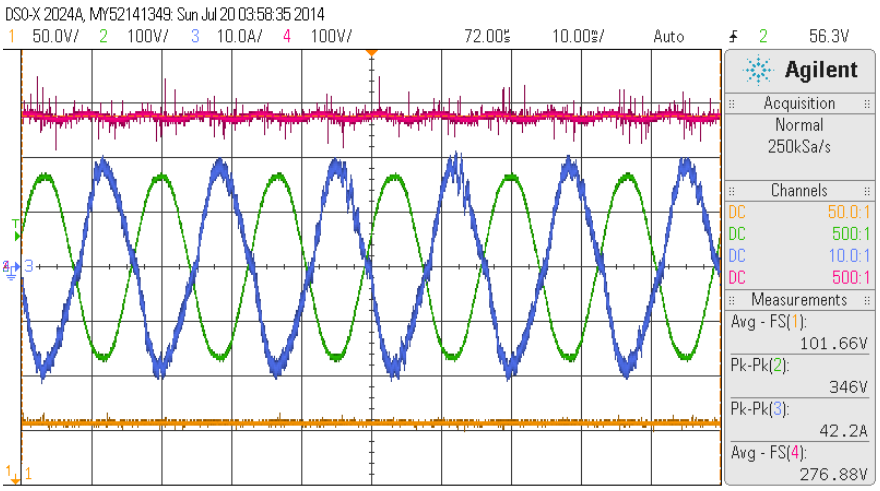

Figure 5-11. Steady-state response for Experiment 5, $P_s = -1.7$ kW and $Q_s = 0$ kVAR.

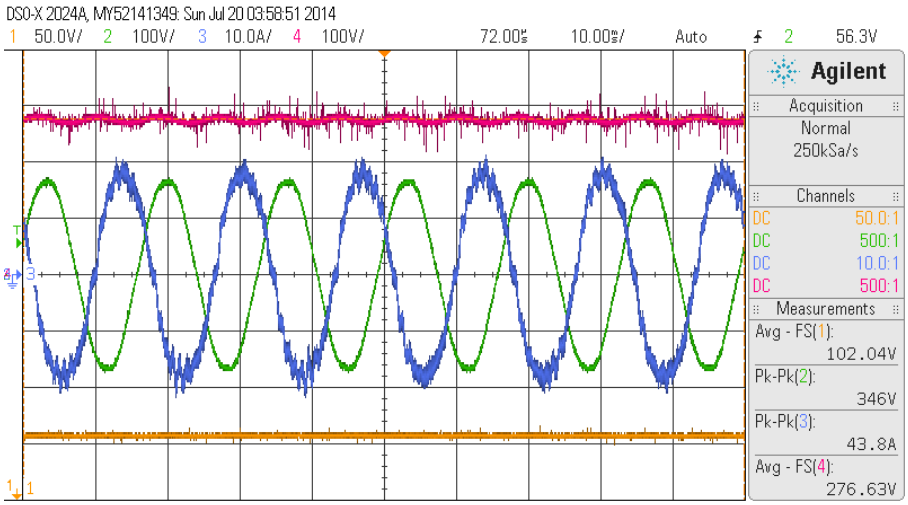

Figure 5-12. Steady-state response for Experiment 6, $P_s = -1.2$ kW and $Q_s = -1.2$ kVAR.

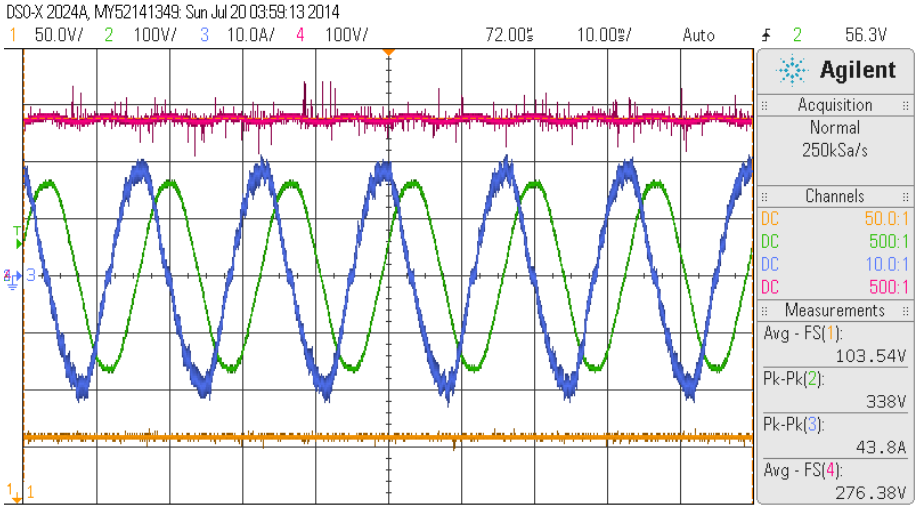

Figure 5-13. Steady-state response for Experiment 7, $P_s = 0$ kW and $Q_s = -1.7$ kVAR.

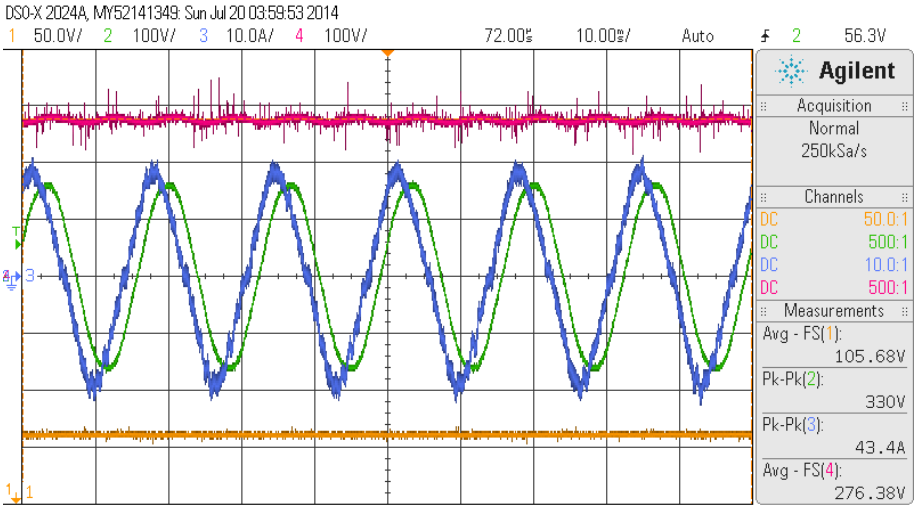

Figure 5-14. Steady-state response for Experiment 8, $P_s = 1.2$ kW and $Q_s = -1.2$ kVAR.

5.3.2 Step Response

The step-response plot of the prototype is shown in Figure 5-15, and a summary of the P-Q requests is given in Table 5-5. The step response shows V_{dc} (red), V_{batt} (yellow) and I_{batt} (blue) over a 50 second window. From the figure it can be observed that the controller has a slow response, as intended. Since there is no inherent advantage to having a fast response time, which can lead to overshoot, potentially charging the battery at a limit it is not rated for, the DC filter values were chosen such that it would not only filter the ripple in the P-Q requests, but also slow the response down and eliminate overshoot. The response time of the active power controller is much slower than that of the reactive controller, since the active power controller is directly coupled to the battery current. It should also be noted here that the voltage measurements show very large transients, which can be attributed to electrical interference of the measurement probe.

Table 5-5. Prototype step response P-Q request summary.

Request Time (s)	P	Q
0	1500	0
7	-1500	0
28	1100	1100

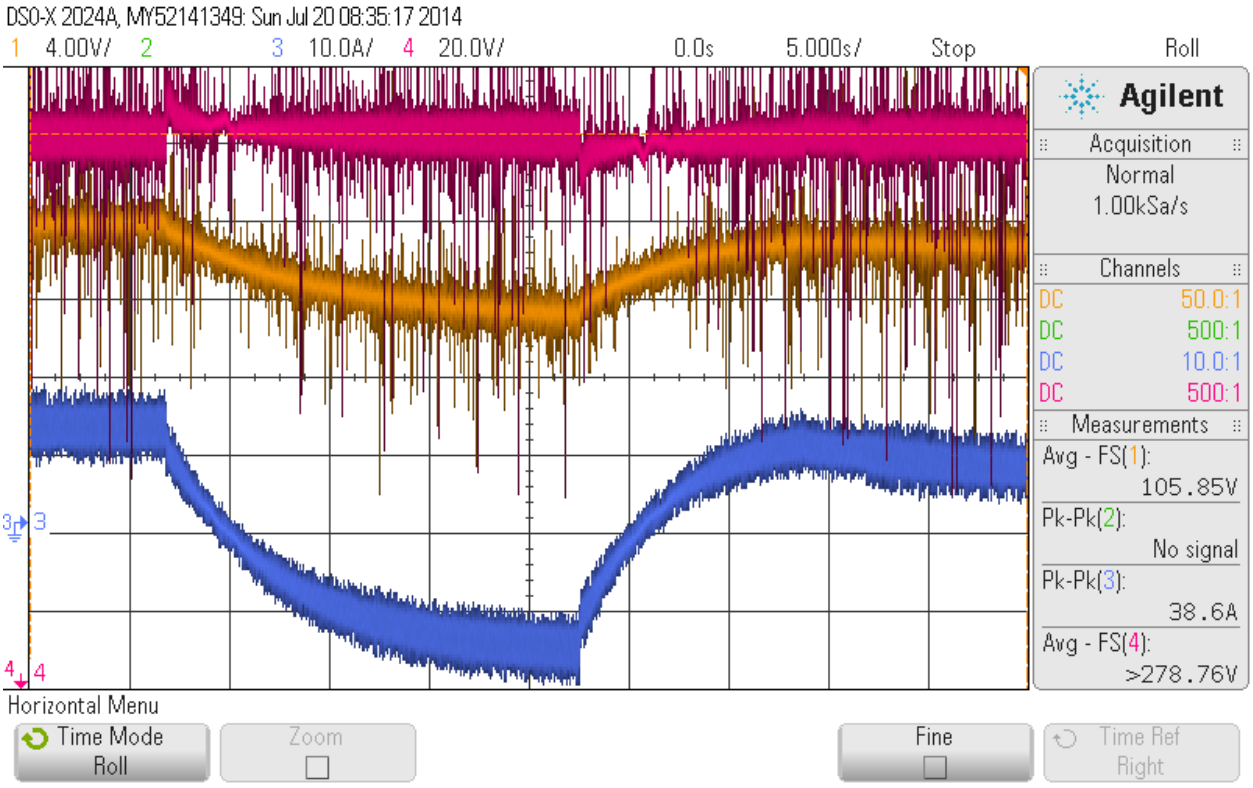

Figure 5-15. Prototype step response oscilloscope screenshot.

5.3.3 Efficiency Analysis

There are various sources of losses in a Smart Charger, such as IGBT switching losses, inductor core losses as well as inductor and capacitor losses caused by their ESR. Measuring each of these losses precisely is a difficult task, but measuring the losses of Smart Charger as a whole is a relatively straightforward exercise. Thus, the power at the PCC is defined as follows:

$$P_s = V_s I_s cos\theta \tag{5.1}$$

The battery power is defined as:

$$P_{batt} = V_{batt} I_{batt} \tag{5.2}$$

Since the Smart Charger is bidirectional, when referring to efficiency calculations, the input and output are interchangeable. Hence, for positive active power requests, i.e., when power is flowing into the battery, the input is the PCC and the output is the battery. Conversely, when the active power request is negative, the input and output definitions are interchanged. This is important to establish, since the input

component will be the one to cover the chargers losses, thus always having a greater power than the output.

The definition of efficiency is given by:

$$\eta = \frac{P_{out}}{P_{in}} \tag{5.3}$$

The true efficiency of the Smart Charger is best evaluated based on unity power requests. Reactive power requests will, by design, decrease efficiency and make it difficult to determine the true system losses. Efficiency has been calculated for two cases; thus in case 1, $P_{req} = 1.7$ kW, and in case 2, $P_{req} = -1.7$ kW, with the results summarized in Table 5-6. For both cases, the efficiency is comparable with an average efficiency of 89%.

Table 5-6. Efficiency calculations.

Metric	**Case 1**	**Case 2**
$P_{req}\ (kW)$	1.7	-1.7
$V_s\ (V)$	120	120
$I_s\ (A)$	14.1	14.14
$V_{batt}\ (V)$	106.8	101.6
$I_{batt}\ (A)$	14.20	18.9
$P_s\ (kW)$	1.692	1.697
$P_{batt}\ (kW)$	1.517	1.92
$\eta = \frac{P_{batt}}{P_s}$	89.65	
$\eta = \frac{P_s}{P_{batt}}$		88.38

5.4 Comparison

The simulation results presented in Chapter 4 show that the chosen charger configuration would be capable of bidirectional power flow for P-Q requests less than 1.92 kVA. However, based on the experimental results presented in section 5.3, it can be observed that there are notable differences between the simulation and experimental results; most notably, efficiency, third harmonics, and current wave shaping. Thus, as expected, the efficiency of the prototype Smart Charger is much less than that of the simulations. This is because all the losses in the simulations are intentionally added in the form of ESRs, and losses due to heat generation are not accounted for.

The experimental current waveforms show the presence of a third harmonic, which can be seen at the zero crossing mark, where the current flattens. Third harmonics are always a concern when dealing with single phase systems, unlike 3 phase systems, where the 120^{O} separation of each phase eliminates the third harmonic in the prototype. In theory, a full-bridge AC/DC converter should be able to completely eliminate the third harmonic, but unfortunately the third harmonic remains. Potential solutions include increasing the size of the coupling inductor and retuning the PI regulators in the AC/DC converter. There were also issues producing a stable current wave shape which is a result of poor current tracking. This is in part a result of the chosen current sensor, and the AC current conditioning circuit linking the measured current to the ADC on the CCU.

5.5 Prototype Bill of Materials

The Smart Charger bill of materials is presented in Table 5-7, with a total cost of $2,207.75. The "smart" aspect of the charger is entirely implemented with the WiFi network module highlighted in blue and accounting for $242.57 (10.98%) of the total cost. Since this is a single unit production, the cost of producing this unit is much greater than the cost of a mass produced unit. The greatest cost for the charger comes from the IGBTs accounting for $306.66 (13.89%) of the total cost. Miscellaneous items include low cost components such as small resistors, small capacitors, fuses, cables, connectors, fiber optic cables, diodes, standoffs, low cost ICs, magnet wire, switches, and heat shrink.

Table 5-7. Smart Charger bill of materials.

Component	Quantity	Unit Cost (CAD)	Net Cost (CAD)
IGBT (CM150DUS-12F)	3	$102.22	$306.66
AC/DC CONVERTER 5V +/-15V 30W	1	$98.86	$98.86
CHOKE DC REACTORS 1.0mH 30A	1	$89.47	$89.47
FAN 115VAC 120 X 38MM 105CFM	3	$17.11	$51.33
PWR SPLY MEDICAL 15V 2.67A 40W	1	$89.91	$89.91
SENSOR CURRENT 100A TH	2	$33.45	$66.89
TRANSDUCR VOLTAG CLOSE LOOP 10MA	3	$48.23	$144.68
CAP ALUM 1000UF 500V 20% SCREW	3	$53.80	$161.40
INDUCTOR FERRITE CORE	1	$32.30	$32.30
XMITTER FIBER OPTIC 600NM 5MBD	6	$13.48	$80.87
RECEIVER FIBER OPTIC 600NM 5MBD	6	$13.48	$80.87
OPTOCOUPLER GATE DVR 2.5A 8-DIP	6	$6.38	$38.29
PS CONVERTER DC/DC ISO 100MA 24V	6	$18.49	$110.94
POWER SUPPLY 5V, 1W	1	$14.72	$14.72
IC OPAMP VFB 80MHZ RRO 8DIP	4	$5.42	$21.69
CAP ALUM 390UF 35V 20% RADIAL	36	$0.77	$27.81
VARISTOR 558V 7.5KA DISC 17.5MM	18	$1.14	$20.52
RELAY GEN PURPOSE DPST 30A 12V	1	$18.92	$18.92
SMART CHARGER PCB	1	$200.00	$200.00
KIT EXPERIMENTER TMS320F2808	1	$109.05	$109.05
WI-FI NETWORK MODULE EVK	1	$242.57	$242.57
MISCELLANEOUS	1	$200.00	$200.00
TOTAL			**$2,207.75**

5.6 Summary

This chapter outlined the implementation process of a Smart Prototype Bidirectional Charger. First the prototypes main components were presented, which included the Smart Charger Control Board, smart grid communication controller, battery pack and BMS, and central control unit, followed by a summary of these components communication protocols. The final prototype was then shown, followed by oscilloscope plots of the frequency and step response. Efficiency analysis was done, followed by a

comparison of the experimental and simulation results and the chapter concluded with efficiency analysis and a discussion of the prototypes bill of materials.

Chapter 6
Conclusions

6.1 Summary

In Chapter 1, a discussion of the potential threat EVs pose on the future smart grids was presented, leading to the motivation to design a Smart Charger which can not only eliminate this threat but improve the future smart grid operation. The literature review presented focused on existing bidirectional EV charger topologies and smart grid communication technologies. Finally, the research objectives of the thesis were presented, followed by the thesis outline.

In Chapter 2, all relevant background information was presented. This chapter began with a review of the relevant standards (SAE J1772 and IEEE 1547), followed by a review of the battery model, charging algorithm, limitations, and cell balancing technique of lithium-ion batteries. Finally, a review of existing AC/DC converter controllers was presented, focusing on two well-known control strategies, the single phase dq controller and PR controller.

In Chapter 3, the Smart Charger design process was presented. Based on the analysis done in Chapter 2 and the review in Chapter 1, the Smart Charger topology and battery model were finalized. The

reactive power controller was designed based on a hybridization of the known dq controller, and a constant power active controller was presented. The chapter concluded by determining the optimal size of the high voltage components, DC link voltage, and battery voltage. The design work done in this chapter laid the foundation for the simulations and experimental implementation in the subsequent chapters.

In Chapter 4, the simulation results of a bidirectional charger were presented and discussed. The chapter focused on the steady-state and step response characteristics. The steady-state response plots were presented for eight P-Q set points, one in each quadrant of the P-Q plane, as well as for purely active and reactive set points, both positive and negative. The step response plots focused on the controller's ability to respond to changes in P-Q requests with minimal overshoot or DC link voltage fluctuations. The results of this chapter showed confidence in the design decisions made in Chapter 3

Chapter 5 outlined the implementation process of a Smart Prototype Bidirectional Charger. First the prototypes main components were presented, which included the Smart Charger Control Board, smart grid communication controller, battery pack and BMS, and central control unit. The final prototype was then shown, followed by oscilloscope plots of the frequency and step response, much like what was presented in the simulation chapter. Efficiency analysis was done, followed by a comparison of the experimental and simulation results and the chapter concluded with efficiency analysis and a discussion of the prototypes bill of materials. Chapter 5 confirmed that a practical implementation of a smart bidirectional on-board charger, capable third-party control, is possible.

6.2 Contributions

The main contributions of this thesis are:

- Development and design of a bidirectional control strategy for a charger that requires two inputs, active power (P_s) and reactive power (Q_s)

- Development, implementation, and testing of a functional working prototype of a Level 1 Smart Bidirectional Charger with a wireless interface so that P-Q set points can be issued to the charger from anywhere by logging into the Smart Charger Control Interface.

6.3 Future Work

Based on the work of this thesis and the results obtained, two major areas for future work are being proposed:

- The experimental results obtained from the prototype demonstrated the presence of a third harmonic component in the AC current waveform, as well as issues with tracking the reference AC current. Work has already begun to determine the cause of the third harmonic and potential solutions have been proposed. These solutions include: refining the control strategy and/or retuning the PI regulators of the DQ controller as well as making modifications to the hardware. This should eliminate the third harmonic in the AC current. On the other hand, to solve the AC current improper tracking, the sensor coupling circuitry could be redesigned.
- The work of this thesis has been part of a larger project, funded by NSERC and Hydro One, to determine the impact of EVs smart grids. The purpose of this thesis was to prototype a Smart Charger, to be used in the work of PhD students in the area of controlling EV charging, more specifically to control EV charge/discharge in residences and the control of fleet charging. Hence, the developed prototype can be used in the implementation of hierarchal smart charging controls in real time.

Appendix A
Smart Charger Control Board Design

The Smart Charger Board can be divided into four major segments; the gate driver optical fiber transmitter, optical fiber receiver/gate drive module, the onboard power supplies, and the sensor conditioning circuits.

A.1 Gate Driver Optical Fiber Transmitter

The gate driver optical fiber transmitter's primary purpose is to isolate the CCU from the gate drive modules. Figure A-1 shows the Altium Designer schematic of the six gate drive optical fiber transmitters on the board. The CCU's six PWM outputs are represented by the yellow rectangle on the left had side of the schematic. The signal is fed into an inverter, which serves as a buffer, limiting the current draw from the CCU. The output of the inverter is then fed into a LED driver which controls the transmission of the optical signal through the fiber optic connection (HFBR-15X1Z). Not only does this circuit ensure isolation between the CCU and the gate drive module, but it also eliminates noise that may be accrued between the CCU and optical fiber transmitter.

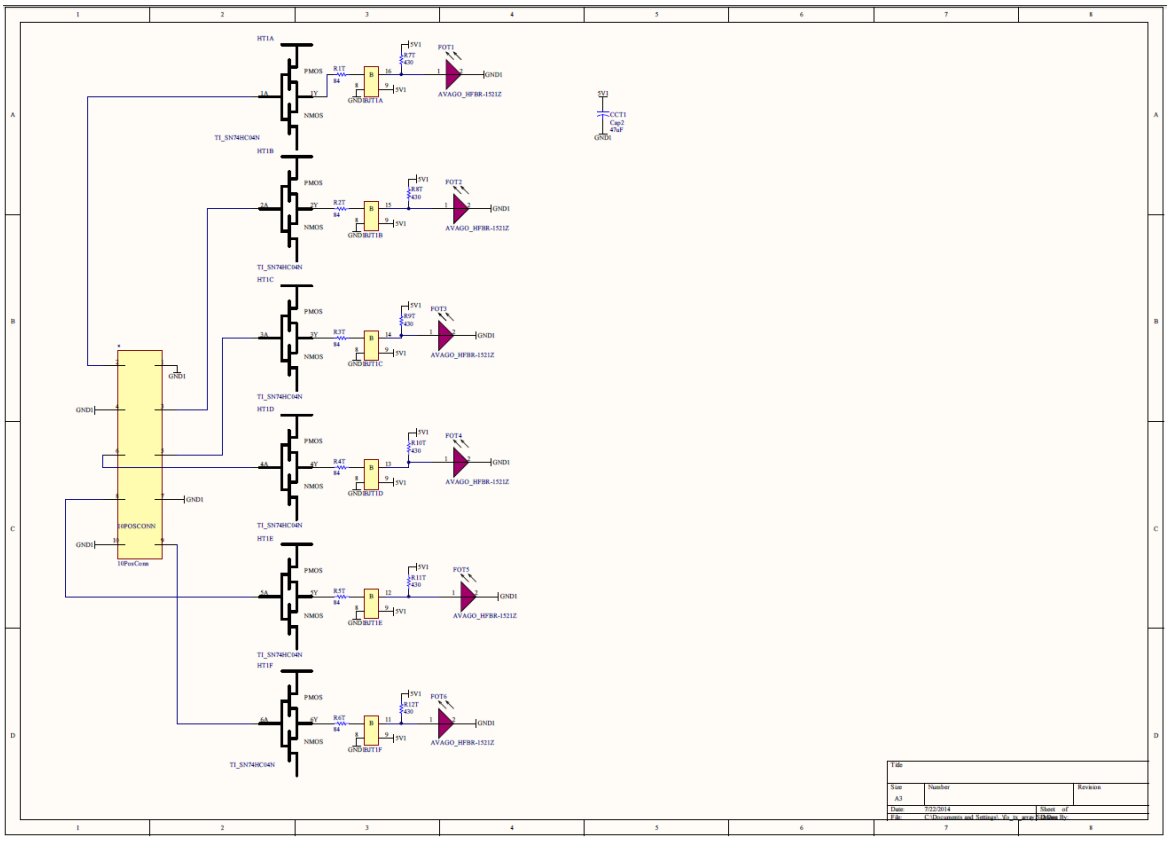

Figure A-1. IGBT gate driver optical fiber transmitter.

A.2 Optical Fiber Receiver/Gate Driver Module

The other end of the optical fiber connector (HFBR-25X1Z) is connected to the gate driver module as shown in Figure A-2. The signal is passed through an inverter and to a gate drive optocoupler (ACWN3130). The optocoupler outputs are linked to +15 V and -8.2 V generated by an isolated DC-DC converter (VLA106-15242), which requires +15 V. When the optocoupler is drawing current on its primary side, the output is connected to the +15 V side of the DC-DC, generating 15 V between the gate and emitter of the IGBT. When the primary side is not pulling current, the output is tied to the -8.2 V side of the DC-DC, placing 8.2 V between the emitter and gate of the IGBT. Large capacitors (330 µF) are placed between the two DC-DC outputs and the emitter. These capacitors are necessary to quickly push charge onto the IGBT to turn it on and to quickly pull the charge off the IGBT to turn it off.

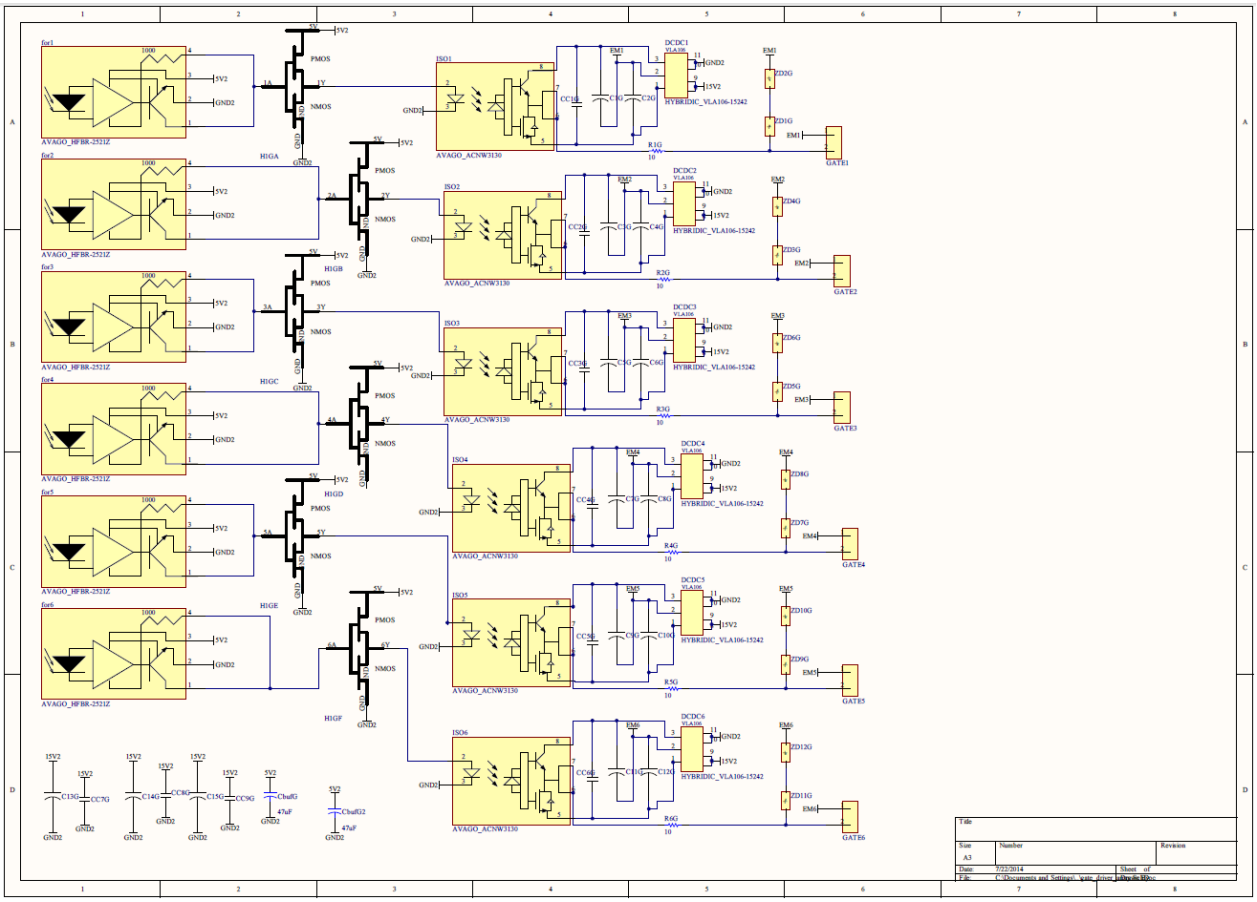

Figure A-2. Optical fiber receiver/gate driver module.

A.3 Voltage/Current Sensors Conditioning Module

The voltage/current sensor conditioning module is shown in Figure A-3. The Smart Charger contains three voltage transducers and two current transducers; however the voltage transducers themselves are actually low current transducers, placed in series with a large resistor across the voltage element it is measuring. The voltage transducers (LV-20P) output to input current conversion ratio is 25:10, whereas the current transducers (LA-100P) have a conversion ratio of 1:2000. Since both the current and voltage transducers operate on the same principle, the output of each of the transducers is tied to a resistor, whose value is selected such that it creates an output voltage between -1.5 V and +1.5 V for AC signals and 0-3V for DC signals. AC signals are then fed into an inverting amplifier with a +1.5 VDC offset such that the signal is now 0-3V. 0-3V is necessary since the input of the ADC on the CCU (TMS320F2808) requires a voltage

in that range. The signal is then passed through a low pass filter to eliminate noise and is connected to the ADC of the CCU.

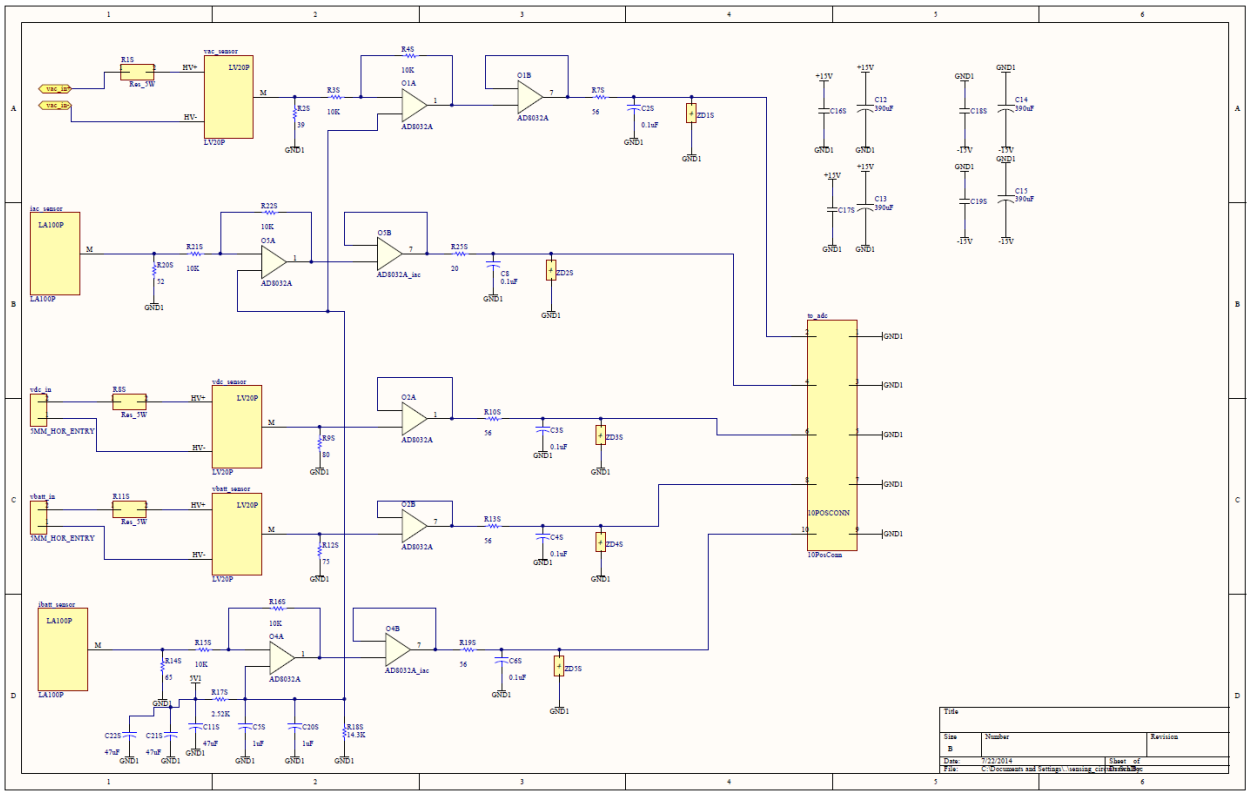

Figure A-3. Voltage/current sensor conditioning module.

A.4 Power Supply Module

The power supply module supplies the various DC voltage requirements of the onboard components as shown in Figure A-4. The board is divided into two grounds. One ground contains all the voltage/current sensors, their conditioning circuits and is also tied to the CCU and Wi-Fi network controller. These components are powered by the ECL30UT03 AC/DC power supply which takes 120 VAC as an input and outputs +/-15 V and +5 V. The gate drive components require a separate ground so it is supplied by a separate +15 V supply (KMS40-15) which takes 120VAC as the input. Another 5 V supply (VSK-S1-5U) is connected to the second ground to supply the +5 V requirement of the components.

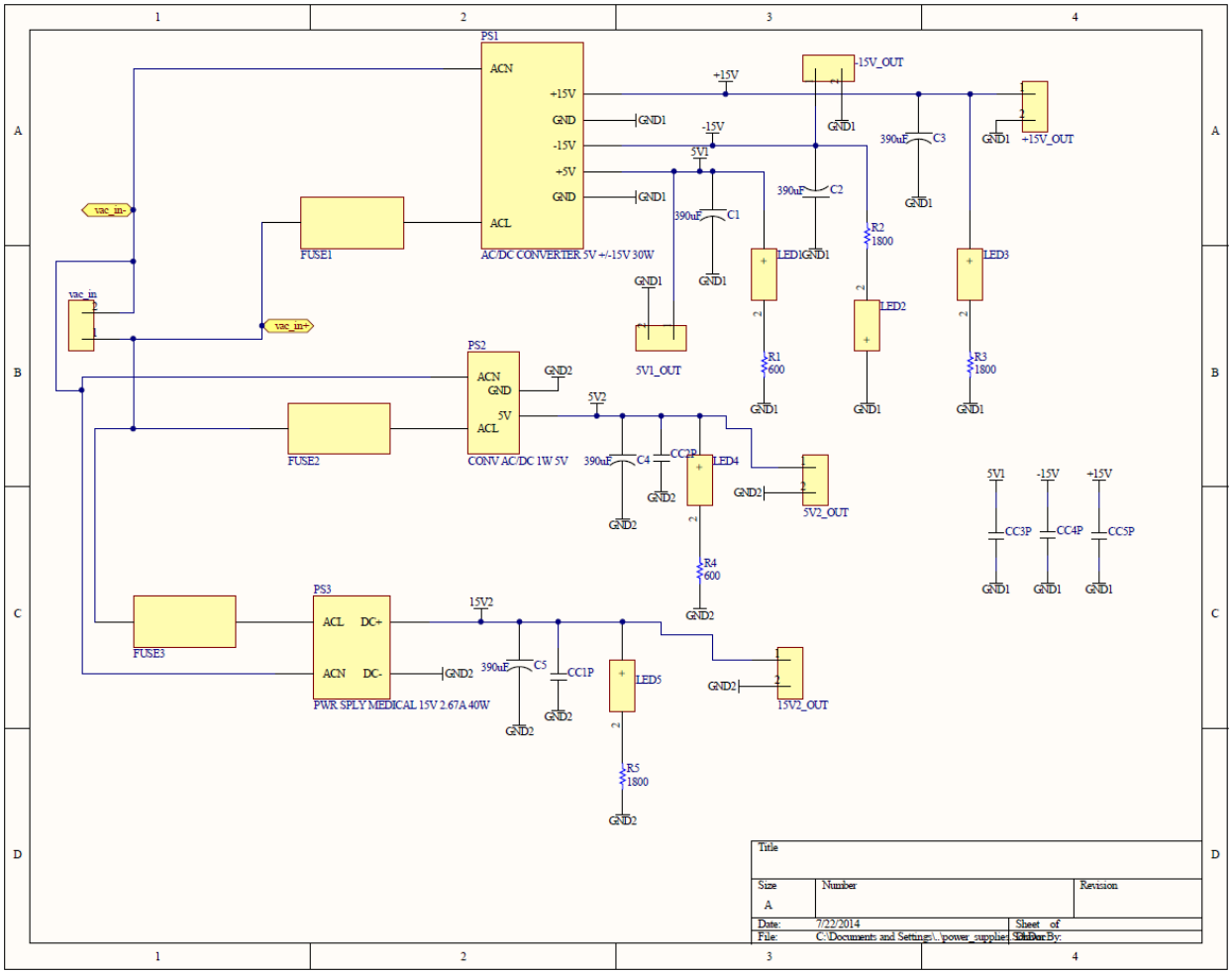

Figure A-4. Power supply module.

A.5 Smart Charger Printed Circuit Board Layout

The final circuit board layout for the Smart Charger Board is shown in Figure A-5 and the populated board is shown in Figure A-6.

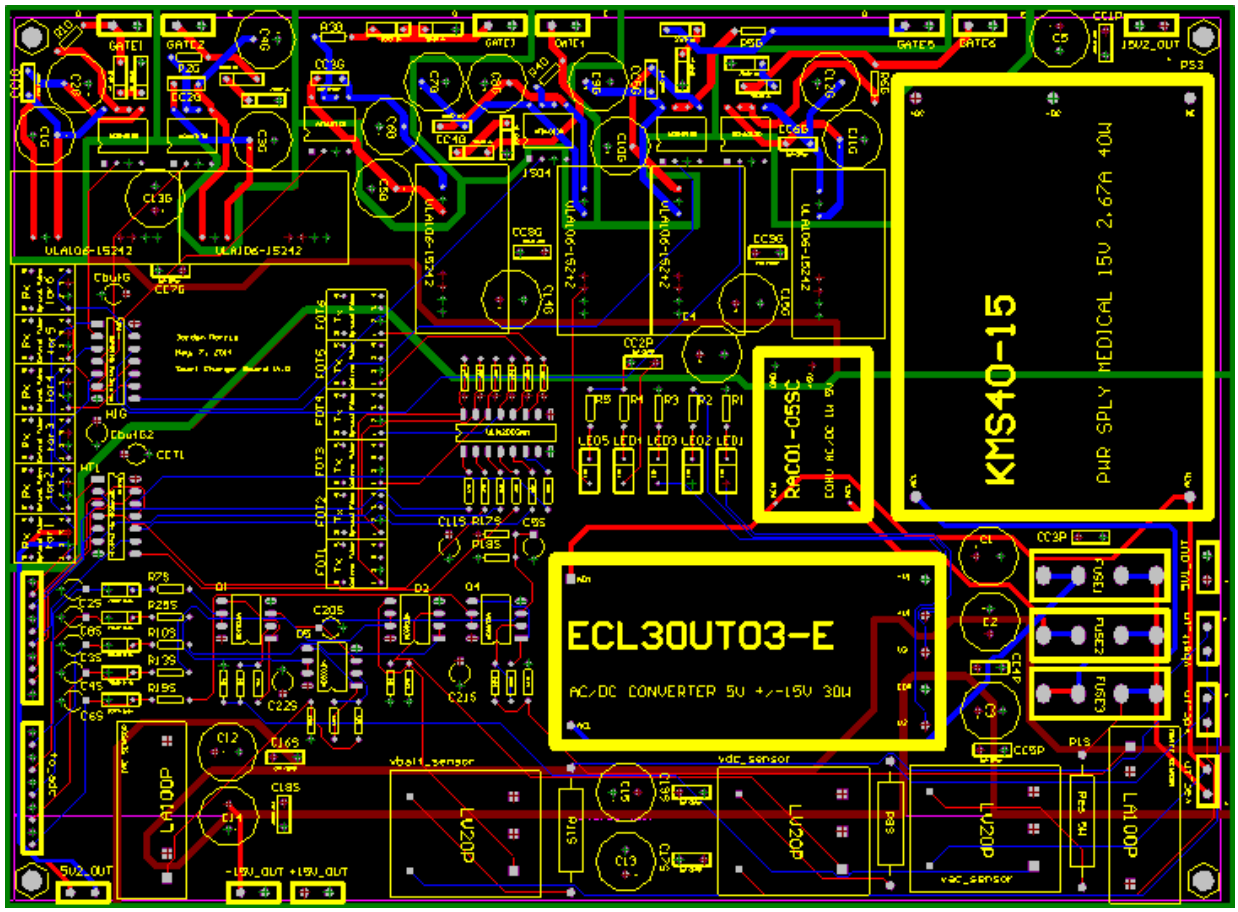

Figure A-5. Smart Charger Control Board PCB layout.

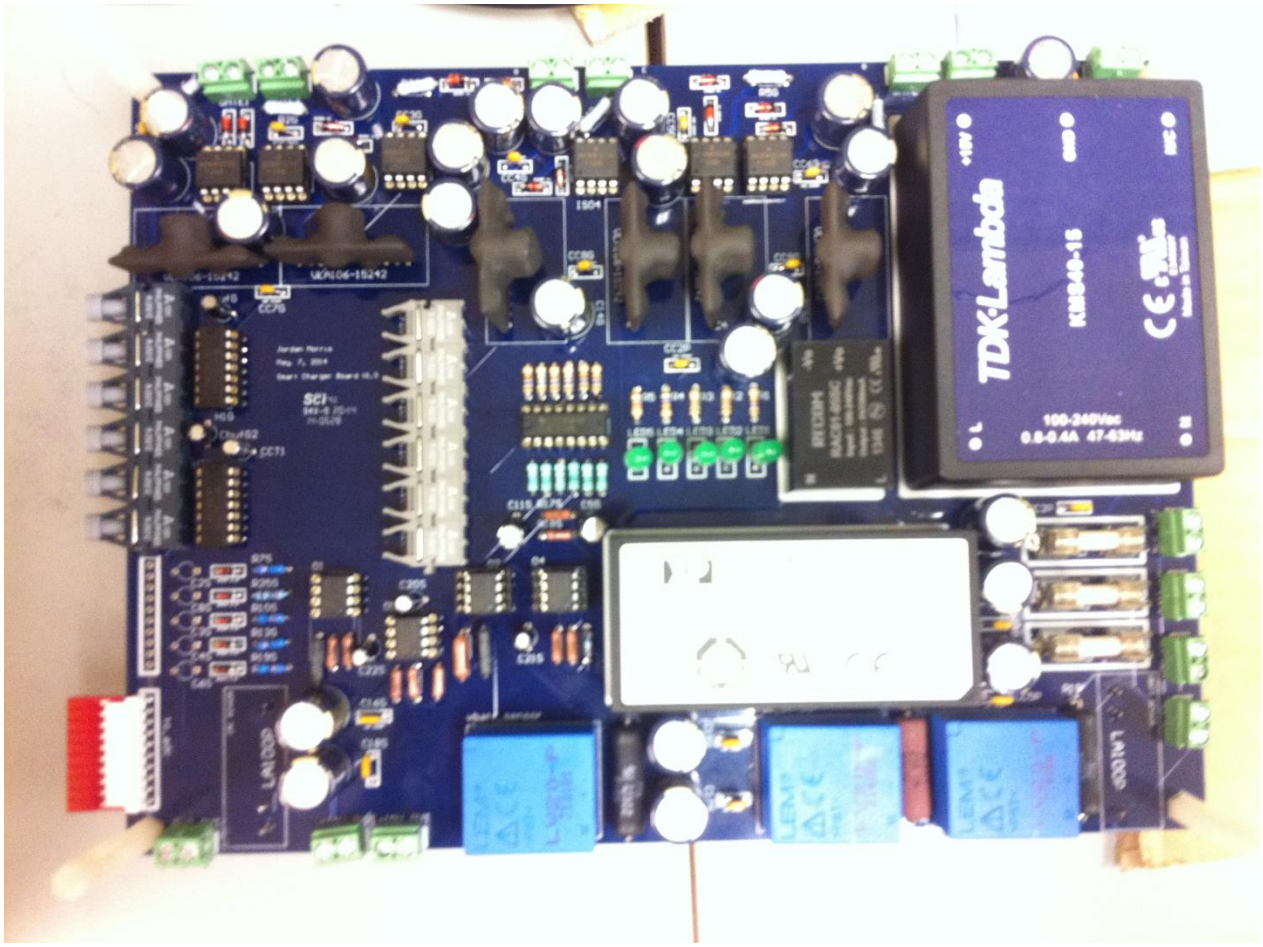

Figure A-6. Smart Charger Board, populated.

Appendix B Smart Charger Communication Controller Interface

The communication controller serves as a link between the end-user and Smart Charger. As a proof of concept, the prototype Smart Charger broadcasts its own Wi-Fi network, which any Wi-Fi enabled device may connect to. The user simply connects like they would to any other wireless network as shown in Figure B-1. The network has been named “jfmorris_smart_charger41850”.

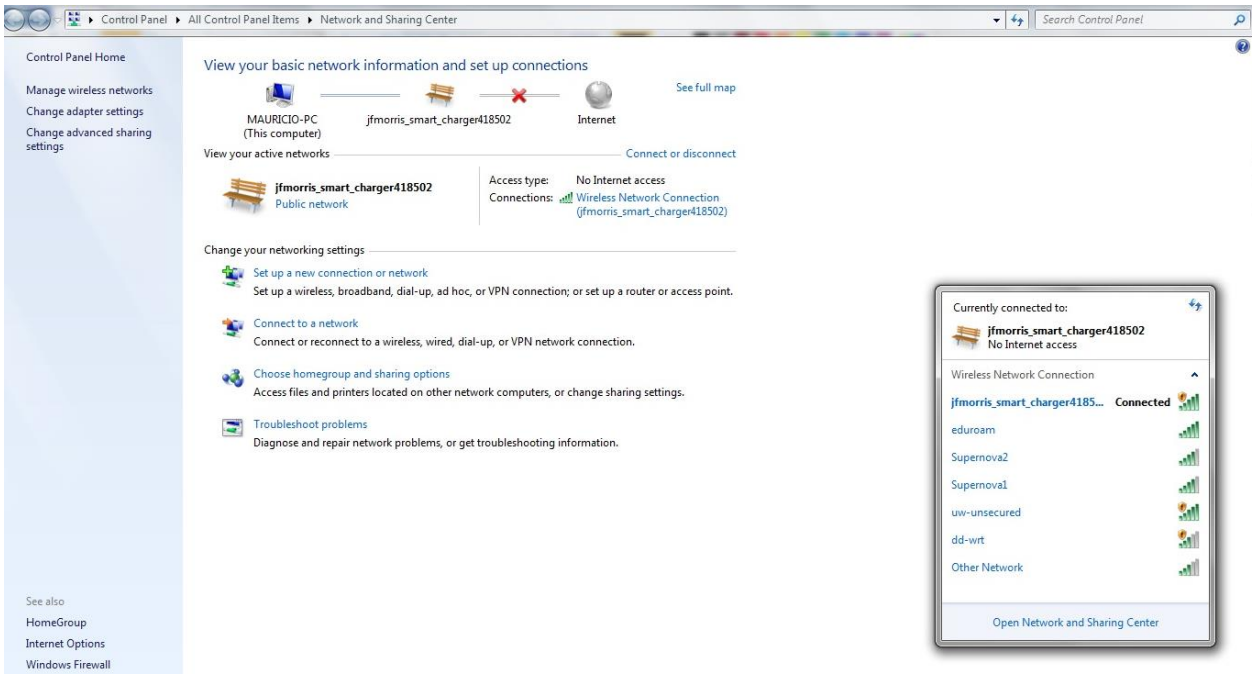

Figure B-1. Smart charger broadcast network.

Once connected to the network the user will need to go to “controls.com” to access the Smart Charger control interface. As shown in Figure B-2 there are various tools available to the user to control the Smart Charger. At the top of the page the current status of the Smart Charger is displayed, letting the user know the current SOC, if user’s device is still connected to the Smart Charger and the chargers power rating. The next three checkboxes are used to: turn the charger on, turn the DC/DC on and enable smart charging. For example, if the first and last boxes are checked then only reactive power control is available since the DC/DC has not been enabled. If the first two boxes are checked, then the charger will behave as a standard charger and if all three are checked then smart charging is available with access to the battery pack. The next part of the interface allows users to input P-Q requests.

The measurements portion of interface, shown in Figure B-3, allows the user to specify the frequency at which they would like to log data. Ten signals are available for logging; active power, reactive power, battery current, battery voltage, DC link voltage, efficiency, battery SOC, Vd, Id and Iq. At the end, once the user is finished, they can export the data to a csv file.

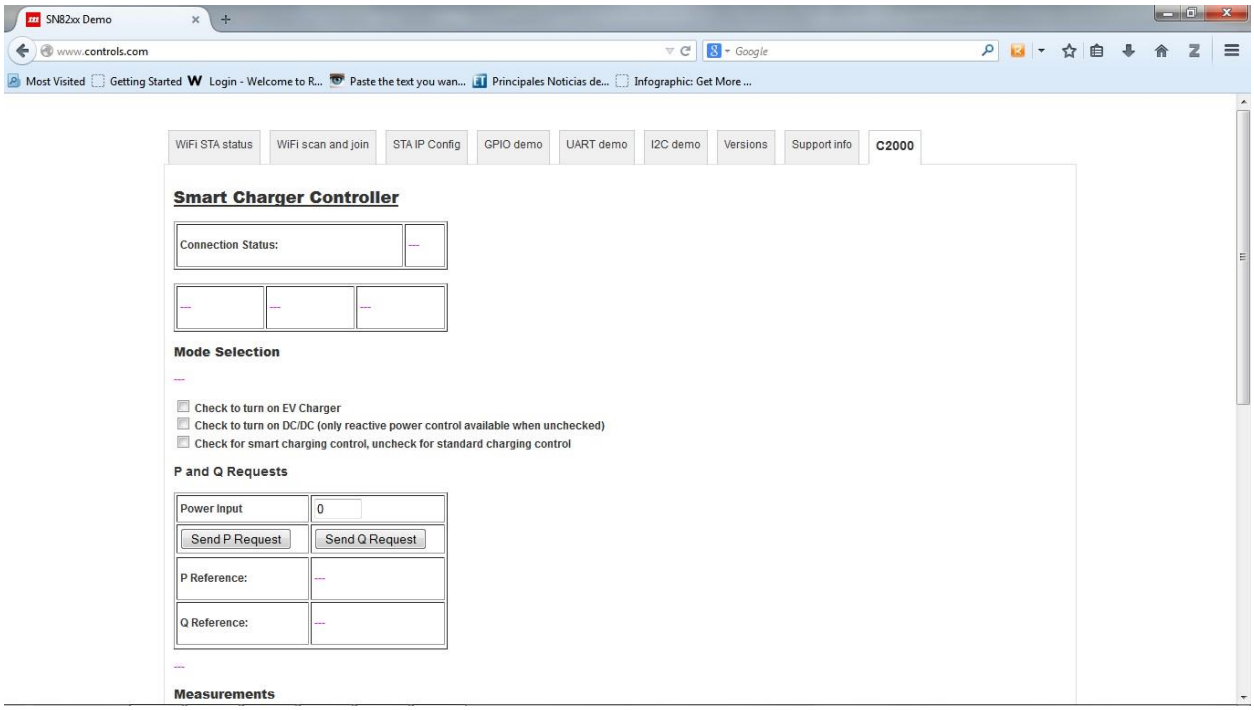

Figure B-2. Smart Charger controller, main page, 1.

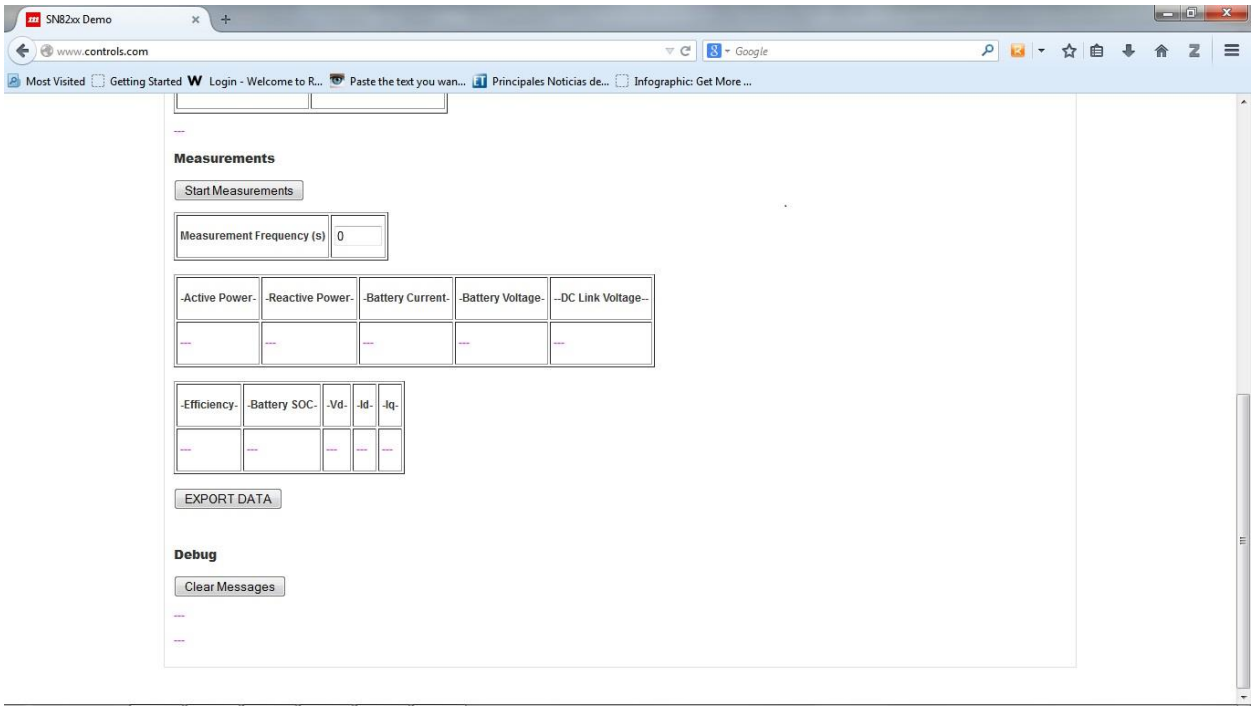

Figure B-3. Smart Charger controller, main page 2.

References

[1] "CO2 Emissions From Fuel Combustion Highlights," International Energy Agency, 2012.

[2] S. G. Wirasingha and A. Emadi, "Pihef: Plug-In Hybrid Electric Factor," *IEEE Trans. Veh. Technol.*, vol. 60, no. 3, pp. 1279–1284, Mar. 2011.

[3] J. Williams, "History and Analysis -Crude Oil Prices." [Online]. Available: http://www.wtrg.com/prices.htm. [Accessed: 09-Aug-2014].

[4] M. Duvall and E. Knipping, "Environmental Assessment of Plug-in Hybrid Electric Vehicles. Volume 1: Nationwide Greenhouse Gas Emissions," EPRI/NRDC, Palo Alto ,CA, 2007.

[5] "Model S Specs | Tesla Motors." [Online]. Available: http://www.teslamotors.com/models/specs. [Accessed: 10-Aug-2014].

[6] SAE International, "SAE J1772 Electric Vehicle and Plug in Hybrid Electric Vehicle Conductive Charge Coupler," 2010.

[7] L. Gan, U. Topcu, and S. H. Low, "Optimal decentralized protocol for electric vehicle charging," *IEEE Trans. Power Syst.*, vol. 28, no. 2, pp. 940–951, May 2013.

[8] E. Sortomme, M. M. Hindi, S. D. J. MacPherson, and S. S. Venkata, "Coordinated Charging of Plug-In Hybrid Electric Vehicles to Minimize Distribution System Losses," *IEEE Trans. Smart Grid*, vol. 2, no. 1, pp. 198–205, Mar. 2011.

[9] O. Sundstrom and C. Binding, "Flexible Charging Optimization for Electric Vehicles Considering Distribution Grid Constraints," *IEEE Trans. Smart Grid*, vol. 3, no. 1, pp. 26–37, Mar. 2012.

[10] C. Zhou, K. Qian, M. Allan, and W. Zhou, "Modeling of the Cost of EV Battery Wear Due to V2G Application in Power Systems," *IEEE Trans. Energy Convers.*, vol. 26, no. 4, pp. 1041–1050, Dec. 2011.

[11] "2015 Volt: Electric Cars - Hybrid Cars | Chevrolet." [Online]. Available: http://www.chevrolet.com/volt-electric-car.html?seo=goo_|_GM+Chevy+Retention_|_1744%7C1751%7CIPUS%7CAU%7CG%7CS%7CB%7CA%7CE%7CGG-RTN-Chevy-Volt-BP-SN-Exact_|_Chevy+Volt_|_chevy%20volt. [Accessed: 03-Aug-2014].

[12] "Nissan LEAF® Electric Car Battery," *Nissan USA*. [Online]. Available: http://www.nissanusa.com/electric-cars/leaf/charging-range/battery. [Accessed: 17-Jun-2014].

[13] "Toyota Prius Interior, Exterior & Safety Features." [Online]. Available: http://www.toyota.com/prius/features.html?srchid=sem|google|Prius|Model_Prius|Prius_Specs_E|Existing|Prius_Features_Mechanical#!/mechanical_performance/1223/1225/1227/1229. [Accessed: 10-Aug-2014].

[14] W. Kempton and J. Tomić, "Vehicle-to-grid power fundamentals: Calculating capacity and net revenue," *J. Power Sources*, vol. 144, no. 1, pp. 268–279, Jun. 2005.

[15] N. Wong and M. Kazerani, "A review of bidirectional on-board charger topologies for plugin vehicles," in *2012 25th IEEE Canadian Conference on Electrical Computer Engineering (CCECE)*, 2012, pp. 1–6.

[16] X. Zhou, S. Lukic, S. Bhattacharya, and A. Huang, "Design and control of grid-connected converter in bi-directional battery charger for Plug-in hybrid electric vehicle application," in *IEEE Vehicle Power and Propulsion Conference, 2009. VPPC '09*, 2009, pp. 1716–1721.

[17] A. K. Verma, B. Singh, and D. T. Shahani, "Grid to vehicle and vehicle to grid energy transfer using single-phase bidirectional AC-DC converter and bidirectional DC-DC converter," in *2011 International Conference on Energy, Automation, and Signal (ICEAS)*, 2011, pp. 1–5.

[18] B. Bilgin, E. Dal Santo, and M. Krishnamurthy, "Universal input battery charger circuit for PHEV applications with simplified controller," in *2011 Twenty-Sixth Annual IEEE Applied Power Electronics Conference and Exposition (APEC)*, 2011, pp. 815–820.

[19] B.-R. Lin, D.-J. Chen, and H.-R. Tsay, "Bi-directional AC/DC converter based on neutral point clamped," in *IEEE International Symposium on Industrial Electronics, 2001. Proceedings. ISIE 2001*, 2001, vol. 1, pp. 619–624 vol.1.

[20] B.-R. Lin, T.-L. Hung, and C.-H. Huang, "Bi-directional single-phase half-bridge rectifier for power quality compensation," *Electr. Power Appl. IEE Proc. -*, vol. 150, no. 4, pp. 397–406, Jul. 2003.

[21] X. Zhou, G. Wang, S. Lukic, S. Bhattacharya, and A. Huang, "Multi-function bi-directional battery charger for plug-in hybrid electric vehicle application," in *IEEE Energy Conversion Congress and Exposition, 2009. ECCE 2009*, 2009, pp. 3930–3936.

[22] M. C. Kisacikoglu, B. Ozpineci, and L. M. Tolbert, "EV/PHEV Bidirectional Charger Assessment for V2G Reactive Power Operation," *IEEE Trans. Power Electron.*, vol. 28, no. 12, pp. 5717–5727, 2013.

[23] M. C. Kisacikoglu, "Vehicle-to-Grid (V2G) Reactive Power Operation Analysis of the EV/PHEV Bidirectional Battery Charger," PhD Dissertation, University of Tennessee, Knoxville, 2013.

[24] W. Luan, D. Sharp, and S. Lancashire, "Smart grid communication network capacity planning for power utilities," in *Transmission and Distribution Conference and Exposition, 2010 IEEE PES*, 2010, pp. 1–4.

[25] S. M. Amin and B. F. WollenBerg, "Toward a Smart Grid," *IEEE Power Energy Mag*, vol. 3, no. 5, pp. 34–41, Oct. 2005.

[26] V. C. Gungor, D. Sahin, T. Kocak, S. Ergut, C. Buccella, C. Cecati, and G. P. Hancke, "Smart Grid Technologies: Communication Technologies and Standards," *IEEE Trans. Ind. Inform.*, vol. 7, no. 4, pp. 529–539, Nov. 2011.

[27] R. P. Lewis, P. Igic, and Z. Zhou, "Assessment of communication methods for smart electricity metering in the U.K.," in *2009 IEEE PES/IAS Conference on Sustainable Alternative Energy (SAE)*, 2009, pp. 1–4.

[28] V. Paruchuri, A. Durresi, and M. Ramesh, "Securing powerline communications," in *IEEE International Symposium on Power Line Communications and Its Applications, 2008. ISPLC 2008*, 2008, pp. 64–69.

[29] VC Gungor, D. Sahin, T. Kocak, and S. Ergut, *Smart Grid Communications and Networking*. Turk Telekom, Tech, 2011.

[30] "The Next Generation of DSL Can Pump 1Gbps Through Copper Phone Lines," *Gizmodo*. [Online]. Available: http://gizmodo.com/the-next-generation-of-dsl-can-pump-1gbps-through-coppe-1484256467. [Accessed: 06-Jul-2014].

[31] D. M. Laverty, D. J. Morrow, R. Best, and P. A. Crossley, "Telecommunications for Smart Grid: Backhaul solutions for the distribution network," in *2010 IEEE Power and Energy Society General Meeting*, 2010, pp. 1–6.

[32] P. Yi, A. Iwayemi, and C. Zhou, "Developing ZigBee Deployment Guideline Under WiFi Interference for Smart Grid Applications," *IEEE Trans. Smart Grid*, vol. 2, no. 1, pp. 110–120, Mar. 2011.

[33] P. Kulshrestha, K. Swaminathan, M.-Y. Chow, and S. Lukic, "Evaluation of ZigBee communication platform for controlling the charging of PHEVs at a municipal parking deck," in *IEEE Vehicle Power and Propulsion Conference, 2009. VPPC '09*, 2009, pp. 1211–1214.

[34] W. Su, W. Zeng, and M.-Y. Chow, "A digital testbed for a PHEV/PEV enabled parking lot in a Smart Grid environment," in *Innovative Smart Grid Technologies (ISGT), 2012 IEEE PES*, 2012, pp. 1–7.

[35] W. Su, H. Eichi, W. Zeng, and M.-Y. Chow, "A Survey on the Electrification of Transportation in a Smart Grid Environment," *IEEE Trans. Ind. Inform.*, vol. 8, no. 1, pp. 1–10, Feb. 2012.

[36] "Chevy Volt Specs," *GM-VOLT : Chevy Volt Electric Car Site*. [Online]. Available: http://gm-volt.com/full-specifications/. [Accessed: 15-Jun-2014].

[37] "GM Voltec™." [Online]. Available: http://www.pluginnow.com/content/gm-voltec%E2%84%A2. [Accessed: 15-Jun-2014].

[38] "Supercharger | Tesla Motors." [Online]. Available: http://www.teslamotors.com/supercharger. [Accessed: 15-Jun-2014].

[39] "IEEE Standard for Interconnecting Distributed Resources with Electric Power Systems," *IEEE Std 1547-2003*, pp. 1–28, Jul. 2003.

[40] "US Nissan LEAF Sales Increase 118%, LEAF Holds #1 Spot In US Electric Car Sales −." .

[41] "Model S Features | Tesla Motors," 04-Oct-2010. [Online]. Available: http://www.teslamotors.com/en_CA/models/features#/performance. [Accessed: 17-Jun-2014].

[42] F. V. Conte, "Battery and battery management for hybrid electric vehicles: a review," *E Elektrotechnik Informationstechnik*, vol. 123, no. 10, pp. 424–431, Oct. 2006.

[43] "What Goes Into A Tesla Model S Battery--And What It May Cost." [Online]. Available: http://www.greencarreports.com/news/1084682_what-goes-into-a-tesla-model-s-battery--and-what-it-may-cost. [Accessed: 17-Jun-2014].

[44] N. N.-Y. Wong, "Design of a Two-Stage Level-Two Bidirectional On-Board Battery Charger for Plugin Vehicles," Jan. 2013.

[45] D. N. Rakhmatov and S. B. K. Vrudhula, "An analytical high-level battery model for use in energy management of portable electronic systems," in *IEEE/ACM International Conference on Computer Aided Design, 2001. ICCAD 2001*, 2001, pp. 488–493.

[46] J. Zhang, S. Ci, H. Sharif, and M. Alahmad, "An enhanced circuit-based model for single-cell battery," in *2010 Twenty-Fifth Annual IEEE Applied Power Electronics Conference and Exposition (APEC)*, 2010, pp. 672–675.

[47] M. Chen and G. A. Rincon-Mora, "Accurate electrical battery model capable of predicting runtime and I-V performance," *IEEE Trans. Energy Convers.*, vol. 21, no. 2, pp. 504–511, Jun. 2006.

[48] "Elite Power Solutions BMS Overview." [Online]. Available: http://elitepowersolutions.com/bms-overview.html. [Accessed: 16-Jun-2014].

[49] T. T. Vo, W. Shen, and A. Kapoor, "Experimental comparison of charging algorithms for a lithium-ion battery," in *IPEC, 2012 Conference on Power Energy*, 2012, pp. 207–212.

[50] B. T. Kuhn, G. E. Pitel, and P. T. Krein, "Electrical properties and equalization of lithium-ion cells in automotive applications," in *Vehicle Power and Propulsion, 2005 IEEE Conference*, 2005, p. 5 pp.–.

[51] B. P. Divakar, K. W. E. Cheng, H. J. Wu, J. Xu, H. B. Ma, W. Ting, K. Ding, W. F. Choi, B. F. Huang, and C. H. Leung, "Battery management system and control strategy for hybrid and electric vehicle," in *3rd International Conference on Power Electronics Systems and Applications, 2009. PESA 2009*, 2009, pp. 1–6.

[52] M. P. Kazmierkowski and L. Malesani, "Current control techniques for three-phase voltage-source PWM converters: a survey," *IEEE Trans. Ind. Electron.*, vol. 45, no. 5, pp. 691–703, Oct. 1998.

[53] N. Wong, K. Zhuge, and M. Kazerani, "A comparative evaluation of control techniques for grid-side AC-DC converter in a two-stage level-two bidirectional battery charger," in *2013 IEEE Transportation Electrification Conference and Expo (ITEC)*, 2013, pp. 1–5.

[54] O. Hegazy, J. Van Mierlo, R. Barrero, P. Lataire, N. Omar, and T. Coosemans, “A comparative study of different control strategies of On-Board Battery Chargers for Battery Electric Vehicles,” in *2013 8th International Conference and Exhibition on Ecological Vehicles and Renewable Energies (EVER)*, 2013, pp. 1–6.

[55] M. C. Kisacikoglu, B. Ozpineci, and L. M. Tolbert, “Examination of a PHEV bidirectional charger system for V2G reactive power compensation,” in *2010 Twenty-Fifth Annual IEEE Applied Power Electronics Conference and Exposition (APEC)*, 2010, pp. 458–465.

[56] B. Bahrani, A. Rufer, S. Kenzelmann, and L. A. C. Lopes, “Vector Control of Single-Phase Voltage-Source Converters Based on Fictive-Axis Emulation,” *IEEE Trans. Ind. Appl.*, vol. 47, no. 2, pp. 831–840, Mar. 2011.

[57] D. N. Zmood and D. G. Holmes, “Stationary frame current regulation of PWM inverters with zero steady-state error,” *IEEE Trans. Power Electron.*, vol. 18, no. 3, pp. 814–822, 2003.

[58] R. Teodorescu, F. Blaabjerg, M. Liserre, and P. C. Loh, “Proportional-resonant controllers and filters for grid-connected voltage-source converters,” *Electr. Power Appl. IEE Proc.*, vol. 153, no. 5, pp. 750–762, Sep. 2006.

[59] U. A. Miranda, L. G. B. Rolim, and M. Aredes, “A DQ Synchronous Reference Frame Current Control for Single-Phase Converters,” in *Power Electronics Specialists Conference, 2005. PESC ’05. IEEE 36th*, 2005, pp. 1377–1381.

[60] M. Yilmaz and P. T. Krein, “Review of Battery Charger Topologies, Charging Power Levels, and Infrastructure for Plug-In Electric and Hybrid Vehicles,” *IEEE Trans. Power Electron.*, vol. 28, no. 5, pp. 2151–2169, May 2013.

[61] L. Shi, A. Meintz, and M. Ferdowsi, “Single-phase bidirectional AC-DC converters for plug-in hybrid electric vehicle applications,” in *IEEE Vehicle Power and Propulsion Conference, 2008. VPPC ’08*, 2008, pp. 1–5.

[62] Muratta, “wifi_sn8200_evkplus_brief.” [Online]. Available: http://www.murata-ws.com/devkit/wifi_sn8200_evkplus_brief.pdf. [Accessed: 02-Aug-2014].

[63] “Elite Power Solutions.” [Online]. Available: http://elitepowersolutions.com/products/product_info.php?cPath=27_38&products_id=186. [Accessed: 03-Aug-2014].

[64] Texas Instruments, “TMS320F2808 Digital Signal Processors Data Manual,” 02-Aug-2014. [Online]. Available: http://www.ti.com/lit/ds/symlink/tms320f2802.pdf.